

6. SITE 1210¹

Shipboard Scientific Party²

PRINCIPAL RESULTS

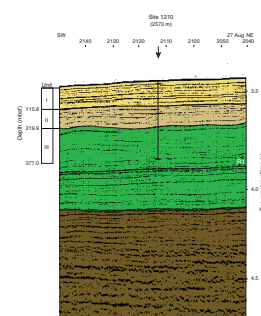
Background

Site 1210 is located on the southern flank of the Southern High of Shatsky Rise on seismic line TN037-17A. Because of the proximity of this site to the seismic lines that are calibrated with drill holes and characteristic sets of reflectors on these profiles, the seismic units of Sliter and Brown (1993) can be identified with confidence. Seismic Unit 1 (Neogene) is relatively condensed, and Units 2 (Paleogene) and 3 (Upper Cretaceous) are moderately expanded (Fig. F1). Although the site was selected at a location where the sedimentary section looks relatively expanded, the section was expected to contain a number of minor disconformities as indicated by prominent horizontal reflectors.

At 2574 m, Site 1210 is the second shallowest site in the Shatsky Rise Paleogene–Late Cretaceous depth transect that ranges from 2387 to 3346 m. As part of this depth transect, cores from Site 1210 will be used to address a number of leg-related objectives focused on abrupt and long-term climate change during the Cretaceous and Paleogene.

Holes 1210A and 1210B were cored largely with the advanced piston corer (APC). Extended core barrel (XCB) center bit drilling was used to punch through chert layers in the Upper Cretaceous section. Hole 1210A terminated at 249.3 meters below seafloor (mbsf) in the core below a major chert horizon in the upper Maastrichtian. In Hole 1210B, a greater effort was made to penetrate the chert layers and to core the surprisingly soft sediment in between them with the APC. In this hole, 11 chert layers were penetrated with XCB center bit drilling, and a total depth of 376.5 mbsf was achieved.

F1. Interpretation of seismic reflection profile, Site 1210, p. 32.



¹Examples of how to reference the whole or part of this volume.

²Shipboard Scientific Party addresses.

Summary of Results

Coring at Site 1210 recovered three lithologic units that have been separated based on composition (Fig. F2). Lithologic Unit I ranges from Holocene to lower Oligocene (0 to ~32 Ma; 0–115.8 mbsf) and consists of clayey nannofossil ooze, nannofossil ooze with clay, and nannofossil ooze. This unit is split into three subunits. Subunit IA (Holocene to upper Miocene; 0 to 5.5 Ma; 0–83.4 mbsf) is olive gray to gray and was deposited at higher rates than Subunit IB (upper Miocene to upper middle Miocene; 5.5 to 11.5 Ma; 83.4–112.0 mbsf), whose color ranges from shades of yellowish brown to pale orange to grayish orange. Subunit IC (upper middle Miocene to lower Oligocene; 11.5 to ~32 Ma; 112.0 to 115.8 mbsf) encompasses several dark yellowish brown clay-rich intervals that represent condensed sections or unconformities, interbedded with pale orange nannofossil ooze. A significant unconformity from lower Miocene to lower Oligocene occurs within this interval (see “**Biostratigraphy**,” p. 56, in “Specialty Syntheses” in the “Leg 198 Summary” chapter). Lithologic Unit II ranges from lower Oligocene to lowermost Paleocene (~32 to 65 Ma; 115.8–219.9 mbsf) and consists of shades of orange and yellowish brown nannofossil ooze, nannofossil ooze with clay, and minor amounts of clay with nannofossil ooze. The unit has a generally higher carbonate content than Unit I. Lithologic Unit III ranges from uppermost Maastrichtian to lower Campanian (65 to ~77 Ma; 219.9–377.0 mbsf) and consists of white nannofossil ooze, nannofossil ooze with foraminifers, and chert. Eleven chert layers were penetrated in lithologic Unit III.

The recovered section at Site 1210 is remarkably similar to that cored at Site 1209 located 29 km to the northeast on the summit of the Southern High. On a large scale, the ages of unconformities at the two sites are similar. On a small scale, critical boundaries—for example, the Paleocene/Eocene and Cretaceous/Tertiary (K/T) boundaries—show a similar, detailed sequence of lithologies. Thus, the two sites have highly comparable sedimentation histories. There are a number of subtle differences between the Site 1209 and 1210 sedimentary sections that yield important interpretations in the depth transect framework of Leg 198. Site 1210 is 200 m deeper than Site 1209. Preliminary biostratigraphy suggests that the middle Miocene to upper Miocene interval at Site 1209 is highly condensed with a number of diastems, whereas the same interval at Site 1210 more likely corresponds to an unconformity (see “**Biostratigraphy**,” p. 13, and “**Sedimentation and Accumulation Rates**,” p. 21). Increased dissolution at Site 1210 in the middle to late Miocene is the most likely mechanism to explain this difference.

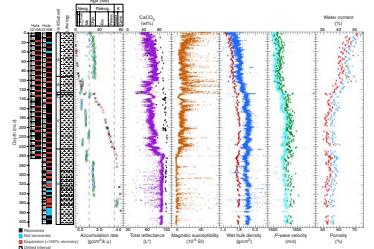
The highlights of coring at Site 1210 are also similar to those at Site 1209, namely the recovery of all of the critical intervals, most in both holes. These include the Eocene/Oligocene boundary, the Paleocene–Eocene Thermal Maximum (PETM), a biological event in the mid Paleocene, the K/T boundary, and the mid-Maastrichtian deepwater event (MME).

Highlights

Recovery of Critical Events

As at Site 1209, a number of critical events have been recovered at Site 1210 in multiple holes. The lithologic record of each of these intervals at Site 1210 appears to be remarkably similar to that at Site 1209.

F2. Coring results, Site 1210, p. 33.



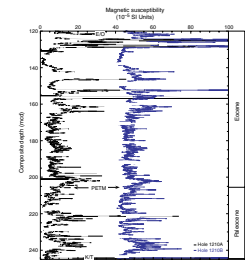
The correlation is especially compelling based on magnetic susceptibility data of the composite section (Fig. F3). These data show similar shaped peaks for the events at the two sites, but perhaps more remarkably, a broadly similar number of peaks in between them. Multisensor track (MST) data will provide precise correlations between the two sites as well as an internal chronology. Site 1210 in general shows a slightly more expanded as well as more complete section in certain intervals. However, in the absence of detailed data and analysis, discussion of the significance of these events would be broadly similar for both Sites 1209 and 1210. More detail on the critical events is presented in “Site 1209,” p. 28, in “Principal Results” in the “Leg 198 Summary” chapter.

The Eocene–Oligocene transition has been recovered in an interval of continuous recovery from Holes 1210A and 1210B. The record for both holes show a gradual increase in carbonate content that is indication for a deepening in the calcite compensation depth (CCD), similar to Site 1209 and sites from the Atlantic and Indian Oceans (e.g., Zachos et al., 1996). The Site 1210 record shows alternating dark and light lithologic cycles throughout this interval that indicate an orbital control on dissolution. In intervals of the uppermost Eocene at Site 1210, planktonic foraminifers are extremely dissolved, suggesting that the site was toward the base of the lysocline. Comparison of carbonate content and microfossil records between the Leg 198 sites will provide important information on changes in the level of the lysocline and CCD through this major cooling event.

The interval recording the PETM was recovered in Holes 1210A and 1210B. The lithologic record of this event is very similar in the two holes; this similarity is borne out by the magnetic susceptibility records (Fig. F3). The sharp base of the event coincides with an abrupt change from a very pale orange nannofossil ooze to a thin (1–2 mm), dark yellowish brown clayey nannofossil ooze. This is overlain by ~18 cm of moderate yellowish brown nannofossil ooze with clay that grades slowly into a pale orange nannofossil ooze. There is a noticeable color change from below the PETM clay-rich horizon to directly above it that persists upsection for at least 10 m. The significance of this color change has not been determined. The clay-rich units show signs of dissolution, although this does not appear to be more pervasive than at Site 1209. Nannofossils appear highly dissolved in the lowest 1 cm of the event, but preservation improves significantly in the middle and upper part of the nannofossil ooze with clay. Blade-shaped, ~10–20 μm calcite grains are observed throughout the clay-rich units. Transient “excursion” planktonic foraminifers that correlate with the interval represented by the negative carbon isotope shift (e.g., Kelly et al., 1996) are observed within and just above the clay-rich units. The lack of significant difference between the PETM records at Sites 1209 and 1210 suggests that these sections were located in a depth range that was relatively insensitive to carbonate solubility changes across the PETM. The Paleocene–Eocene transition at Site 1208, on the other hand, shows a significant amount of dissolution and intervals lacking carbonate, suggesting that it was at a depth (~800 m deeper than Site 1210) far more sensitive to solubility changes.

The record of the K/T boundary at Site 1210 is similar to that at Site 1209. The boundary succession includes uppermost Maastrichtian (nannofossil Zone CC26) pale orange nannofossil ooze overlain by lowermost Paleocene (planktonic foraminiferal Zone P α) grayish orange foraminiferal ooze that grades into a white foraminiferal nannofossil chalk then back into a grayish orange nannofossil ooze. The boundary

F3. Comparison of magnetic susceptibility records, Holes 1210A and 1210B, p. 35.



between the uppermost Maastrichtian and the lowermost Paleocene is clearly bioturbated, and careful sampling of burrows yields planktonic foraminifers dominated by *Guembelitra* with rare *Hedbergella holmdelenensis* that suggest a possible Zone P0 age. Light brown to amber, spherical particles ~50 μm in diameter found in a sample from these burrows may be altered tektites. As at Site 1209, perhaps the most exciting aspect of this boundary succession is the excellently preserved, and apparently expanded, Danian section that will allow us to investigate the detailed record of the recovery and adaptive radiation of floras and faunas after this major extinction event.

The MME also appears to have been recovered at Site 1210. Large *Inoceramus* prisms can be seen over a 2-m interval of the mid-Maastrichtian in Core 198-1210B-28H but disappear above this level. The first occurrence (FO) of the planktonic foraminifer *Abathomphalus mayaroensis* lies in Section 198-1210B-26H-CC, which is consistent with the age of the event at other sites (i.e., MacLeod and Huber, 1996).

Anomalous Lithification of Shatsky Rise Sediments

One of the most interesting results to emerge from Site 1210 and other Southern Rise sites is that the sediment has undergone little lithification, even at comparable burial depths to sediment at other sites that are indurated. For example, at the base of Hole 1210B at 377 mbsf, the predominant lithology is a nannofossil foraminiferal ooze. This sediment is soft, plastic in behavior, and almost uncemented. Nannofossils and foraminifers at this level have suffered a greater amount of dissolution than overgrowth. Chalk is found at a comparable depth in a typical carbonate sequence on the Ontong Java Plateau; in fact, the chalk/ooze boundary is located between 181 and 339 mbsf (Berger et al., 1991). The soft nature of the upper part of the Shatsky Rise section has been discussed by Matter et al. (1975).

At Site 1210 between 200 and 300 mbsf, there are not the expected changes in physical properties that go hand in hand with compaction (e.g., Schlanger and Douglas, 1974). In this interval, gamma ray attenuation (GRA) density decreases, *P*-wave velocity is constant, and porosity increases (see "**Physical Properties**," p. 26). What are the major anomalies at Shatsky Rise that might be responsible for the relative lack of induration of the Cretaceous and Paleogene section? One possible factor that may have played a role in keeping the sediment soft is that sedimentation rates for most of the burial history of the deep section have been relatively slow, except for the last 5 m.y. (see "**Sedimentation and Accumulation Rates**," p. 21). Thus, the time integrated overburden for the deep section has been far less than for most comparable sections.

A second factor is sediment composition. Cretaceous and Paleocene sediments at Site 1210 and other Leg 198 sites on the Southern High of Shatsky Rise are unusually enriched in foraminifers. Qualitative estimates of the foraminiferal abundance range up to 30% by volume, whereas typical deep-sea sediments never exceed 15%–20% foraminifers. The bulk of the remaining volume is composed of nannofossils. The Site 1210 foraminiferal nannofossil oozes do not have anomalous porosities, densities, or *P*-wave velocities. However, the predominantly subspherical shape of foraminifers (vs. the predominantly flat shape of nannofossils) provides a smaller surface of exposed carbonate grains and a lower amount of grain-to-grain contact than in typical nannofossil ooze. Thus, typical nannofossil ooze will experience more pressure solution, and this will lead to a greater amount of available carbonate

for overgrowth on particles and for cement. This general relationship is borne out by results from the Ontong Java Plateau. Shipboard microfossil abundance estimates show a substantial difference in the relative abundance of nannofossils and planktonic foraminifers, especially around the ooze–chalk transition. Although these data are semiquantitative, an apparent relationship exists between the depth of the transition and the relative abundance of foraminifers. Sections with generally higher abundances of foraminifers (Sites 805, 806, and 807) have deeper ooze–chalk transitions, between 264 and 339 mbsf, than those with lower percentages of foraminifers (Sites 803 and 804) where this transition is at 217 and 181 mbsf, respectively.

BACKGROUND AND OBJECTIVES

Site 1210 is located in middle bathyal (2573 m) water depth on the southern flank of the Southern High of Shatsky Rise. According to the reconstruction of Nakanishi et al. (1989), basement underlying the site was formed in the latest Jurassic within Magnetochron M20 (~145 Ma). The site is located on seismic line TN037-17A. Because of the proximity of this site to the seismic lines that are calibrated with drill holes, the seismic units of Sliter and Brown (1993) can be identified with a fair amount of certainty. Seismic Unit 1 (Neogene) is relatively condensed, and Units 2 (Paleogene) and 3 (Upper Cretaceous) are moderately expanded. The paleodepth of this site is ~750 m in the early Maastrichtian based on the estimate of Barrera et al. (1997) for Site 305; however, this estimate is based on the assumption of subsidence rates for normal crust. In actuality, the subsidence history of Shatsky Rise may have been very different than that of normal crust, with much of the subsidence taking place in the first few tens of millions of years (e.g., McNutt et al., 1990).

Site 1210 is the second shallowest site in the Shatsky Rise depth transect. Site 1209 is at 2387 m, ~200 m shallower than Site 1210; the deepest site, Site 1208 at 3346 m, is some 770 m deeper than Site 1210. As part of this depth transect, drilling at Site 1210 addresses a number of leg-related objectives. The sediments recovered at this site will be used to

1. Constrain the character and stability of intermediate- and deep-water circulation and vertical thermal gradients through the Late Cretaceous and Paleogene.
2. Determine long-term climate changes in the Late Cretaceous and Paleogene, in particular, in the onset and demise of the Cretaceous “greenhouse” climates and the onset of Antarctic glaciation in the Eocene.
3. Determine the changes in surface and deepwater biotas over long and short timescales during the Cretaceous and Paleogene and relating them to oceanographic changes.
4. Elucidate the origin of transient climatic events such as the Eocene/Oligocene boundary, the PETM, late Paleocene and early Eocene hyperthermals, and the MME. The depth transect will also constrain changes in temperature, CCD, nutrients, and oxygenation during these events.
5. Determine fluctuations in the CCD through time, compare them to other records from the North Pacific as well as from other

ocean basins, and interpret them in a paleoceanographic framework.

6. Improve understanding of the origin of orbital cycles in the sedimentary record.
7. Continue to refine Cretaceous and Paleogene timescales. We expect to derive a reliable magnetostratigraphy. This will allow us to refine correlations between the geomagnetic polarity timescale and low-latitude biostratigraphies. In intervals with prominent cycles, we will be able to derive high-resolution orbital stratigraphies.

OPERATIONS

Transit from Site 1209 to Site 1210

The 29-nmi transit to Site 1210 required just 3.25 hr, at an average speed of 8.9 kt. At 0750 hr on 23 September, the ship was switched over to dynamic positioning mode, initiating operations at Site 1210.

Hole 1210A

An APC/XCB bottom-hole assembly was assembled and run to near the seafloor. At 1358 hr on 23 September, the bit was positioned at 2581.0 meters below rig floor (mbrf), and a mudline core recovered 5.90 m of sediment, indicating a seafloor depth of 2584.6 mbrf, or 2573.5 meters below sea level (mbsl) (Table T1). APC coring continued to a depth of 233.9 mbsf without incident. Cores 4H through 26H were oriented. An incomplete stroke on Core 26H required deploying a center bit to drill through a ~1-m chert layer. APC Core 27H was deployed, but was also an incomplete stroke, resulting in a decision to terminate the hole at a depth of 242.4 mbsf. Recovery for APC coring in Hole 1210A averaged 103.3%. The drill string was tripped up to the seafloor with the bit clearing the seafloor at 1415 hr on 24 September, ending drilling at Hole 1210A.

T1. Coring summary, p. 69.

Hole 1210B

The ship was offset 15 m to the north, and the bit was positioned 3 m deeper to provide stratigraphic overlap with Hole 1210A. Hole 1210B was spudded at 1645 hr on 24 September, recovering a 9.2-m APC core, which indicated a seafloor depth of 2584.3 mbrf, or 2573.2 mbsl. APC coring advanced the hole to 267.9 mbsf. Cores 4H through 27H were oriented. An incomplete stroke on Core 29H resulted in deployment of the XCB center bit to drill through a chert layer, followed by recovery of another piston core. This technique of drilling through chert layers when encountered (a total of 11.5 m was drilled) and then redeploying the APC to core between layers continued for 13 cores to a depth of 377.0 mbsf. Because of the diminishing core quality of a few of the last cores and the time being expended to drill through the chert layers, we terminated coring after Core 42H. APC coring recovery averaged 103.0% in Hole 1210B. The drill string was retrieved and the ship secured for transit to Site 1211 by 0000 hr on 27 September.

LITHOSTRATIGRAPHY

Description of Lithologic Units

A total of 377.0 m of sediment was cored at Site 1210, representing a time span from the Holocene to the Campanian (Fig. F4). The sediment recovered consists largely of nannofossil ooze with variable amounts of clay and chert. Rare occurrences of clay-rich intervals represent condensed intervals. In general, carbonate content and bulk density increase downcore, yet no transition to chalk was observed (Fig. F4). The intercalation of several layers of chert with soft nannofossil ooze in the Cretaceous sediments led to lower recovery in this portion of the sequence. Minor and trace components observed in the nannofossil oozes include foraminifers, diatoms, radiolarians, silicoflagellates, sponge spicules, inorganic calcite, Fe oxides, opaque minerals, pyrite, quartz, volcanic glass, feldspar, and mica (see “Site 1210 Smear Slides,” p. 70, and “Site 1210 Thin Sections,” p. 72). Other minor lithologies encountered include two discrete volcanic ash layers in the Neogene and ~0.5 m of chalk just above the K/T boundary.

Three lithologic units have been defined for the composite section of Holes 1210A and 1210B. Unit I (0–115.8 mbsf in Hole 1210A) contains clayey nannofossil ooze, nannofossil ooze with clay, and lesser amounts of nannofossil ooze. A color transition from gray and olive gray to orangish and yellowish brown marks the division between Subunits IA and IB. Subunit IC encompasses several clay-rich intervals that likely represent condensed sections. The boundary between Units I and II is defined at the base of a condensed interval of early Oligocene–middle Miocene age. Unit II (115.8–219.9 mbsf in Hole 1210A) consists primarily of very pale orange (10YR 8/2) to moderate yellowish brown (10YR 5/4) nannofossil ooze and nannofossil ooze with clay. This unit is characterized by higher carbonate content and softer consistency than Unit I. The base of Unit II is placed at the K/T boundary. Unit III (219.9–377.0 mbsf in Hole 1210B) extends from the K/T boundary to the bottom of Hole 1210B and contains interbedded white (N9) nannofossil ooze (~96–100 wt% CaCO₃) and chert.

Lithologic Unit I

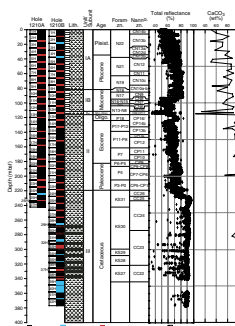
Intervals: 198-1210A-1H-1, 0 cm, through 13H-4, 90 cm, and 198-1210B-1H-1, 0 cm, through 13H-1, 104 cm

Depths: 0 to 115.8 mbsf in Hole 1210A and 0 to 114.74 mbsf in Hole 1210B

Age: Holocene to early Oligocene

Unit I extends from the core top to the base of a clay-rich condensed interval that may represent an unconformity separating the middle Miocene and lower Oligocene. Clayey nannofossil ooze, nannofossil ooze with clay, and lesser amounts of nannofossil ooze compose the dominant lithologies present in this unit. Darker and lighter intervals in Unit I are generally defined by variable proportions of clay and biogenic carbonate. Unit I is subdivided into three lithologic subunits. The division between Subunit IA (0–83.4 mbsf in Hole 1210A) and Subunit IB (83.4–112.0 mbsf in Hole 1210A) is located at a transition from olive gray and gray to orange and yellowish brown hues. Subunit IC (112.0–115.8 mbsf) is distinct from the remainder of Unit I, because it contains several clay-rich condensed intervals.

F4. Core recovery, lithology, lithologic units, age with corresponding biostratigraphic zonation, color reflectance, and percent carbonate, p. 36.



Subunit IA

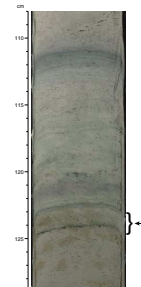
Subunit IA (intervals 198-1210A-1H-1, 0 cm, through 10H-1, 138 cm, and 198-1210B-1H-1, 0 cm, through 9H-6, 0 cm) contains Holocene- to late Miocene-age sediment. Nannofossil ooze in this subunit has a higher clay content, and thus a lower carbonate content, than nannofossil ooze recovered downcore. The lithology predominantly grades from light olive-gray (5Y 8/1) and olive-gray (5Y 6/1) clayey nannofossil ooze to very light gray (N8), light gray (N7), and medium light-gray (N6) nannofossil ooze. These lithologies alternate throughout Subunit IA on a decimeter scale. Color transitions are generally gradational, and bioturbation ranges from rare to moderate. Where color contrasts are greater, mottling from bioturbation is more clearly visible. Rare, centimeter-scale open burrows are usually filled with pyritic nannofossil ooze, with the exception of two open burrows in Cores 198-1210A-2H and 4H that contain pyritic foraminiferal ooze. One discrete volcanic ash layer was observed in this subunit, and several pumice fragments were identified in the upper 30 m.

The upper cores in Holes 1210A and 1210B exhibit sharper contacts between colors and show some evidence of soft-sediment deformation, which may be a syndepositional feature or a product of drilling disturbance. Aside from this observation, no drilling deformation was observed in the remainder of Unit I.

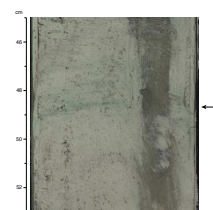
Millimeter-scale pyrite blebs and nodules as well as millimeter- to centimeter-scale clay-rich, pale green laminae are both common features in Subunit IA. These diagenetic laminae sometimes appear as diffuse bands and in some cases are associated with diffuse bands that, in some cases, are purple in color. Some pale green laminae appear to be more fully developed and occur as relatively thick (up to ~1 cm) bands that are more lithified than the surrounding stiff nannofossil ooze. Pale green laminae are generally oriented horizontally but appear to be randomly distributed in space and in relation to the light-dark color cycles of the ooze. These laminae were observed to both crosscut burrows (Fig. F5) and to be crosscut by burrows (Fig. F6), implying that they are a product of early diagenesis. X-ray diffraction (XRD) analyses were performed on calcite-free samples (see “X-Ray Diffraction,” p. 9, in “Lithostratigraphy” in the “Explanatory Notes” chapter) from several pale green laminae, as well as from nannofossil ooze above and below the laminae to assess the clay mineralogy (Fig. F7). Shipboard XRD results indicate that pale green laminae are concentrated layers of saponite (saponite-15A; JCPDS 29-1491), a Mg-Ca-bearing smectite group clay. X-ray diffractograms display a shift to 18.7 Å due to expansion from glycolation and to 10.2 Å upon heating, consistent with the behavior of saponite (Fig. F8). This mineralogy is consistent with XRD results from pale green laminae at Site 1209 (Table T2). The clay of the surrounding ooze contains saponite, illite, and smectite-kaolinite (relative abundances not determined). Some illite also appears to be present in the green laminae; however, we suspect that this may be the result of a contamination of the sample with some of the surrounding sediment.

Thin sections were made of two well-defined green laminae (intervals 198-1210B-6H-7, 56–64 cm, and 6H-3, 57–65 cm). In these thin sections, clay is observed to have precipitated in foraminiferal tests, particularly in the pores (Fig. F41, p. 131, in the “Leg 198 Summary” chapter). Clay also is present in irregular thin seams and wisps and as a product of partial alteration of disseminated shards of volcanic glass. Some burrows are entirely filled with grains of volcanic glass that are only

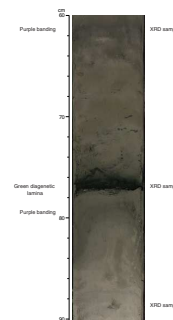
F5. Green lamina crosscutting some burrows, p. 37.



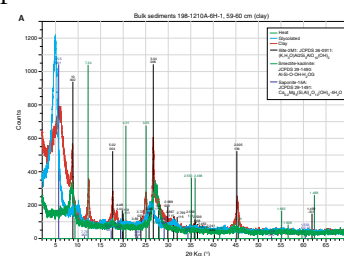
F6. Burrow crosscutting green lamina, p. 38.



F7. Example of well-defined pale green lamina with diffuse purple banding above and below, p. 39.



F8. X-ray diffractograms for bulk sediment and green lamina, p. 40.



T2. Mineralogy of clay fraction, p. 71.

slightly altered around the edges. Authigenic clay is growing in the interstices of these glass grains, and there is much less clay in the center of the burrow.

Subunit IB

Subunit IB (intervals 198-1210A-10H-1, 138 cm, through 13H-1, 112 cm, and 198-1210B-9H-6, 0 cm, through 12H-6, 30 cm) includes sediment of middle to late Miocene age. Subunit IB has the same lithologic composition as Subunit IA but is distinguished by pale yellowish brown (10YR 6/2) to moderate yellowish brown (10YR 5/4) clayey nannofossil ooze and very pale orange (10YR 8/2) to grayish orange (10YR 7/4) nannofossil ooze with clay as opposed to the olive gray and light gray hues characteristic of Subunit IA. Red/blue reflectance ratios are ~1.5 times greater in Subunit IB than in Subunit IA. Color transitions are gradational, and dark and light intervals alternate in decimeter-scale cycles in the upper part of this subunit and increase to meter-scale cycles in the lower portion of the subunit. A notable shift in the reflectance data to lower values occurs within Subunit IB (Fig. F4). Pyrite is a very rare component in Subunit IB, and pale green diagenetic laminae are absent. A pumice fragment and a discrete layer of volcanic ash are both observed in Core 198-1210A-11H. Bioturbation is rare to moderate, as in Subunit IA. *Zoophycos* trace fossils were identified in Core 198-1210A-10H.

Subunit IC

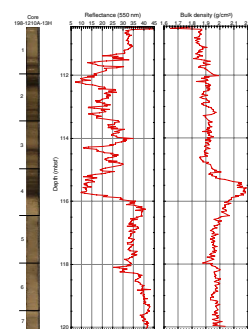
Subunit IC (intervals 198-1210A-13H-1, 112 cm, through 13H-4, 90 cm, and 198-1210B-12H-6, 30 cm, through 13H-1, 104 cm) includes several clay-rich condensed intervals that occur in the middle Miocene, near the base of Unit I (Fig. F9). Intervals of dark yellowish brown (10YR 4/2) clay with nannofossils in Core 198-1210A-13H contain philipsite, barite, and Fe oxides as minor components, as well as trace amounts of quartz, volcanic glass, and opaques. Clay-rich intervals (~24–35 wt% carbonate) in Subunit IC are interbedded with very pale orange (10YR 8/2) nannofossil ooze. The basal clay interval in this subunit contains nannofossils early Oligocene to middle Miocene in age.

Lithologic Unit II

Intervals: 198-1210A-13H-4, 90 cm, through 24H-4, 48 cm, and 198-1210B-13H-1, 104 cm, through 24H-1, 52 cm
 Depths: 115.8 to 219.88 mbsf in Hole 1210A and 114.74 to 218.72 mbsf in Hole 1210B
 Age: early Oligocene to early Paleocene

Unit II extends from the early Oligocene to the K/T boundary and consists predominantly of homogeneous very pale orange (10YR 8/2) to grayish orange (10YR 7/4) nannofossil ooze with lesser amounts of pale yellowish brown (10YR 6/2) to dark yellowish brown (10YR 4/2) nannofossil ooze with clay, clayey nannofossil ooze, and clay with nannofossils. Color gradations are subtle throughout this unit. The ooze in Unit II is much softer than in Unit I, and it was probably made soupier by the drilling and splitting process. Carbonate content of the nannofossil ooze is generally higher in Unit II (~73–100 wt%) than it is in Unit I (~50–91 wt%) (Fig. F4). Bulk density also shifts to higher values in Unit II (Fig. F34). Bioturbation is rare to moderate and is characterized by white (N9) to very pale orange (10YR 8/2) centimeter-scale burrow fills. Some tek-

F9. Composite digital photograph, color reflectance, and bulk density, Core 198-1210A-13H, p. 42.



tites were recovered from a core catcher in Unit II (Section 198-1210A-14H-CC), which is late Eocene in age. A sharp contact between a clay-rich interval overlying a relatively carbonate-rich interval in Sections 198-1210A-20H-6, 52 cm, and 198-1210B-20H-3, 110 cm, has been identified as correlative to the PETM based on shipboard biostratigraphy (Fig. F10). The lowermost Paleocene portion of the section is characterized by lighter colors (very pale orange [10YR 8/2] to white [N9]) and contains pyritized vertical burrows. A more lithified foraminifer-nannofossil chalk directly overlies the K/T boundary. Most of the foraminifers have chambers filled with pyrite.

Lithologic Unit III

Intervals: 198-1210A-24H-4, 48 cm, through 27H-CC and 198-1210B-24H-1, 52 cm, through 42H-CC
Depth: 219.88 to 242.4 mbsf in Hole 1210A and 218.72 to 377.0 mbsf in Hole 1210B
Age: Maastrichtian to Campanian

Unit III consists of interbedded chert and white (N9) nannofossil ooze and nannofossil ooze with foraminifers. Chert layers were drilled with the XCB center bit, and then the APC was used to recover the softer nannofossil ooze interbeds. As a result, the chert was intensely brecciated by the drilling process. This is particularly evident in the top of several cores where the residue from center-bit drilling collected. Carbonate content is ~96–100 wt% in the ooze intervals. Small patches of granular green material consist of foraminifers with green (possibly glauconite?) infill. Rare patches of pyrite blebs were observed, as well as larger (centimeter-scale) green patches of unknown mineralogy. One Maastrichtian-age core (Core 198-1210B-28H) contained shell fragments of *Inoceramus*.

Interpretation

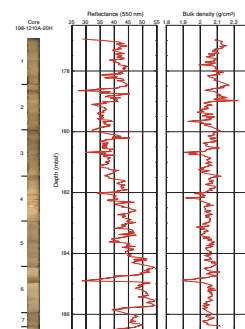
Notable features of the section recovered at Site 1210 include an unconformity between the middle Miocene and lower Oligocene and several boundary sections of particular interest to the shipboard party, including the Eocene/Oligocene, Paleocene/Eocene, and K/T boundaries. Comparison of the sedimentary record through these critical intervals to those recovered at other sites drilled on Leg 198 will allow for interesting comparisons along paleolatitudinal and paleodepth transects.

Sedimentation

Unit I

Sedimentation accumulation rates throughout Unit I average between 14.4 and 16.0 m/m.y. and are similar to those of the time-equivalent section at Site 1209 (Fig. F18). The prevalence of bioturbation in Unit I indicates that sediment at Site 1210 was deposited under sufficiently oxic conditions. Dark-light color cycles that prevail throughout this sequence result from varying proportions of clay and biogenic carbonate content. This pattern is a manifestation of variation in carbonate production and/or dissolution. Modern water depth at Site 1210 is slightly deeper than at Site 1209 (~2.6 vs. ~2.4 km), yet both sit well above the lysocline and the CCD that are regionally located at ~3.5 and 4.1 km, respectively. Because the CCD deepens in the Pacific basin during glacial periods (Farrell and Prell, 1989), it is unlikely that the cyclic

F10. Composite digital photograph, color reflectance, and bulk density, Core 198-1210A-20H, p. 43.



variation in carbonate content observed is produced by shoaling cycles of the lysocline/CCD that occur in concert with glacial–interglacial transitions. In contrast to Sites 1207 and 1208, there is very little biogenic silica at Site 1210; rare occurrences of biogenic silica in smear slide analysis amount to only ~1%–2%. Although Site 1209 is also largely devoid of biogenic silica, there is a peak in biosiliceous deposition (up to 25% in smear slide estimates) in the mid-Pliocene that does not appear at the slightly more southerly Site 1210. This may reflect the effects of dissolution at Site 1210 or greater rates of deposition of biogenic silica at Site 1209 in the Pliocene.

Substantially fewer ash layers are present in the Neogene section at Site 1210 than at previous Leg 198 sites. Regional studies (e.g., Natland, 1993) of ash distribution across Shatsky Rise suggest that beds of ash are wind-borne from volcanic eruptions along the Japan and/or Kurile magmatic arc systems. Differences in the frequency of ash beds between these drilling sites could be linked to distance from the arc system or differences in prevailing wind patterns at these localities. The combination of differences in volcanic ash frequency and in biogenic silica composition suggest the possibility that the prevailing wind and current dynamics at Site 1210 were distinct from the more northerly Sites 1207–1209 on Shatsky Rise.

Below 83.4 mbsf in Subunit IB, the sediment is more oxidized, characterized by shades of pale orange and grayish orange rather than olive gray and gray hues. This color transition is evident in the color reflectance data by an increase in red/blue ratios. Weight percent carbonate increases in Subunit IB, giving rise to higher bulk density (Fig. F4). Subunit IC contains several clay-rich condensed intervals, which possibly are the result of shoaling of the CCD in the early to middle Miocene (Rea et al., 1995). These dark horizons contain approximately a few percent phillipsite, barite, and Fe oxides based on smear slide estimates. It is unclear whether the dark, clay-rich intervals in Subunit IC represent periods of nondeposition, erosion, or relatively continuous but slow sedimentation rates.

Unit II

This unit is composed of sediment that is remarkably homogenous in composition and physical properties such as bulk density and color reflectance (Fig. F4). Sedimentation rates in the Paleogene are much lower than those in Unit I, ranging from ~2.1 to 7.6 m/m.y., most likely a result of lower carbonate production, higher rates of carbonate dissolution, and consequent development of condensed sequences. The homogenous texture of the ooze, disrupted only by rare burrow fills, is evidence that oxic conditions prevailed during sedimentation. High carbonate content throughout Unit II indicates that deposition generally occurred well above the CCD during the Paleogene. Tektites recovered from the upper Eocene in Hole 1210A (Section 198-1210A-14H-CC) are closely correlative with the timing of the Popigan impact in Russia and the Chesapeake Bay bolide.

The PETM interval is hypothesized to represent enhanced carbonate dissolution, triggered by the release of large quantities of methane clathrate (Dickens et al., 1995). This interval is slightly bioturbated at Site 1210 but otherwise fully intact and will provide a valuable resource for shore-based studies comparing the geochemical record preserved on Shatsky Rise during the PETM. Although it appears that the paleodepth of Shatsky Rise at Site 1210 was well above the CCD during much of the Paleogene, the CCD must have shoaled rapidly during the PETM. There

is a clear contrast between the clay-rich layer at the base of the event and the underlying carbonate-rich layer. The clay-rich interval just above this event grades back into more carbonate-rich sediment upsection, likely due to the deepening of the CCD.

Unit III

The nannofossil ooze in Unit III is nearly pure carbonate and remains white in color throughout the Maastrichtian and Campanian section recovered at Site 1210. The ooze alternates with chert, and in two places the chert appears to exist as nodules. Because the drilling process brecciated the chert, it is difficult to interpret whether the chert is primarily nodular or occurs in layers. The presence of chert in Unit III is in sharp contrast to Units I and II, which are almost entirely composed of carbonate and clay.

Inoceramus fragments are locally present in the mid-Maastrichtian (Sections 198-1210B-28H-5 and 28H-6). The occurrence of *Inoceramus* is restricted to sediment of mid-Maastrichtian and older age (MacLeod et al., 1996), but visible shell fragments are restricted to the mid-Maastrichtian on Shatsky Rise at Sites 1210 and 1209.

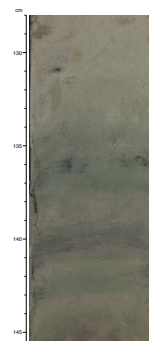
Diagenesis

Unit I

Bulk density increases downcore with carbonate content (Fig. F4), yet carbonate sediment throughout the entire sequence at Site 1210 is unlithified with the exception of a short interval of chalk just above the K/T boundary. Relatively low redox conditions persist through the upper 70 m of sediment, where it is olive gray in color and there are frequent occurrences of pyrite. Decreasing sulfate concentrations in the pore waters through Unit I (see “Inorganic Geochemistry,” p. 23) are consistent with sulfate reduction and, therefore, with pyrite formation. Other interesting diagenetic features that may be associated with reducing pore waters through this section are frequent pale green laminae, which are sometimes associated with diffuse purple banding. Smear slide analyses suggest that the well-developed green laminae are nearly 100% clay. XRD analysis of the clay fraction of the bulk sediment indicates the presence of illite, saponite, and smectite-kaolinite (relative abundances undetermined). However, the mineralogy of the green diagenetic laminae is primarily saponite ($\text{Ca}_{0.2}\text{Mg}_{0.8}(\text{Si},\text{Al})_4\text{O}_{10}(\text{OH})_2$), a clay belonging to the smectite group (Table T2). Similar features have been observed in previous Deep Sea Drilling Project (DSDP) and Ocean Drilling Program (ODP) sediment cores (e.g., Winterer, Riedel, et al., 1971; Kennett, von der Borch, et al., 1986) and have been rationalized as altered volcanic ash (Gardner et al., 1986; Lind et al., 1993). Yet several lines of evidence lead us to suggest that these green laminae are authigenically produced rather than altered volcanic glass grains:

1. Green laminae are not intimately associated with ash layers, and no green color is observed at the edges or within volcanic ash intervals.
2. Green laminae were observed to crosscut burrows and are also crosscut by burrows, indicating that they are an early diagenetic product (Figs. F5, F6).
3. In places, diffuse green laminae were found just above or below diffuse purple color bands, suggestive of a redox front diffusing through the sediment column (Fig. F11).

F11. Diffuse green and purple banding, p. 44.



We note, however, that the temporal distribution of the green diagenetic laminae is similar to that of volcanic ashes at Site 1210 as well as at the previous sites (1207–1209). It is possible that volcanic glass present in the sediment column provides a source of silica and cations for saponite authigenesis. Alternatively, dissolution of biogenic silica could also generate a source of silica. Pore water profiles at Site 1210 demonstrate a depletion of Mg in the upper portion of the section, which is consistent with the formation of saponite through this interval (see [“Inorganic Geochemistry,”](#) p. 23).

Unit II

Laths of inorganic calcite are present as a minor component in some of the smear slides from Unit II. It is probable that these crystals represent incipient cementation of carbonate from the pore waters.

Unit III

Carbonate sediment of Cretaceous age in Unit III is remarkably unlithified, despite ~220 m of sediment overburden. Some of the ooze in this unit is stiff, while other portions are very soft and likely became soupy during drilling and splitting. In places, the ooze seems somewhat more indurated, but this may have occurred as sections were compacted and stretched during drilling.

Although there is no evidence for biosiliceous material in the nannofossil oozes, this component was likely concentrated through diagenetic dissolution and remobilization of the silica, which was eventually converted to chert. We suspect that the chert recovered from this sequence exists primarily as layers, in part due to evidence for layered chert at Site 1207 (see [“Downhole Measurements,”](#) p. 40, in the “Site 1207” chapter). However, in two places where the stratigraphy within the ooze appears to be preserved, chert nodules within the core were observed. Chert recovered from Site 1210 differs from that at Site 1207 in that no porcellanite coatings or inclusions were observed at Site 1210. The chert was also relatively a monochrome medium dark gray (N4) to black (N2) and did not have the variety in color that was observed at Site 1207.

BIOSTRATIGRAPHY

The Neogene section of nannofossil ooze and clay-rich nannofossil ooze in Holes 1210A and 1210B ranges from the Pleistocene to lower Miocene. This interval appears to be complete, at least within the stratigraphic resolution achieved shipboard. Sedimentation rates in the Pleistocene, Pliocene, and upper Miocene are relatively high (Samples 198-1210A-1H-CC through 6H-CC and 198-1210B-1H-CC through 5H-CC) but decrease considerably in older Neogene sediments (Samples 198-1210A-6H-CC through 7H-2, 20 cm) (see [“Sedimentation and Accumulation Rates,”](#) p. 21). Planktonic foraminiferal datums indicate that a significant unconformity exists near the base of the Miocene (Samples 198-1210A-13H-CC and 198-1210B-13H-CC) that extends into the lower Oligocene. However, samples taken at higher resolution for study of calcareous nannofossils reveal the possibility of a condensed section in this interval.

With the exception of the condensed/truncated mid- and upper Oligocene sediments, the Paleogene section from Site 1210 is also relatively complete. High-resolution sampling for both calcareous nanno-

fossil and planktonic foraminiferal biostratigraphy suggests that several key intervals were recovered, including the Eocene/Oligocene boundary, the Paleocene/Eocene boundary transition, PETM, and K/T boundary. A thick and continuous section of nannofossil ooze was also recovered from the Maastrichtian to the lower part of the upper Campanian, which may contain the mid-Maastrichtian event. The main calcareous nannofossil and foraminiferal datums are summarized in Tables T3 and T4.

Calcareous nannofossils are generally abundant and moderately to well preserved in the Cenozoic and Mesozoic sediments of Holes 1210A and 1210B. Planktonic foraminifers exhibit variable preservation and diversity. In particular, preservation is generally poor in samples from the middle to lower Miocene, lower Oligocene, and upper Eocene. This is indicated by the absence of more delicate taxa, higher percentages of dissolution-resistant species, and the prevalence of authigenic minerals. All core catcher samples were examined, and supplementary samples were used to refine datums and the stratigraphy in and around critical intervals.

Studies on benthic foraminifers were conducted on selected core catcher samples from Holes 1210A and 1210B. The >250- μm size fraction was examined in Neogene samples, and the >125- μm size fraction was examined in Paleogene and Cretaceous samples. Pleistocene through Oligocene sediments yield benthic foraminifers that are well preserved and rare to few in abundance. The Eocene through Cretaceous sediments yield moderately preserved benthic foraminifers that are generally rare to few in abundance.

Calcareous Nannofossils

Calcareous nannofossils are generally abundant and moderately to well preserved in Holes 1210A and 1210B. Both the Cenozoic and Mesozoic parts of the succession appear to be stratigraphically complete, at least to within nannofossil biostratigraphic resolution achieved shipboard. However, a number of upper to middle Miocene zones are missing, and because zonal markers are extremely rare or absent, an unconformity may separate the lower or middle Miocene and lower Oligocene.

Neogene

The Neogene section ranges from the upper Pleistocene (Subzone CN14b) to the lower middle Miocene (Zones CN3–CN4). Most of the zones of Okada and Bukry (1980) were recognized. The middle to lower Miocene (Subzone CN5a to Zone CN3) was difficult to subdivide because of the sporadic presence of the nominal taxon *Sphenolithus heteromorphus*, as reported from previous Leg 198 sites. At Site 1210, *S. heteromorphus* was only recorded in Sample 198-1210B-12H-CC.

Paleogene

Between Samples 198-1210A-12H-CC and 13H-CC and 198-1210B-12H-CC and 13H-CC there is a stratigraphic gap of ~13 m.y., comprising Zone CN2 (lower Miocene) to Zone CP18 (lower Oligocene). The underlying Paleogene section appears to be relatively complete. The PETM interval is characterized by the presence of abundant *Discoaster multiradiatus*, the abundance decrease and last occurrence of *Fasciculithus* (in Section 198-1210A-20H-6), and, above, by the first occurrence

T3. Calcareous nannofossil datums, ages, and depths, p. 72.

T4. Planktonic foraminifer datums, ages, and depths, p. 73.

of *Discoaster diastypus* (Sample 198-1210A-20H-3, 100 cm), which marks the base of Zone CP9.

The K/T boundary interval is apparently complete. Sediments containing *Micula prinsii*, the nominal taxon for Zone CC26, are overlain by a white carbonate interval, which yields smear slides dominated by fine micrite, minute foraminifers, and abundant calcispheres, with few reworked Cretaceous nannofossil taxa. These sediments consistently contain survivor taxa (e.g., species of *Cyclagelosphaera* and *Markalius*). The first new Paleocene coccolith genus, *Neobiscutum*, is recorded in Sample 198-1210B-24H-1, 40 cm.

Cretaceous

The apparently continuous section of Maastrichtian to Campanian sediments recovered at Site 1210 yields well-preserved and diverse assemblages of calcareous nannofossils. Zones CC26 to CC21–CC20 were identified, but a number of subzones could not be identified. Certain marker taxa were difficult to identify with certainty because of the presence of transitional morphologies (e.g., *Micula murus* and *Reinhardtites levis*) or were very rare (e.g., *Tranolithus orionatus*). In addition, a number of ranges that are inconsistent with other sections were recorded; *Lithraphidites quadratus* was not found beneath the range of *M. murus*, and *Eiffelithus eximius* did not co-occur with *Uniplanarius trifidum*. The nature of these difficulties will be a focus of postcruise investigations.

Planktonic Foraminifers

Neogene

Planktonic foraminifers are common to abundant, and preservation is moderate to good in the apparently complete upper Pliocene to Pleistocene interval (Zones N21–N22; Sections 198-1210A1H-CC to 6H-CC and 198-1210B-1H-CC to 6H-CC). *Globorotalia inflata* and/or *G. crassaformis* are particularly abundant through this interval.

The upper Miocene–lower Pliocene interval also appears to be complete, although abundance varies from few to common and preservation is poor to moderate. A downhole increase in foraminiferal test fragmentation indicates that dissolution may be partially responsible for the sporadic distribution of biostratigraphically useful taxa through this interval. However, the last occurrences of *Dentoglobigerina altispira*, *Sphaeroidinellopsis seminulina*, *Globorotalia margaritae*, and *Globoturbotalita nepenthes* are valuable orbitally tuned datums that are present in the mid- to lower Pliocene. Likewise, the FO of *Globorotalia tumida* is a reliable datum in the uppermost Miocene (base of Zone N18).

Fragmentation and very low foraminiferal abundances are prevalent through the condensed lower portion of the upper Miocene (Zones N14–N5; Samples 198-1210A-11H-CC and 198-1210B-11H-CC) and also in the middle Miocene (Zone N10; Samples 198-1210A-12H-CC and 198-1210B-12H-CC). This interval is dominated by dissolution-resistant taxa, including *Sphaeroidinellopsis seminulina*, *S. kochii*, *S. disjuncta*, *Globoquadrina dehiscens*, and *G. venezuelana*. Rare age-diagnostic taxa in Zone N14 include *Globoturbotalita nepenthes*, *Paragloborotalia mayeri*, *Globorotalia menardii*, and *G. praemenardii*. Rare age-diagnostic taxa in Zone N10 include *Orbulina universa*, *Fohsella peripheroacuta*, and *Globigerinoides mitra*.

Paleogene

Low-resolution planktonic foraminiferal evidence suggests that the middle Miocene unconformably overlies the lower Oligocene (Zone P18) at Site 1210. Alternatively, it is possible that dark-colored sediments in Cores 198-1210A-13H and 198-1210B-13H represent continuous but condensed sedimentation. Like the middle Miocene, the lower Oligocene and upper Eocene assemblages also show strong dissolution based on the abundance of foraminiferal fragments, low-diversity assemblages dominated by dissolution-resistant taxa, residues dominated by markedly smaller size fractions, and the presence of the authigenic mineral phillipsite. Samples 198-1210A-13H-CC and 198-1210B-13H-CC are assigned to lower Oligocene Zone P18 based on the presence of rare to abundant *Pseudohastigerina* spp. in the absence of late Eocene taxa such as *Turborotalia cerroazulensis* and *Hantkenina* spp. (including spines of this genus). Other taxa present include *Cassigerinella chipolensis*, "*Globigerina*" *euapertura*, *Catapsydrax dissimilis*, and *C. unicavus*, with or without rare "*Globigerina*" *ampliapertura*, *T. increbescens*, and *Globoquadrina tapuriensis*.

The upper Eocene of this site contains few planktonic foraminifers in the >63- μ m size fraction. Sample 198-1210B-14H-1, 7 cm, contains rare *Hantkenina* spines and fragments, *Subbotina angiporoides*, "*Globigerina*" *ampliapertura*, and common phillipsite and calcispheres. The assemblages in Samples 198-1210A-14H-CC and 198-1210B-14H-CC contain *Globigerinatheka senni*, *G. mexicana*, and *G. index* and are assigned to Zones P14–P16. Tektites were found in the former sample. Samples 198-1210A-15H-CC and 198-1210B-15H-CC are assigned to middle Eocene Zone P11 based on the presence of *Morozovella aragonensis*, *Globigerinatheka mexicana*, *G. subconglobata*, *G. senni*, *Acarinina bullbrooki*, *A. primitiva*, *A. pentacamerata*, *Guembelitrioides higginsii*, and rare, isolated spines of the genus *Hantkenina*. Zone P10 was not recognized in the low-resolution shipboard sampling, although we believe that the entire upper and middle Eocene sequence is complete based on the combined planktonic foraminiferal and calcareous nannofossil datums depicted in the age-depth plots (see "[Sedimentation and Accumulation Rates](#)," p. 21).

A more expanded lower Eocene section is present at Site 1210, a trend also observed at Site 1209. The interval from Sample 198-1210A-16H-CC through 198-1210B-17H-CC represents Zone P9, which is characterized by *Morozovella aragonensis*, *M. caucasica*, *Acarinina pentacamerata*, *A. quetra*, *A. soldadoensis*, and *Igorina broedermanni*. Zones P7 and P8 (Samples 198-1210A-18H-CC, 198-1210B-18H-CC, and 198-1210A-19H-CC) contain similar assemblages but are distinguished from the overlying sediments by the co-occurrence of *M. aragonensis*, *M. formosa*, and *M. subbotinae*; the FO of *A. pentacamerata* defines the boundary between these two zones. The section is more condensed in the basal Eocene. Sample 198-1210B-19H-CC is assigned to Zone P6 based on the absence of both *M. aragonensis* and *M. velascoensis*; the presence of *M. formosa* places this sample in Subzone P6b.

A continuous succession of upper Paleocene sediments was recovered in Core 198-1210A-20H through Section 23H-CC and Core 198-1210B-20H through Section 23H-CC. Zone P5 (Sample 198-1210A-20H-CC) contains a diverse planktonic assemblage including *Morozovella velascoensis*, *M. subbotinae*, *M. aequa*, *M. oclusa*, and *M. pasionensis*. This sample also contains the benthic foraminifer *Gavelinella beccariiiformis*, indicating a level below the benthic foraminiferal extinction event at the

onset of the PETM (Zachos et al., 1993). The absence of *M. subbotinae* and the presence of *Globanomalina pseudomenardii*, *Igorina pusilla*, *I. albeari*, *Acarinina nitida*, *A. mckannai*, and *A. subsphaerica* distinguish Zone P4 (Samples 198-1210A-21H-CC through 22H-CC and 198-1210B-20H-CC through 21H-CC) and its subzones. The co-occurrence of *M. angulata*, *M. conicotruncana*, and *I. pusilla* characterizes the sediments of Zone P3 (Samples 198-1210A-23H-CC and 198-1210B-22H-CC).

A prominent, 18 cm-thick magnetic susceptibility increase was found in Core 198-1210A-22H. This layer consists of a dark brown nannofossil ooze with clay. Preliminary micropaleontological investigations suggest that this interval as already identified in cores from Site 1209 may represent a previously unrecognized event of considerable evolutionary significance. This horizon lies within planktonic foraminiferal Zone P4 and coincides exactly with the evolutionary FO of the nannolith *Heliolithus kleinpellii*, an important component of the late Paleocene assemblages and a marker for the base of Zone CP5. Planktonic foraminifera are characterized by a low diversity and a largely dissolved assemblage dominated by representatives of *Igorina* (mainly *Igorina tadjikistanensis* and *Igorina pusilla*). The composition of the assemblage suggests some kind of oceanic perturbation.

The lower Paleocene (Danian) is condensed at Site 1210. Sediments of Zones P1 and P2 were not observed in core catcher samples. However, *Parvularugoglobigerina eugubina* (Zone P α) is present in Samples 198-1210A-24H-4, 24–25 cm, and 40–43 cm, and in Samples 198-1210B-24H-1, 5–6 cm, and 24H-1, 48–49 cm. Sample 198-1210B-24H-1, 5–6 cm, yields abundant woodringinids, which outnumber the low trochospiral group, including *P. eugubina*. The underlying sample (198-1210B-24H-1, 36–37 cm) is characterized by common larger *P. eugubina* with subordinate biserial heterohelicids. Few biserial woodringinids and chiloguembelinids in association with common *Guembelitra* and rare *P. eugubina* are present in Sample 198-1210B-24H-1, 48–49 cm.

Cretaceous

The highest occurrence of Cretaceous planktonic foraminifers is in Samples 198-1210A-24H-4, 49–50 cm, and 198-1210B-24H-1, 57–58 cm. This assemblage is extremely dissolved with few whole specimens. Fragments of Cretaceous specimens contribute >50% of the fine fraction (38–150 μ m), with the remaining part of the sample consisting of well-preserved tiny planktonic foraminiferal specimens that include *Guembelitra* and rare *Hedbergella holmdelensis*. Diverse assemblages of moderately to well-preserved planktonic foraminifers are present throughout the thick Campanian–Maastrichtian section cored at Site 1210. The *Abathomphalus mayaroensis* Zone (KS31) extends from the K/T boundary downward through Cores 198-1210A-27H and 198-1210B-25H, based on the presence of the nominal taxon. Additional taxa include *A. intermedius*, *Contusotruncana contusa*, *Globotruncana linneiana*, *G. orientalis*, *G. rosetta*, *Globotruncanella havanensis*, *G. petaloidea*, *Globotruncanita stuarti*, *G. stuartiformis*, *Heterohelix globulosa*, *H. rajagopalani*, *Pseudoguembelina costulata*, *P. excolata*, *Pseudotextularia elegans*, *P. nuttalli*, *Racemiguembelina fructicosa*, *Rugoglobigerina hexacamerata*, *R. rugosa*, and *Planoglobulina multicamerata*.

The FOs of *R. fructicosa* and *C. contusa* in Sample 198-1210B-27H-CC define a recognizable interval in the upper part of Zone KS30. The base of the *Gansserina gansseri* Zone (Zone KS30) is present in Sample 198-1210B-32H-CC. In addition to many of the taxa found in the overlying

A. mayaroensis Zone, other characteristic species found throughout Zone KS30 include the nominal taxon, *Contusotruncana fornicata*, *Globotruncana aegyptiaca*, *G. arca*, *G. bulloides*, and *G. falsostuarti*. The base of the *Globotruncana aegyptiaca* Zone (Zone KS29) is found in Sample 198-1210B-33H-CC. The total range of *Radotruncana calcarata* defines the base of the *Globotruncanella havanensis* Zone (Zone KS28) in Sample 198-1210B-35H-CC and the base of the *R. calcarata* Zone (Zone KS27) in Sample 198-1210B-39H-CC. The *Globotruncana ventricosa* Zone (KS26) is present to the bottom of the cored section at Site 1210.

Benthic Foraminifers

Benthic foraminifers were examined in selected core catcher samples from Holes 1210A and 1201B (Tables T5, T6). They are generally well preserved and rare to few in abundance in the Pleistocene through the Oligocene. The Eocene through Cretaceous section contains moderately preserved benthic foraminifers that are generally rare to few in abundance. The dissolution of planktonic foraminifers resulted in an increased relative abundance of benthic foraminifers in the upper to middle Miocene, in the Eocene/Oligocene boundary interval, and near the K/T boundary.

Neogene

In Samples 198-1210A-1H-CC through 10H-CC (Pleistocene–Pliocene), benthic assemblages are represented by abundant *Oridorsalis tener*, cibicidoidids (*Cibicidoides wuellerstorfi* and *C. mundulus*), uvigerinids (*Uvigerina hispida*, *U. hispidocostata*, *U. senticosa*, and *U. peregrina*), *Pyrgo murrhina*, *P. lucernula*, and several agglutinated taxa (*Eggerella bradyi*, *Karreriella bradyi*, and *Martinottiella* sp.). In Samples 198-1210A-10H-CC to 12H-CC, stilostomellids (*Stilostomella abyssorum*, *S. subspinosa*, *S. gracillima*, and *Stilostomella* spp.) replace the uvigerinids. These Miocene benthic assemblages are also characterized by *Oridorsalis tener* and nodosariids (*Dentalina* spp. and *Chrysalogonium longicostatum*).

Paleogene

Beneath the Oligocene–Miocene condensed interval or unconformity, Sample 198-1210A-13H-CC contains abundant *Bulimina jarvisi*, *Globocassidulina subglobosa*, and *Stilostomella subspinosa*. Other components of the benthic assemblage include *Oridorsalis umbonatus*, buliminids (*B. elongata* and *B. impendens*), and *Vulvulina spinosa*. Upper Eocene Sample 198-1210A-14H-CC contains well-preserved and abundant benthic foraminifers. This assemblage is dominated by very large specimens of *Plectofrondicularia paucicostata*. *Nuttallides truempyi*, *O. umbonatus*, some cibicidoidids (*Cibicidoides eocaenus* and *C. havanensis*), *Dentalina* spp., *Bulimina jarvisi*, and *V. spinosa* are also present in this sample. In Sample 198-1210A-16H-CC, species such as *Alabamina dissonata*, *N. truempyi*, *Dentalina* spp., buliminids (*B. impendens*, *B. jarvisi*, and *B. semicostata*), and stilostomellids (*Stilostomella* spp. and *S. gracillima*) characterize the benthic assemblages.

The preservation and size of benthic foraminiferal tests decrease in lower Eocene (Samples 198-1210A-17H-CC through 19H-CC). Few benthic foraminifers are present in the >250- μ m range. Small trochospiral forms (*Nuttallides truempyi*, *Oridorsalis umbonatus*, and *Clinapertina complanata*), *Dentalina* spp., abundant *Bulimina jarvisi*, and *B. semicos-*

T5. Cenozoic and Cretaceous benthic foraminifers, Hole 1210A, p. 74.

T6. Cenozoic and Cretaceous benthic foraminifers, Hole 1210B, p. 76.

tata characterize benthic assemblages in this interval, although buliminids are absent in Sample 198-1210A-19H-CC.

The Paleocene benthic assemblages of Samples 198-1210A-20H-CC to 23H-CC and 198-1210B-23H-CC contain various trochospiral forms (*Conorbinoides hillebrandti*, *Gyroidinoides globosus*, *Nuttallides truempyi*, *Oridorsalis umbonatus*, and *Osangularia plummerae*), *Aragonia ouezzanensis*, *A. velascoensis*, *Lenticulina* spp., and *Buliminella grata*. Although sporadic in their distribution, agglutinated taxa (*Spiroplectamina jarvisi* and *Tritaxia* spp.) are also present in this interval.

Cretaceous

Benthic assemblages in Samples 198-1210A-24H-CC to 26H-CC and 198-1210B-24H-CC to 32H-CC are represented by trochospiral species (*Conorbinoides hillebrandti*, *Nuttallides truempyi*, *Oridorsalis umbonatus*, and *Sliterella lobulata*), *Dentalina* spp., *Lenticulina* spp., and agglutinated taxa (*Gaudryina pyramidata* and *Marssonella trochoides*). Although they are sporadically present, *Aragonia velascoensis* and *Pyramidina szajnochae* are also characteristic taxa in this section.

In Samples 198-1210A-34H-CC through 42H-CC, *Aragonia velascoensis*, *A. ouezzanensis*, and the agglutinated species *Gaudryina pyramidata* and *Marssonella trochoides* are characteristic benthic foraminifers. Other important components of the benthic assemblages are similar to those observed in the upper part of the section.

Paleodepth

Paleodepth estimates are based on the work of Pflum et al. (1976), Tjalsma and Lohmann (1983), Woodruff (1985), and van Morkhoven et al. (1986) for the Neogene and Paleogene section. For the Cretaceous section, estimates are mainly based on the study of Nyong and Olsson (1984) and backtracked paleodepth-curve based on DSDP and ODP data from Kaiho (1999).

From the Neogene through Cretaceous, the observed benthic assemblages at Site 1210 are generally similar to those from Sites 1207–1209. Neogene paleowater depth is estimated to be upper abyssal (2000–3000 m) based on the presence of the characteristic forms as uvigerinids (*Uvigerina hispida*, *U. hispidocostata*, and *U. senticosa*), *Pyrgo murrhina*, *P. lucernula*, *Eggerella bradyi*, *Karrerella bradyi*, and *Martinottiella* sp. (Pflum et al., 1976; van Morkhoven et al., 1986).

Nuttallides truempyi, *Oridorsalis umbonatus*, *Aragonia ouezzanensis*, *A. velascoensis*, buliminids, and stilostomellids characterize Paleogene benthic assemblages. These also indicate water depths similar to those of the Neogene section (Tjalsma and Lohmann, 1983), but slightly shallower depths in the early Paleocene are suggested by the presence of such forms as *Gyroidinoides globosus*, *Lenticulina* spp., and buliminids (Tjalsma and Lohmann, 1983).

Trochospiral calcareous benthic foraminifers (*Conorbinoides hillebrandti*, *Gyroidinoides globosus*, *Nuttallides truempyi*, *Oridorsalis umbonatus*, *Osangularia plummerae*, and *Sliterella lobulata*) are characteristic taxa of Cretaceous benthic assemblages, and they indicate a wide bathymetric range (1500–4000 m) (Kaiho, 1998, 1999). *Pyramidina szajnochae* is found in Samples 198-1210B-28H-CC and 30H-CC, is one of the characteristic taxa of the Late Cretaceous, and is considered to indicate uppermost abyssal depth (2000–2500 m) (Nyong and Olsson, 1984). Furthermore, another dominant component, *Aragonia velascoen-*

sis, which is indicative of lower bathyal depths (1500–2000 m) (Nyong and Olsson, 1984), becomes more dominant during the Campanian. In summary, this site shows a deepening upward trend from lower bathyal depths during the Campanian to upper abyssal depths during the Cenozoic.

PALEOMAGNETISM

Archive halves of core sections from Holes 1210A and 1210B were measured on the shipboard pass-through magnetometer unless they displayed obvious and pervasive coring disturbance. Of the 27 APC cores from Hole 1210A, measurements were made from each except for Core 198-1210A-26H, which contained 1.24 m of disturbed material. From Hole 1210B, all cores were measured except Cores 198-1210B-36H, 39H, and 40H, which contained flow-in sediments. As at previous sites, most of the data from cores of the Oligocene–Paleocene and Cretaceous age are uninterpretable. This is attributed largely to deformation of these soft sediments during drilling, core recovery, or core splitting.

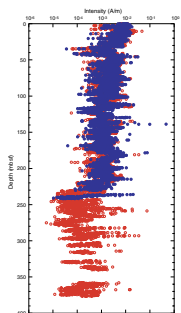
As before, the natural remanent magnetization (NRM) of core sections was measured at 5-cm intervals, followed by measurement after two alternating-field (AF) demagnetization steps (10- and 20-mT peak fields). When time was available, additional AF demagnetization steps (usually at peak fields of 15 mT) were carried out. NRM intensity values typically stayed within a narrow range, from $\sim 10^{-2}$ to 10^{-1} A/m; however, a few cores had intensity spikes with values higher than 1 A/m. After AF demagnetization at 20 mT (to remove the drill string overprint), intensity values were generally from $\sim 2 \times 10^{-4}$ to 2×10^{-2} A/m. A slow decline in intensity of about one order of magnitude was observed with depth from the surface to 220 mbsf (Fig. F12). Below this depth, an abrupt decrease in magnetization intensity occurs, with a factor of 10 reduction, in the weakly magnetic Maastrichtian and Campanian sediments (see “Lithostratigraphy,” p. 7). Many cores in the Cretaceous section have intensities close to the noise level for the shipboard pass-through cryogenic magnetometer, especially in the depth range of 230–280 mbsf, where 20-mT demagnetized intensities decline to as low as $\sim 3 \times 10^{-5}$ A/m.

Paleomagnetic data acquired from the shipboard pass-through magnetometer from Site 1210 produced an interpretable magnetic polarity stratigraphy in the upper ~ 100 meters composite depth (mcd). In this uppermost Miocene, Pliocene, and Pleistocene section, it was possible to recognize polarity zones corresponding to the Brunhes Chron (C1n) and to the Gilbert Chron (C3n) in both holes (Fig. F13). Directly below C3n, several normal polarity chrons were evident in both holes, but the polarity zone pattern is ambiguous. The next two polarity zones below the zone correlative to C3n–C4n were interpreted as correlative to C3An (Fig. F13).

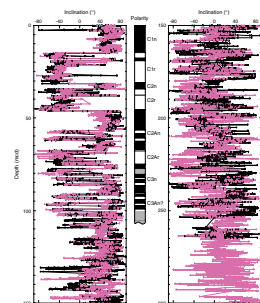
Measurements on cores deeper than 100 mcd showed erratic inclination values and poor correlation between holes (Fig. F13), making it impossible to make any polarity interpretations for the Oligocene to Cretaceous section. As at previous sites, the problem is attributed to the soft and easily deformed nature of the sediments, which compromises the pass-through measurements.

Polarity chrons recognized in the upper 100 mcd of the section yield an age-depth curve for the upper Miocene–Pleistocene sediments (Fig.

F12. Archive-half magnetization intensities after AF demagnetization at peak fields of 20 mT, p. 45.



F13. Inclination after AF demagnetization at peak fields of 20 mT, Holes 1210A and 1210B, p. 46.



F14. The sedimentation rate was nearly constant for the last ~5 m.y., although slight variations in slope suggest an increase during Pliocene time, from 12 to 19 m/m.y., before a slight reduction to 16 m/m.y. for the last 2 m.y. Prior to 5 Ma, the sedimentation rate appears to have been about half as large (Fig. F14).

COMPOSITE DEPTHS

MST and spectral reflectance (L^*) data collected from Holes 1210A and 1210B were used to determine depth offsets in the composite section. Magnetic susceptibility, GRA bulk density, and spectral reflectance measurements were the primary parameters used for core-to-core correlation. GRA bulk density and magnetic susceptibility data were collected at 3-cm intervals, and spectral reflectance data were collected at 2.5-cm intervals on all cores (see “MST Measurements,” p. 27, in “Physical Properties” and “Lithostratigraphy,” p. 7, for details about MST and spectral reflectance data).

The data used to construct the composite section and determine core overlaps are presented in a composite depth scale in Figure F15. The depth offsets that comprise the composite section for Holes 1210A and 1210B are given in Table T7. Units for the composite depth scale are mcd.

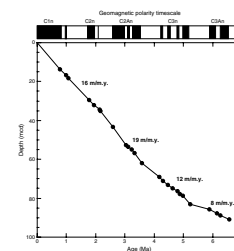
The composite data show that the APC cores from Site 1210 provide a continuous overlap to at least 260 mcd (K/T boundary; 244 mcd in Core 198-1210A-23H). Below the uppermost Maastrichtian, most of the cores from Holes 1210A and 1210B could not be correlated and placed into a composite depth framework. Expansion of sedimentary features in one hole relative to coeval cores in the other hole indicate distortion of the cored sequence. Because some distortion occurred within individual cores on depth scales of <9 m, it was not possible to accurately align every feature in the MST and color reflectance records by simply adding a constant to the mbsf core depth.

Following construction of the composite depth section for Site 1210, a single spliced record was assembled for the aligned cores over the upper 260 mcd by using cores from both holes. Intervals having significant disturbance or distortion were avoided. The PETM interval in the composite was taken from Core 198-1210B-20H. Magnetic susceptibility data from both holes for the middle Miocene–lower Oligocene unconformity interval are shown in Figure F16. The Site 1210 splice (Table T8) can be used as a guide to sample a single sedimentary sequence between 0 and 260 mcd and can be used to plot other data sets from this site.

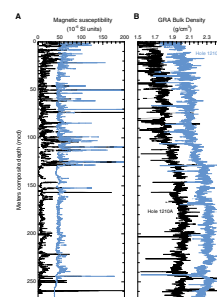
SEDIMENTATION AND ACCUMULATION RATES

Unconformities and changes in sedimentation rate at Site 1210 are illustrated in a plot of calcareous microfossil datum ages (first and last occurrences) vs. depth (Fig. F17). These rates rely on major calcareous nannofossil and planktonic foraminiferal datums presented in Tables T3 and T4. The Pleistocene–Campanian section cored at Site 1210 is possibly punctuated by one major unconformity between the lower Miocene and lower Oligocene, as well as an interval of diastems and/or multiple condensed intervals in the middle Miocene to lower Miocene and upper to middle Eocene.

F14. Age-depth curve derived from magnetic stratigraphy, p. 47.

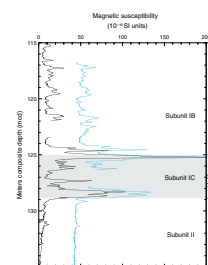


F15. Magnetic susceptibility data and GRA bulk density data, p. 48.



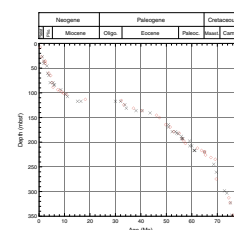
T7. Composite depth section, p. 77.

F16. Magnetic susceptibility data, 115 to 135 mcd, p. 49



T8. Splice tie points, p. 78.

F17. Age-depth plot of calcareous nannofossil and planktonic foraminiferal datums, p. 50.



ble T9). The noncarbonate fraction, composed largely of clay and volcanic ash, became more significant during the last 5.5 m.y., making up an average of 23 wt% of the accumulating sediment.

ORGANIC GEOCHEMISTRY

Volatile Hydrocarbons

Headspace gas analysis was conducted as part of the standard protocols required for shipboard safety and pollution prevention monitoring. A total of 17 cores from Hole 1210A were evaluated (Table T10). The concentrations of CH₄ were at background levels (range = 1.7–2.2 μL/L [ppmv]); no hydrocarbon gases higher than C₁ were detected.

Carbonate

Carbonate determinations by coulometry were made for a total of 106 samples from Hole 1210A and 25 samples from Hole 1210B (Table T11). Samples were selected to provide a measure of the carbonate content within different units and to assess the influence of carbonate content on color reflectance. In addition, parts of Cores 198-1210A-14H and 20H within Unit II were sampled at 20-cm intervals to calibrate reflectance profiles with carbonate contents. The carbonate content ranges from 24 to 92 wt% (Table T11; Fig. F23) in Unit I. The low values in Unit I come from condensed intervals enriched in clay, notably in Core 198-1210A-13H at the base of the unit. There also is a general trend toward increasing carbonate with increasing depth in this unit (Fig. F23). A similar trend is discernible in Unit II, where the median value for the carbonate contents of the nannofossil ooze is 95.1 wt%. Again the low values, including the minimum of 1.3 wt% for Sample 198-1210A-23H-6, 71 cm, correspond to clay-rich condensed intervals. The nannofossil ooze in Unit III possesses uniformly high carbonate contents (mean = 96.7 wt%).

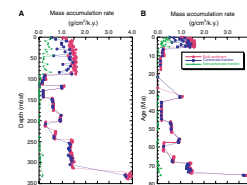
Elemental concentrations of C, H, N, and S were measured for a few samples in Unit I (Table T12). The contents of organic carbon were low in all samples and decreased with depth. Their C/N ratios, when organic carbon was measured, were indicative of algal material. Sample 198-1210A-26H-CC, 1 cm, consists of brown-black blebs containing 27.7 wt% carbonate (Table T11) that are associated with pyritized burrows. However, it contains no organic carbon or sulfur (Table T12); XRD analysis of a decalcified sample indicates that the blebs are hydrated Ba/Mn oxide (romanechite: Ba_{0.65}Mn₅O₁₀ · 1.3H₂O).

INORGANIC GEOCHEMISTRY

Interstitial Water Chemistry

A total of 15 interstitial water samples were collected in Hole 1210A: 11 samples between 0 and 100 mbsf (one sample per core) and 5 between 144.8 and 230.3 mbsf. Sample resolution was decreased down-core to preserve critical stratigraphic intervals (e.g., Eocene/Oligocene boundary). A total of 19 samples were collected in Hole 1210B: 18 between 0 and 100 mbsf and 1 at 284.8 mbsf. The samples from 0 to 100 mbsf for Hole 1210B were collected for postcruise analyses. With the ex-

F22. Mass accumulation rates vs. age and depth for the Campanian–Pleistocene, p. 55.

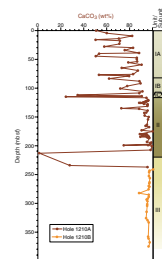


T9. Linear sedimentation rate segments and average accumulation rates, p. 79.

T10. Headspace CH₄ concentrations, p. 80.

T11. Carbonate content, p. 81.

F23. Carbonate profiles, p. 56.



T12. Results from CNSH analysis, p. 82.

ception of chloride titrations, the shipboard analytical suite was not produced for these samples. The deep interstitial water sample in Hole 1210B was collected after a significant change in sediment lithology was observed at ~260 mbsf; this lithological shift was not encountered in Hole 1210A, which extends only to ~240 mbsf. Details of analytical methods can be found in *“Inorganic Geochemistry,”* p. 21, in the *“Explanatory Notes”* chapter. Filtered (0.45 μm) samples were analyzed for pH, salinity, chlorinity, alkalinity, sulfate (SO_4^{2-}), phosphate (HPO_4^{2-}), ammonium (NH_4^+), silica ($\text{Si}(\text{OH})_4$), boron (H_3BO_3), iron (Fe^{2+}), manganese (Mn^{2+}), and major cations (Na^+ , K^+ , Mg^{2+} , Ca^{2+} , Li^+ , Sr^{2+} , and Ba^{2+}). A compilation of data is provided in Table T13. Cited values for average seawater composition are from Millero and Sohn (1992) and Broecker and Peng (1982).

pH, Salinity, Chloride, and Sodium

At Site 1210, there is little variation in the pH of the interstitial waters (7.37 ± 0.07) (Table T13). As at Site 1209, variability of the pH profile (0–100 mbsf) may be a consequence of variations in sediment composition. The relatively narrow range of values below ~100 mbsf reflects the buffering capacity of the carbonate-dominated sediment, whereas the variation in the upper section of the profile may be a consequence of a higher proportion of noncarbonate material (e.g., biogenic silica, ash, and detrital silicates) (see *“Lithostratigraphy,”* p. 7). Salinity remains at 35 g/kg throughout the profile.

The chloride (Cl^-) profile exhibits slight fluctuations (Fig. F24). Concentrations increase from 553 mM in the shallowest sample (4.45 mbsf) to 569 mM at the bottom of the profile at 284.8 mbsf (Table T13). Sodium (Na^+) concentrations, calculated by charge balance using the methods described by Broecker and Peng (1982), show only a slight increase downcore from 469 mM (4.45 mbsf) to 483 mM near the bottom of the profile (Table T13).

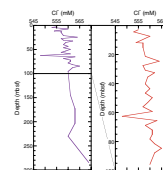
Alkalinity, Sulfate, Ammonium, Phosphate, Iron, and Manganese

As in Hole 1209A, the effects of organic matter reactions are subdued (Fig. F25). The SO_4^{2-} concentrations decrease steadily from 29 mM in the shallowest sample (4.45 mbsf) to 23 mM at the base of the profile. Given that sulfate reduction tends to increase alkalinity at the rate of 2 moles of HCO_3^- per mole of SO_4^{2-} reduced, a downcore increase in alkalinity of ~10 mM would be expected. Alkalinity values, however, are low throughout the profile (2.92 ± 0.34 mM) and decrease downcore from ~3.30 to 2.40 mM (Fig. F25). The difference between the observed and expected alkalinity implies that 7–10 mM of HCO_3^- have been removed from the system, possibly by precipitation of carbonate minerals. Phosphate (HPO_4^{2-}) and ammonium (NH_4^+) concentrations range from 0 to 3 μM and 61 to 118 μM , respectively. Although the NH_4^+ pore water content is approximately twice that in Hole 1209A, the downcore concentrations are significantly less than at Sites 1207 and 1208, implying that there is little organic matter within the sedimentary section at Site 1210 (see *“Carbonate”* p. 23, in *“Organic Geochemistry”*).

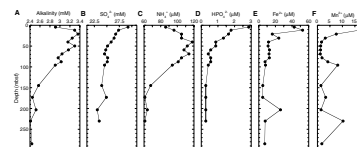
The Fe^{2+} and Mn^{2+} concentrations decrease significantly through the upper ~40 m of their respective profiles (Fig. F25). The Fe^{2+} concentrations decrease from 53 to 12 μM over this interval; the lower part of the

T13. Results of geochemical analyses, p. 83.

F24. Chloride ion concentrations, p. 57.



F25. Alkalinity, sulfate, ammonium, phosphate, iron, and manganese profiles, p. 58.



Fe²⁺ profile is uniform with average concentrations of $9 \pm 3 \mu\text{M}$, with the exception of a single excursion to $27 \mu\text{M}$ at 203.35 mbsf. This variation occurs in proximity to the K/T boundary, where clays with pyrite blebs and oxides are likely related to the deviation in pore water Fe²⁺ concentrations (see “**Lithostratigraphy**,” p. 7).

The shape of the Mn²⁺ profile at Site 1210 is similar to those at Sites 1207, 1208, and 1209 (Fig. F25), implying that similar processes are controlling Mn²⁺ concentrations in the pore waters. Manganese concentrations decrease from $18 \mu\text{M}$ (4.45 mbsf) to $1 \mu\text{M}$ at ~ 40 mbsf. Two large positive excursions occur in the lower section of the profile at Site 1210; $8 \mu\text{M}$ (95.85 mbsf) and $10 \mu\text{M}$ (230.80 mbsf). As in Hole 1209A, these deviations coincide with a number of condensed intervals containing inferred Mn-rich phases (see “**Lithostratigraphy**,” p. 7). Consequently, the increase in Mn²⁺ concentrations is interpreted to reflect the dissolution of Mn-minerals and diffusion of Mn²⁺ away from two separate Mn-rich horizons.

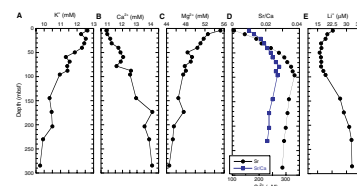
Potassium, Calcium, Magnesium, Lithium, and Strontium

Potassium (K⁺) concentrations gradually decrease downcore from a maximum of 12.6 mM in the shallowest sample (4.45 mbsf) to values slightly less than that of average seawater (10.2 mM) in the deepest sample at 284.80 mbsf (Fig. F26). Elevated concentrations may correspond to the occurrence of volcanic ash in the upper ~ 80 m of the hole (see “**Lithologic Unit I**,” p. 7, in “**Lithostratigraphy**”), suggesting that K⁺ is liberated from glass-rich, silicic volcanic material via leaching and weathering reactions that produce clays (i.e., smectite). The downcore decrease in K⁺ is interpreted to reflect the absence of ash relative to the overlying sediments, diffusion of K⁺ toward greater depths, and possible exchange with basaltic basement.

As at Site 1209, concentrations of Ca²⁺ and Mg²⁺ in the upper pore waters at Site 1210 are close to average seawater (10.3 and 53.2 mM, respectively) and show an inverse relationship downcore (Fig. F26): Ca²⁺ concentrations increase downcore from 10.9 to 14.1 mM, whereas Mg²⁺ concentrations decrease from 55.3 to 44.6 mM. The most likely influences on the downcore distribution of Ca²⁺ and Mg²⁺ cations are calcium carbonate dissolution (releases Ca²⁺) and weathering reactions involving volcanic ash and/or basement (release Ca²⁺ and consume Mg²⁺). However, Ca²⁺ continues to increase below the depth of maximum Sr²⁺ concentration, which suggests that carbonate dissolution may not be the source of excess. The distribution of Mg²⁺ may also be influenced by the formation of Mg phases (i.e., saponite), observed intermittently throughout lithologic Unit I as green laminae (see “**Lithologic Unit I**,” p. 7, in “**Lithostratigraphy**”). The relative contribution of Ca²⁺ and Mg²⁺ to interstitial waters by these processes cannot be determined from the available data.

Initially, the concentration of Li⁺ in Holes 1210A and 1210B (Fig. F26) decreases from $23 \mu\text{M}$ to a minimum of $16 \mu\text{M}$ at 49.85 mbsf. Below this depth, Li⁺ cation concentrations increase linearly to $33 \mu\text{M}$ at 284.4 mbsf. The lower concentrations through the upper ~ 50 m of the profile may reflect Li⁺ adsorption to clay minerals forming through the weathering of volcanic material and, possibly, zeolites (Gieskes, 1981). The similarity of the Li⁺ profile to the Ca²⁺ profile (increasing concentration with depth), and the inverse relationship between these and the

F26. Potassium, calcium, magnesium, strontium, and lithium profiles, p. 59.



Mg²⁺ and K⁺ profiles, implies that weathering reactions involving volcanic basement may be adding Li⁺ to pore waters. Geochemical studies of seafloor vent systems have demonstrated that significant quantities of Li⁺ may be released as a consequence of exchange between seawater and basalt, even at low temperatures (Millero and Sohn, 1992).

The similar curvature of the Sr²⁺ and Sr/Ca pore water profiles (Fig. F26) suggests that the highest rate of carbonate dissolution and/or recrystallization is occurring within the upper ~100 m of the sediment column (e.g., Baker et al., 1982). Below this depth, there is little change in either the Sr²⁺ or Sr/Ca profile, indicating that little additional Sr²⁺ is being added to the system. The lack of variability in the lower part of the profile indicates the sediment has not been buried to a depth sufficient for the onset of pressure solution.

Silica

The downcore dissolved silica (Si(OH)₄) profile is similar to those observed at Sites 1207, 1208, and 1209 (Fig. F27). Pore water silica concentrations average 619 ± 60 μM in the upper ~100 m of the profile, decrease sharply to 229 μM at 144.80 mbsf, and remain low and uniform (226 ± 25 μM) down to 284.8 mbsf. The elevated concentrations in the upper part of the profile are interpreted to reflect the leaching and weathering of volcanic ash in Neogene sediments. Lower pore water Si(OH)₄ concentrations likely correspond to a decrease in ash content and the appearance of chert in calcareous sediments. The removal of Si(OH)₄ from pore waters may be induced by the recrystallization of opal-A to opal-CT or quartz (Baker, 1986; Gieskes, 1981).

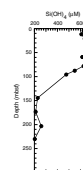
Boron and Barium

At Site 1210, dissolved boron (H₃BO₃) concentrations are relatively uniform (459 ± 58 μM), with one significant negative excursion at 30.85 mbsf (282 μM). Above 100 mbsf, the Ba²⁺ concentrations average 0.4 ± 0.2 μM and show only slight variability. Although Ba²⁺ concentrations in the upper half of the profile are extremely low, they are, on average, higher than those of average seawater, indicating that Ba²⁺ is being added to the pore waters. Possible sources of Ba²⁺ include leaching and/or dissolution of skeletal debris and volcanic ash. The significance of variations in the H₃BO₃ and Ba²⁺ concentrations in pore waters of pelagic sediments is not well understood. Pore water of these constituents profiles at Site 1210 are described largely for purposes of documentation. The data are provided in Table T13.

PHYSICAL PROPERTIES

Physical properties at Site 1210 were measured on both whole-round sections and discrete samples from split-core sections. Continuous whole-round measurements were made of magnetic susceptibility, GRA bulk density, and compressional *P*-wave velocity, using the MST for all Site 1210 cores. Whole-round sections of Hole 1210A cores were also measured for natural gamma radiation using the MST. Discrete measurements of compressional *P*-wave velocity were made at a frequency of at least one measurement per split-core section in Holes 1210A and 1210B. Index properties were measured on discrete samples from split-

F27. Silica profile, p. 60.



core sections at a frequency of one measurement per section throughout Hole 1210A and in Cores 198-1210B-26H to 42H.

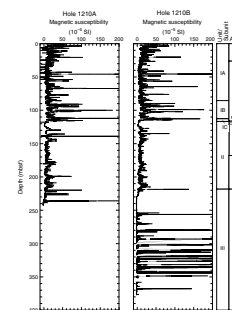
MST Measurements

All core sections from Holes 1210A and 1210B were routinely measured on the MST for magnetic susceptibility and GRA density at 3-cm intervals (Figs. F28, F29). MST *P*-wave velocity was also routinely measured at 10-cm intervals in all cores from the two holes (Fig. F30). Natural gamma radiation was measured on the MST at 30-cm intervals in Hole 1210A cores only (Fig. F31). All collected MST data are archived in the ODP Janus database.

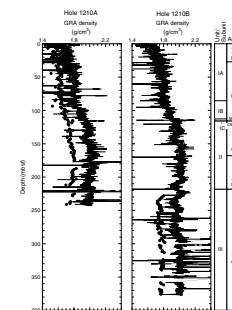
Magnetic susceptibility values (Fig. F28) are generally highest in the uppermost ~116 m of the Site 1210 sedimentary column (lithologic Unit I; see “**Lithologic Unit I,**” p. 7, in “Lithostratigraphy”). The relatively lower magnetic susceptibility values in the sediments below ~116 mbsf occur within lithologic Unit II, which has higher carbonate contents. Peaks in magnetic susceptibility in lithologic Subunits IA and IB may correlate with distinctive ash layers (see “**Lithologic Unit I,**” p. 7, in “Lithostratigraphy”). In the middle Pleistocene–Miocene section an excellent correlation is observed between magnetic susceptibility and color reflectance data, primarily the total reflectance value (L^*) and the 550-nm wavelength (see “**Lithologic Unit I,**” p. 7, in “Lithostratigraphy”). Both magnetic susceptibility and color reflectance data in this interval reveal a pronounced cyclicity, which will be useful in identifying astronomically controlled depositional processes. Magnetic susceptibility values are generally higher in lithologic Subunit IC, relative to Subunit IB. As already observed at Site 1209, a small downhole increase in magnetic susceptibility (at ~112.8 mbsf) characterizes the middle Miocene/lower Oligocene unconformity at Site 1210 (see “**Biostratigraphy,**” p. 13). Miocene lithologic Subunit IC and Paleocene–Oligocene lithologic Unit II are generally characterized by fairly constant magnetic susceptibility values. Small-magnitude peaks in magnetic susceptibility occur within Unit II (e.g., at ~198 mbsf) (see “**Principal Results,**” p. 1). The K/T boundary is marked in Holes 1210A and 1210B by a large peak in magnetic susceptibility values, associated with an increase in clay content (see “**Organic Geochemistry,**” p. 23). In lithologic Unit III, magnetic susceptibility values are generally close to background, except for some short-lived excursions that are related to chert horizons, and do not exhibit any consistent downhole variation.

MST GRA bulk density data exhibit a general downhole increase in magnitude in the upper 115 m of the sediment column (Fig. F29), resulting from sediment compaction and dewatering processes with increased overburden pressure. GRA bulk density data also show distinct variations that relate to lithologic changes at distinct horizons, for example the middle Miocene/lower Oligocene unconformity and the Cretaceous/Paleogene boundary. Cyclic variation in GRA bulk density values, similar to that evident in magnetic susceptibility and color data (see “**Lithologic Unit I,**” p. 7, in “Lithostratigraphy”), is found within Pleistocene–Pliocene lithologic Subunits IA and IB. Lithologic Subunit IC (~112 to ~116 mbsf) is characterized by higher GRA bulk density values. GRA bulk density values also display rhythmic changes between ~116 and ~220 mbsf that are related to cyclic variations in sediment composition, such as carbonate content (see “**Organic Geochemistry,**” p. 23).

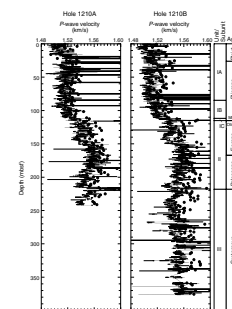
F28. Whole-core MST magnetic susceptibility, p. 61.



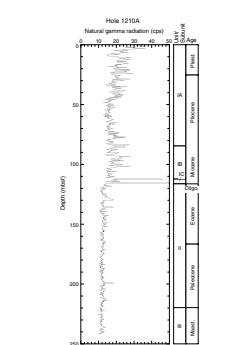
F29. Whole-core MST GRA and discrete bulk density vs. depth, p. 62.



F30. Whole-core MST and discrete *P*-wave velocity vs. depth, p. 63.



F31. MST natural gamma radiation vs. depth, p. 64.



GRA bulk density values are consistently higher than the discrete wet bulk density measurements (Fig. F29; Table T14) throughout Hole 1210A and Hole 1210B. These overestimated GRA bulk density values can be explained by the relatively high carbonate content, porosity, and water content of sediments; the calibration procedure for the MST GRA sensor is optimized for mixed-lithology sediments. Consequently, the GRA method overestimates the density in carbonate-rich sediments. This phenomenon is most pronounced in lithologic Unit III because these sediments have the highest carbonate contents (see “Organic Geochemistry,” p. 23).

MST *P*-wave velocities were recorded at 10-cm intervals in Holes 1210A and 1210B (Fig. F30). Despite some obviously “out of range” values, a general trend to higher velocities with increased depth in the sediment column can be discerned from values lying between ~1500 and ~1600 m/s. MST *P*-wave values generally increase with depth through lithologic Unit I and the upper half of Unit II from 0 to ~150 mbsf, whereas they decrease downhole from ~150 to ~215 mbsf. Between ~110 and ~120 mbsf, *P*-wave values increase relatively abruptly from ~1525 to ~1550 m/s. At ~220 mbsf there is a relatively abrupt increase in *P*-wave velocity that is associated with the K/T boundary and the boundary between lithologic Units II and III. In lithologic Unit III, MST *P*-wave values maintain an almost constant velocity of ~1550 m/s. The downhole trend recorded by the reliable MST *P*-wave logger (PWL) values also compare well with the discrete measurements of *P*-wave velocity (see Table T15; Fig. F32). However, MST PWL values are consistently lower than discrete values (most pronounced in the Paleocene and upper Maastrichtian sediments); this difference may be due to the assumption in the calibration of the MST PWL that the core liner is full of sediment and that there is no water between the liner and the sediment.

Natural gamma radiation data were collected at 30-cm intervals on cores from Hole 1210A only (Fig. F31). Peak natural gamma radiation values occur at the middle Miocene–lower Oligocene unconformity and in upper Eocene and upper Paleocene sediments; high values indicate small increases in clay content in the sedimentary record (see “Lithologic Unit I,” p. 7, and “Lithologic Unit II,” p. 9, in “Lithostratigraphy,” p. 7). Below 135 mbsf, natural gamma radiation values remain generally constant with increase in burial depth.

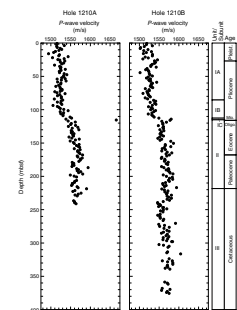
***P*-Wave Velocity**

Discrete measurements of compressional *P*-wave velocity were made on Site 1210 split-core sections using the modified Hamilton frame (PWS3) velocimeter. These data are listed in Table T15 and illustrated in Figure F32. Data were collected at a routine sampling frequency of one measurement per section. Velocities vary between ~1520 m/s in the soft surface sediments and ~1570 m/s in the more consolidated sediments. Discrete *P*-wave measurements show a general downhole increase in velocity between 0 and ~380 mbsf, which is similar to that evident in the reliable data obtained with the MST PWL. The lack of evidence for early diagenetic cementation near the seafloor, as shown by high-percentage porosity in the interval 0–100 mbsf (Fig. F33; Table T14), suggests that increasing *P*-wave velocity with depth in the upper 100 m of the sedimentary column is primarily the consequence of compaction and pore fluid expulsion. An increase in discrete *P*-wave velocities between 0 and ~120 mbsf broadly correlates with an increase in the magnitude of discrete bulk density values (Fig. F33). *P*-wave values then exhibit an

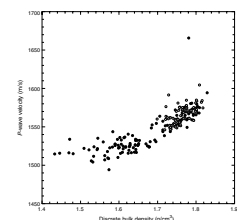
T14. Discrete measurements of *P*-wave velocity, p. 84.

T15. Discrete index properties measurements, p. 86.

F32. Discrete *P*-wave velocities, p. 65.



F33. *P*-wave velocities vs. wet bulk density, p. 66.



abrupt increase between ~100 and ~120 mbsf, from ~1520 to ~1570 m/s. *P*-wave velocities between ~120 and 380 mbsf remain relatively constant at a value of ~1570 m/s. Recorded *P*-wave velocities in the upper part of lithologic Unit III are slower than those measured at the base of this sedimentary interval; this variation may be due to increased lithification of the Cretaceous sediments with greater burial depth.

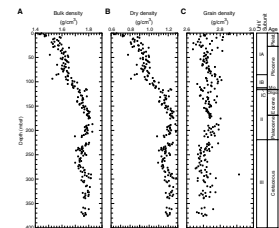
Index Properties

Index properties were determined for discrete samples from Hole 1210A and Cores 198-1210B-26H to 42H. These data are listed in Table T14 and shown in Figures F34 and F35. Index properties primarily reflect progressive sediment compaction and fluid expulsion with depth in the sediment column, but also indicate changes in sediment composition as defined by lithologic units and subunits (see “**Lithostratigraphy**,” p. 7). Bulk and dry density increase in magnitude between the seafloor and ~120 mbsf, within lithologic Unit I. Bulk and dry density continue to increase to maximum values at ~210 mbsf in lithologic Unit II. Between 220 and ~300 mbsf, both bulk and dry density generally decrease. By comparison, grain density exhibits a small general downhole decrease in magnitude from 0 to ~380 mbsf. Water content, porosity, and void ratio all exhibit a general downhole decrease between the seafloor and ~180 mbsf, within lithologic Unit I (Pleistocene–Oligocene) and the Eocene portion of Unit II. Water content, porosity, and void ratio increase slightly between ~180 and ~270 mbsf, within the Paleocene portion of lithologic Unit II and upper part of lithologic Unit III (Cretaceous). These trends suggest that overburden on the Cretaceous sediments was not sufficient to cause significant downhole water loss and decrease in porosity.

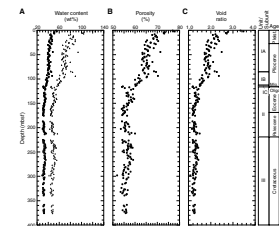
Summary

Physical properties data at Site 1210 show variation with depth below seafloor that suggests control by progressive compaction and fluid expulsion in the upper ~180 m. As at Site 1209, a simple relationship between lithology and physical properties is less obvious than at Sites 1207 and 1208. The absence of such a relationship may in part be due to the more continuous Late Cretaceous–Holocene sedimentation at Site 1210 and, hence, the absence of major unconformities spanning long periods of geologic time. As for Site 1209, the unusual physical properties data from below ~180 mbsf cannot be explained only by the sediment burial history. The physical properties data suggest that there has been less diagenesis and compaction in the sediments below 180 mbsf, relative to those in the interval ~95–180 mbsf. This may be a reflection of varying microfossil composition within the Site 1210 sediments and the so-called “diagenetic potential” of different sediments (see “**Physical Properties**,” p. 29, in the “Site 1209” chapter).

F34. Wet bulk, dry, and grain density vs. depth, p. 67.



F35. Water content, porosity, and void ratio vs. depth, p. 68.



REFERENCES

- Baker, P.A., 1986. Pore-water chemistry of carbonate-rich sediments, Lord Howe Rise, Southwest Pacific Ocean. In Kennett, J.P., von der Borch, C.C., et al., *Init. Repts. DSDP, 90* (Pt. 2): Washington (U.S. Govt. Printing Office), 1249–1256.
- Baker, P.A., Gieskes, J.M., and Elderfield, H., 1982. Diagenesis of carbonates in deep-sea sediments—evidence from Sr²⁺/Ca²⁺ ratios and interstitial dissolved Sr²⁺ data. *J. Sediment. Petrol.*, 52:71–82.
- Barrera, E., Savin, S.M., Thomas, E., and Jones, C.E., 1997. Evidence for thermohaline-circulation reversals controlled by sea level change in the latest Cretaceous. *Geology*, 25:715–718.
- Berger, W.H., Kroenke, L.W., Mayer, L.A., and Shipboard Scientific Party, 1991. Ontong Java Plateau, Leg 130: synopsis of major drilling results. In Kroenke, L.W., Berger, W.H., Janecek, T.R., et al., *Proc. ODP, Init. Repts.*, 130: College Station, TX (Ocean Drilling Program), 497–537.
- Broecker, W.S., and Peng, T.H., 1982. *Tracers in the Sea*: New York (Eldigio Press).
- Cande, S.C., and Kent, D.V., 1995. Revised calibration of the geomagnetic polarity timescale for the late Cretaceous and Cenozoic. *J. Geophys. Res.*, 100:6093–6095.
- Dickens, G.R., O’Neil, J.R., Rea, D.C., and Owen, R.M., 1995. Dissociation of oceanic methane hydrate as a cause of the carbon isotope excursion at the end of the Paleocene. *Paleoceanography*, 10:965–971.
- Farrell, J.W., and Prell, W.L., 1989. Climatic change and CaCO₃ preservation: an 800,000 year bathymetric reconstruction from the central equatorial Pacific ocean. *Paleoceanography*, 4:447–466.
- Gardner, J.V., Nelson, C.S., and Baker, P.A., 1986. Distribution and character of pale green laminae in sediment from Lord Howe Rise: a probable late Neogene and Quaternary tephrostratigraphic record. In Kennett, J.P., von der Borch, C.C., et al., *Init. Repts. DSDP, 90* (Pt. 2): Washington (U.S. Govt. Printing Office), 1145–1159.
- Gieskes, J.M., 1981. Deep-sea drilling interstitial water studies: implications for chemical alteration of the oceanic crust, layers I and II. In Warme, J.E., Douglas, R.G., and Winterer, E.L. (Eds.), *The Deep Sea Drilling Project: A Decade of Progress*. Spec. Publ.—Soc. Econ. Paleontol. Mineral., 32:149–167.
- Kaiho, K., 1998. Phylogeny of deep-sea calcareous trochospiral benthic foraminifera: evolution and diversification. *Micropaleontology*, 44:291–311.
- Kaiho, K., 1999. Evolution in the test size of deep-sea benthic foraminifera during the past 120 million years. *Mar. Micropaleontol.*, 37:53–65.
- Kelly, D.C., Bralower, T.J., Zachos, J.C., Premoli Silva, I., and Thomas, E., 1996. Rapid diversification of planktonic foraminifera in the tropical Pacific (ODP Site 865) during the late Paleocene thermal maximum. *Geology*, 24:423–426.
- Kennett, J.P., von der Borch, C.C., et al., 1986. *Init. Repts. DSDP, 90*: Washington (U.S. Govt. Printing Office).
- Lind, I.L., Janecek, T.R., Krissek, L.A., Prentice, M.L., and Stax, R., 1993. Color bands in Ontong Java Plateau carbonate oozes and chinks. In Berger, W.H., Kroenke, L.W., Mayer, L.A., et al., *Proc. ODP, Sci. Results*, 130: College Station, TX (Ocean Drilling Program), 453–470.
- MacLeod, K.G., and Huber, B.T., 1996. Reorganization of deep ocean circulation accompanying a Late Cretaceous extinction event. *Nature*, 380:422–425.
- MacLeod, K.G., Huber, B.T., and Ward, P.D., 1996. The biostratigraphy and paleobiogeography of Maastrichtian inoceramids. In Ryder, G., Fastowsky, D., and Gartner, S. (Eds.), *The Cretaceous–Tertiary Event and Other Catastrophes in Earth History*. Spec. Publ.—Geol. Soc. Am., 307:361–373.
- Matter, A., Douglas, R.G., and Perch-Nielsen, K., 1975. Fossil preservation, geochemistry and diagenesis of pelagic carbonates from the Shatsky Rise, northwest Pacific. In Larson, R.L., Moberly, R., et al., *Init. Repts. DSDP, 32*: Washington (U.S. Govt. Printing Office), 891–921.

- McNutt, M.K., Winterer, E.L., Sager, W.W., Natland, J.H., and Ito, G., 1990. The Darwin Rise: a Cretaceous superswell? *Geophys. Res. Lett.*, 17:1101–1104.
- Millero, F.J., and Sohn, M.L., 1992. *Chemical Oceanography*: Boca Raton (CRC Press).
- Nakanishi, M., Tamaki, K., and Kobayashi, K., 1989. Mesozoic magnetic anomaly lineations and seafloor spreading history of the northwestern Pacific. *J. Geophys. Res.*, 94:15437–15462.
- Natland, J.H., 1993. Volcanic ash and pumice at Shatsky Rise: sources, mechanisms of transport, and bearing on atmospheric circulation. In Natland, J.H., Storms, M.A., et al., *Proc. ODP, Sci. Results*, 132: College Station, TX (Ocean Drilling Program), 57–66.
- Nyong, E.E., and Olsson, R.K., 1984. A paleoslope model of Campanian to lower Maastrichtian foraminifera in the North American Basin and adjacent continental margin. *Mar. Micropaleontol.*, 8:437–477.
- Okada, H., and Bukry, D., 1980. Supplementary modification and introduction of code numbers to the low-latitude coccolith biostratigraphic zonation (Bukry, 1973; 1975). *Mar. Micropaleontol.*, 5:321–325.
- Pflum, C.E., Frerichs, W.E., and Sliter, W.V., 1976. *Gulf of Mexico Deep-water Foraminifers*. Spec. Publ.—Cushman Found. Foraminiferal Res., 14.
- Rea, D.K., Basov, I.A., Krissek, L.A., and the Leg 145 Scientific Party, 1995. Scientific results of drilling the North Pacific transect. In Rea, D.K., Basov, I.A., Scholl, D.W., and Allan, J.F. (Eds.), *Proc. ODP, Sci. Results*, 145: College Station, TX (Ocean Drilling Program), 577–596.
- Schlanger, S.O., and Douglas, R.G., 1974. The pelagic ooze-chalk-limestone transition and its implication for marine stratigraphy. In Hsü, K.J., and Jenkyns, H.C. (Eds.), *Pelagic Sediments: On Land and Under the Sea*. Spec. Publ.—Int. Assoc. Sedimentol., 1:117–148.
- Sliter, W.V., and Brown, G.R., 1993. Shatsky Rise: seismic stratigraphy and sedimentary record of Pacific paleoceanography since the Early Cretaceous. In Natland, J.H., Storms, M.A., et al., *Proc. ODP, Sci. Results*, 132: College Station, TX, (Ocean Drilling Program), 3–13.
- Tjalsma, R.C., and Lohmann, G.P., 1983. *Paleocene–Eocene Bathyal and Abyssal Benthic Foraminifera from the Atlantic Ocean*. Spec. Publ.—Micropaleontol., 4.
- van Morkhoven, F.P.C.M., Berggren, W.A., and Edwards, A.S., 1986. Cenozoic cosmopolitan deep-water benthic foraminifera. *Bull. Cent. Rech. Explor.—Prod. Elf-Aquitaine*, 11.
- Winterer, E.L., Riedel, W.R., et al., 1971. *Init. Repts. DSDP, 7* (Pt. 1): Washington (U.S. Govt. Printing Office).
- Woodruff, F., 1985. Changes in Miocene deep-sea benthic foraminiferal distribution in the Pacific Ocean: relationship to paleoceanography. In Kennett, J.P. (Ed.), *The Miocene Ocean: Paleoceanography and Biogeography*. Mem.—Geol. Soc. Am., 163:131–175.
- Zachos, J.C., Lohmann, K.C., Walker, J.C.G., and Wise, S.W., Jr., 1993. Abrupt climate change and transient climates during the Paleogene: a marine perspective. *J. Geol.*, 101:191–213.
- Zachos, J.C., Quinn, R.M., and Salamy, K., 1996. High resolution (10⁴ yr) deep-sea foraminiferal stable isotope records of the Eocene-Oligocene climate transition. *Paleoceanography*, 11:251–266.

Figure F1. Interpretation of seismic reflection profile across Site 1210. Mustard = Miocene to Holocene, light brown = Paleogene, medium green = undifferentiated Cretaceous. Major reflections are discussed in the text. For details on the borehole depth to traveltime conversion, see “Depth-Traveltime Conversion,” p. 26, in “Physical Properties” in the “Explanatory Notes” chapter.

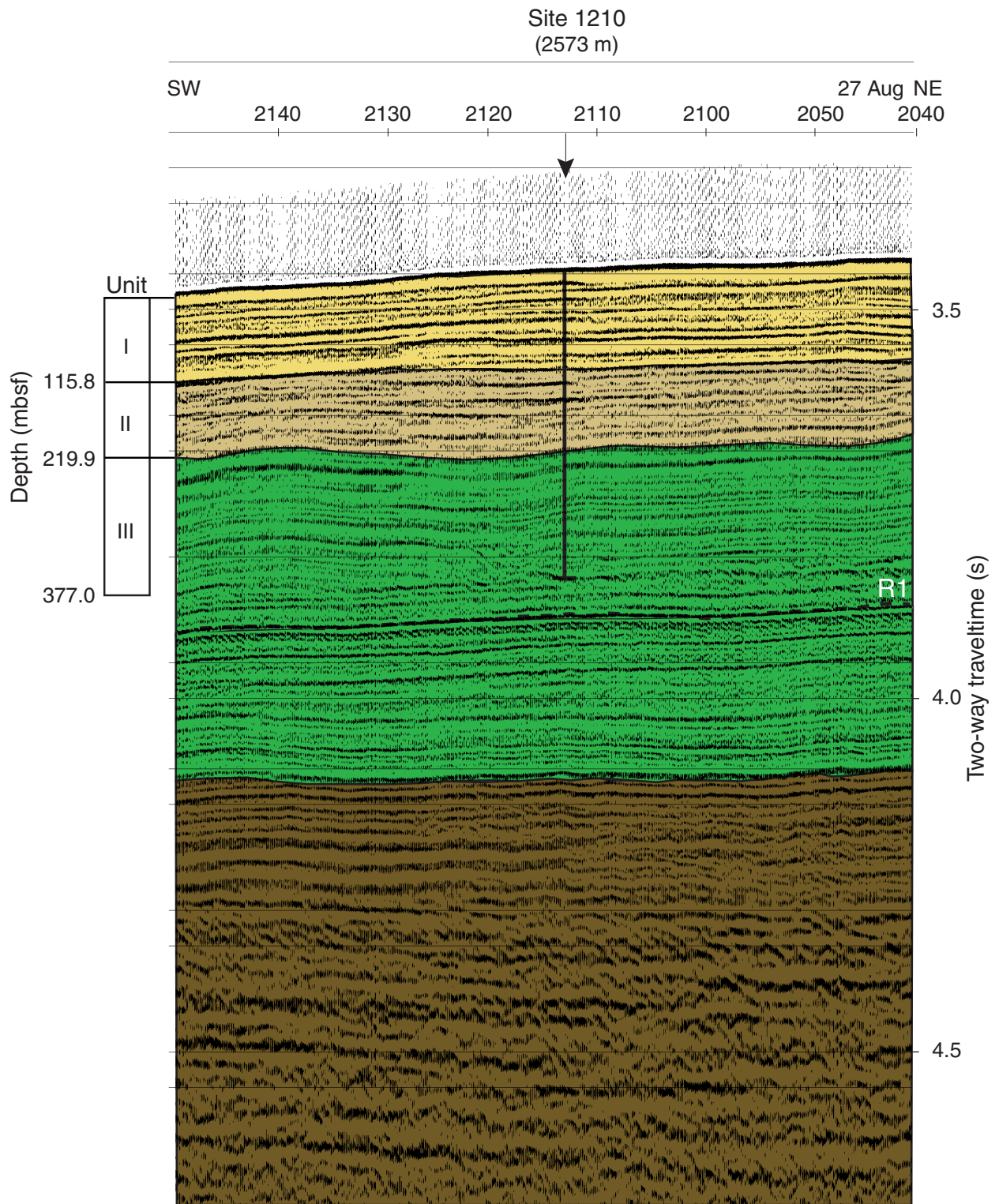


Figure F2. Summary diagram of coring results at Site 1210 plotted on the meters composite depth (mcd) scale. The maximum penetration measured with the drill pipe was 377.0 mbsf. Multisensor track (MST) magnetic susceptibility (brown points) and GRA wet bulk density (dark blue points) were measured every 3.0 cm. The accurate correction factor for the magnetic susceptibility raw instrument values is 0.68×10^{-5} . For details about figure symbols and descriptions see Figure [F12](#), p. 101, in the “Leg 198 Summary” chapter. **(Figure shown on next page.)**

Figure F2 (continued). (Caption shown on previous page.)

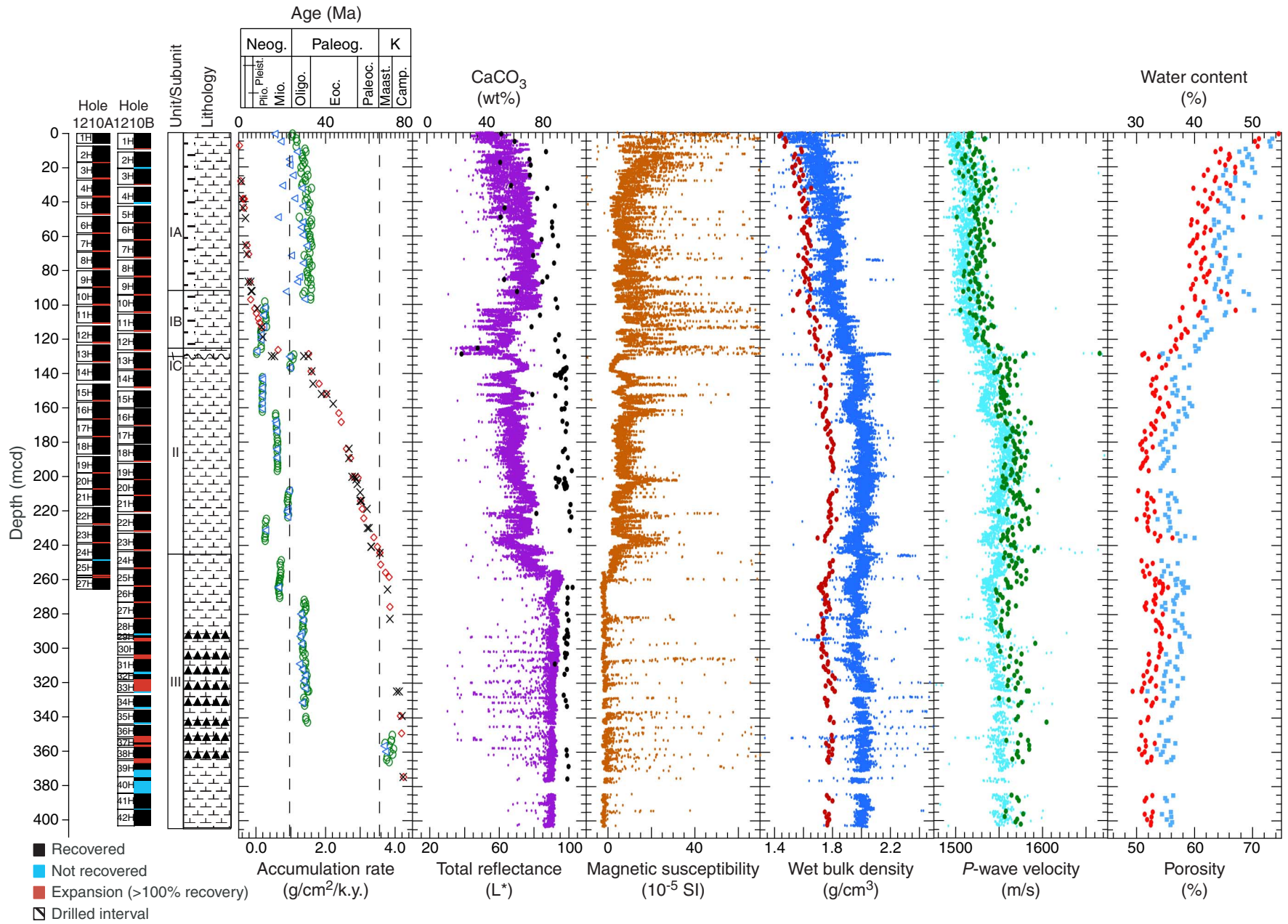


Figure F3. Comparison of magnetic susceptibility records for Holes 1210A (black) and 1210B (blue). The data show the location of critical events (PETM = Paleocene–Eocene thermal maximum, E/O = Eocene/Oligocene boundary, K/T = Cretaceous/Tertiary boundary) as well as significant gaps in the records of individual holes. The accurate correction factor for these raw instrument values is 0.68×10^{-5} .

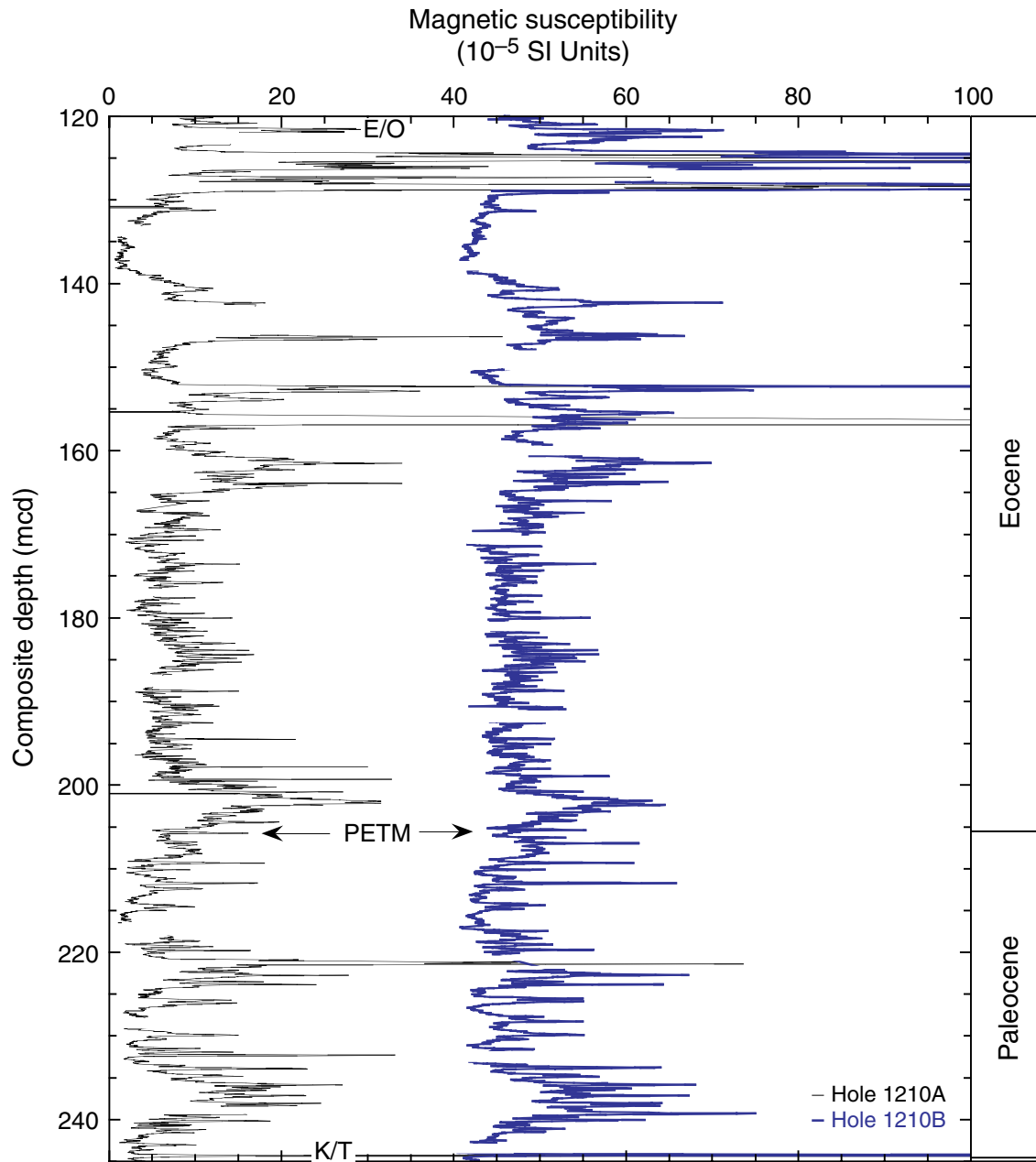


Figure F4. Core recovery, lithology, lithologic units, age with corresponding biostratigraphic zonation, color reflectance, and percent carbonate for Site 1210. Foram. zn. = foraminiferal zone, nanno. zn. = nanofossil zone.

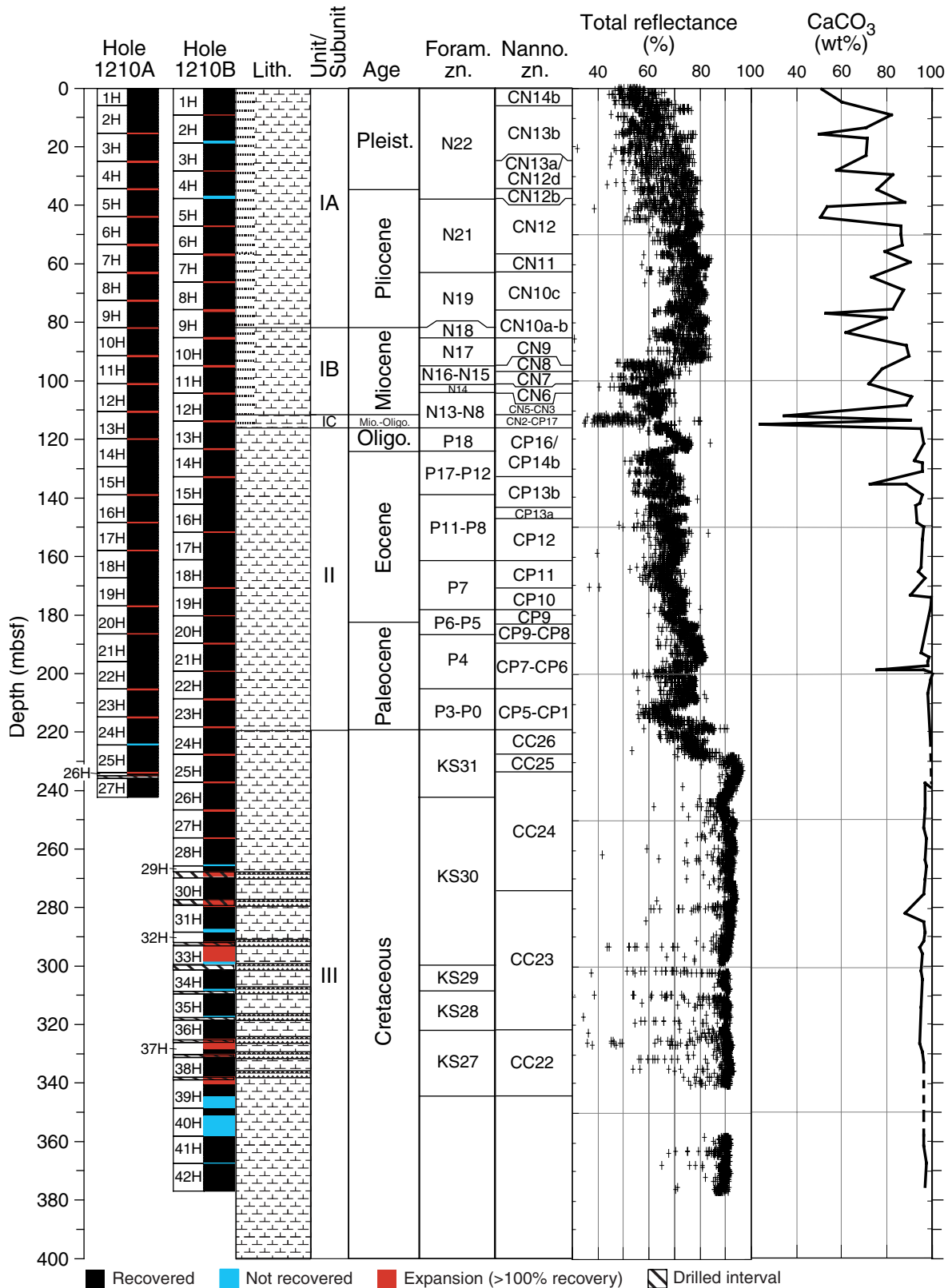


Figure F5. Close-up photograph with arrow pointing to a green lamina crosscutting some burrows (interval 198-1209A-4H-6, 108-129 cm).

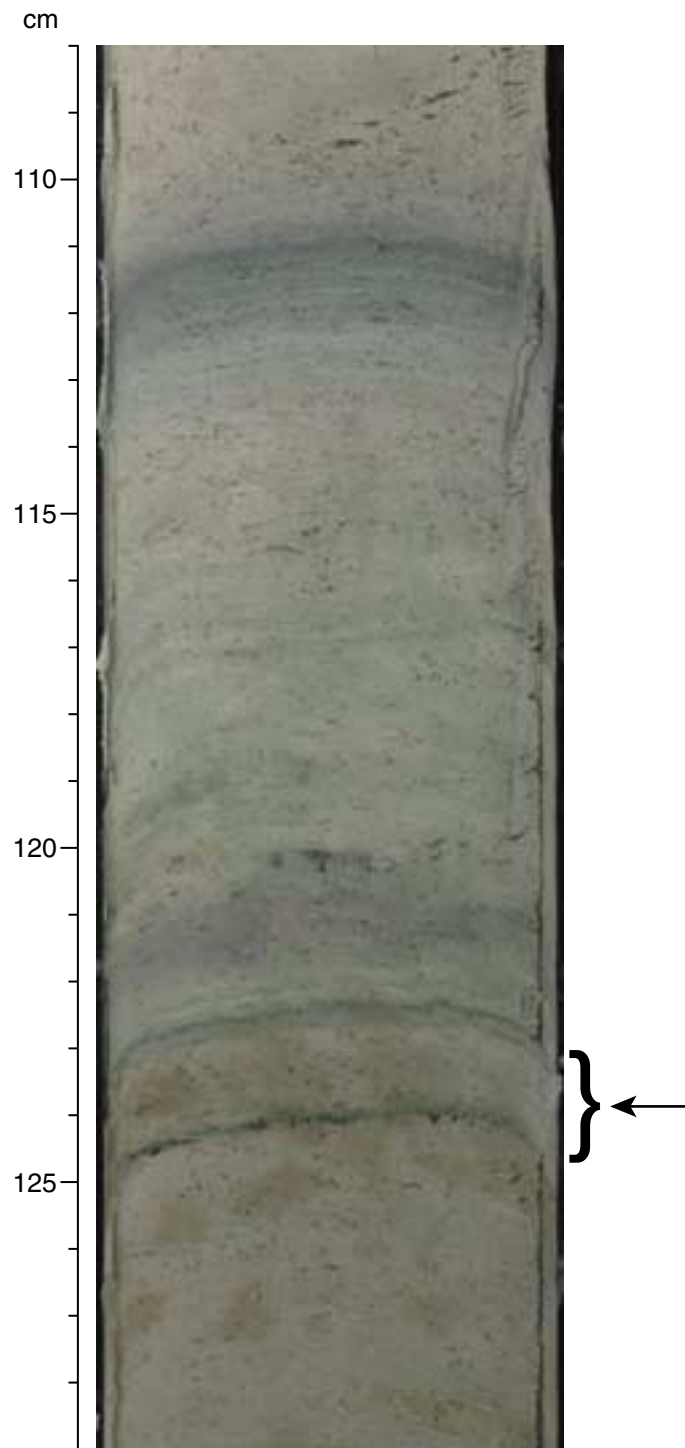


Figure F6. Close-up photograph with arrow pointing to a burrow crosscutting a green lamina (interval 198-1209A-4H-4, 45–53 cm).

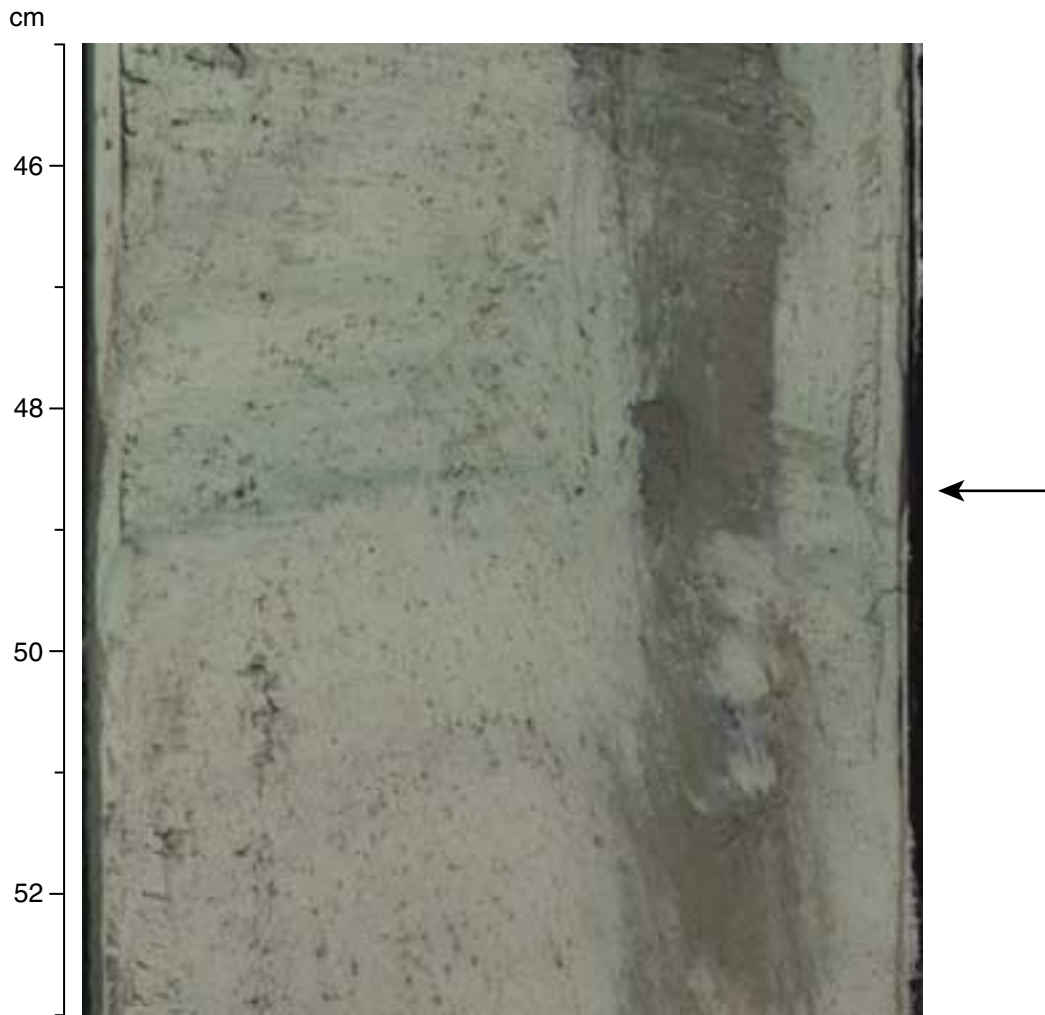


Figure F7. Close-up digital photograph showing a well-defined pale green lamina with diffuse purple banding both above and below (interval 198-1210B-3H-5, 60–90 cm). Locations of X-ray diffraction (XRD) samples from this section are noted (see Table T2, p. 71).

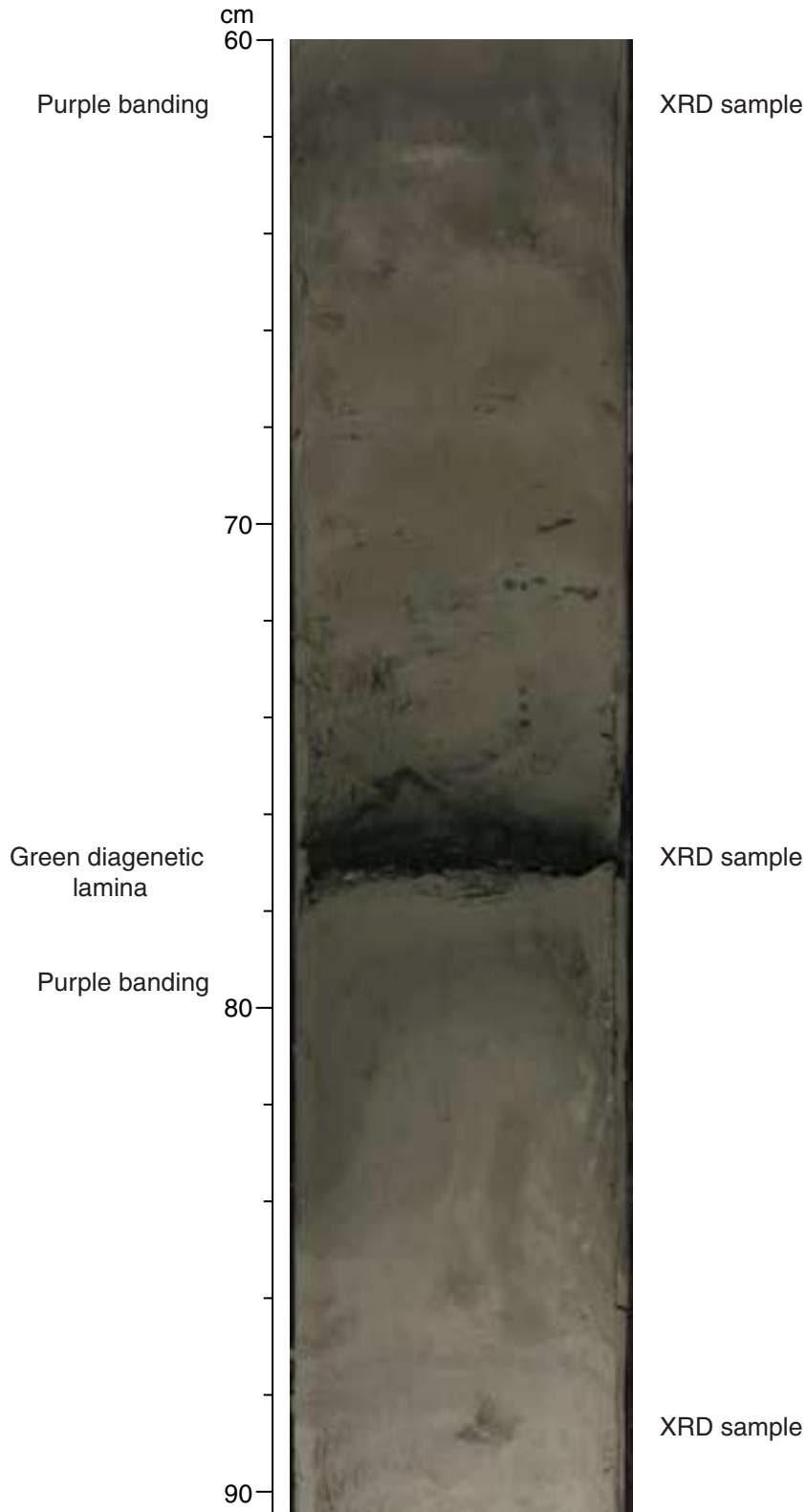


Figure F8. X-ray diffractograms for (A) bulk sediment, Section 198-1210B-6H-1. Curves are shown for three preparation treatments: acid-leached only (red), glycolated (blue), and heated (green). Peaks for clay minerals identified from diffractograms are superimposed on the data. (Continued on next page.)

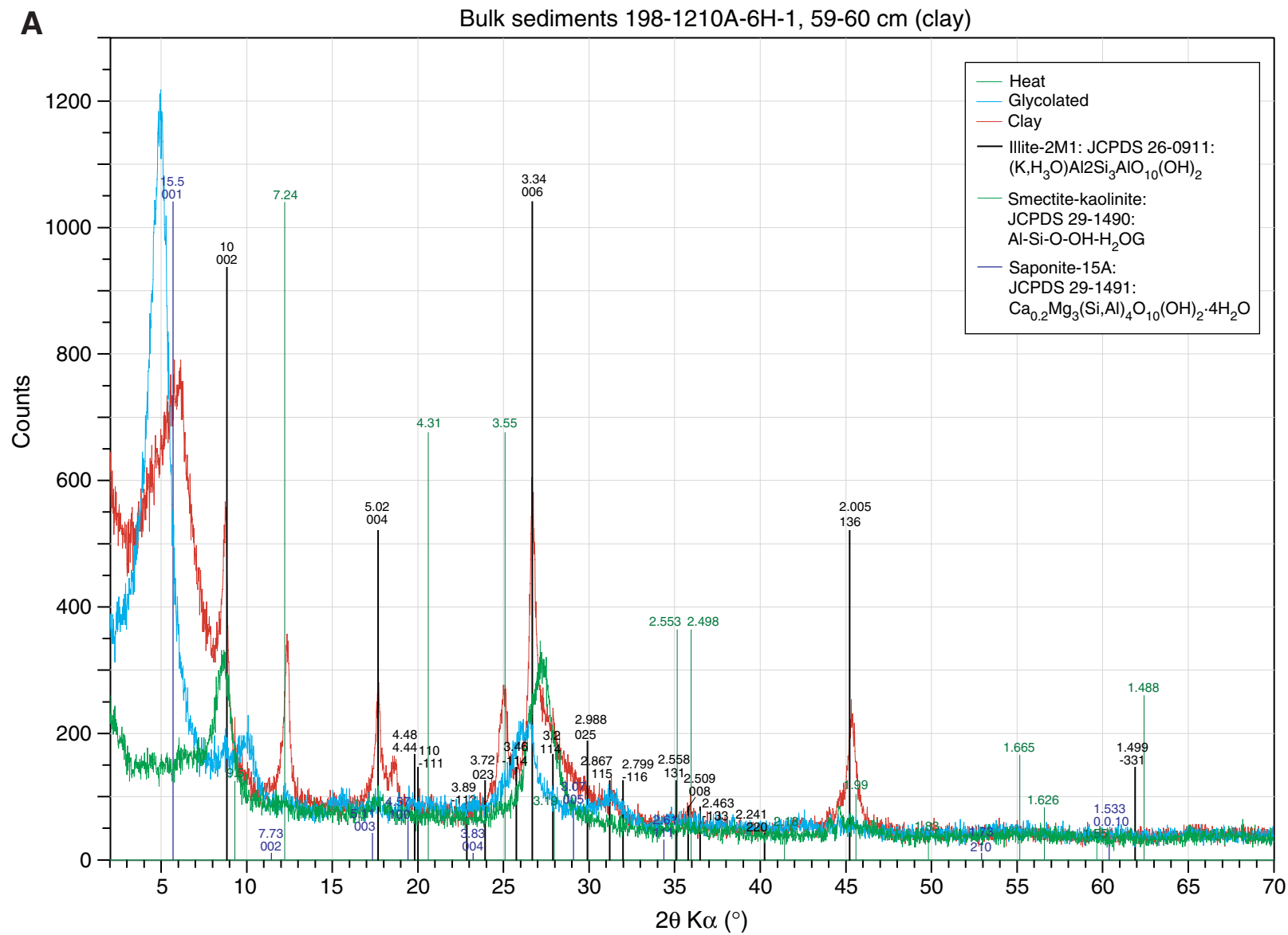


Figure F9. Composite digital photograph, color reflectance, and bulk density for Core 198-1210A-13H. Several dark, clay-rich condensed intervals, which are recorded in the reflectance data, exist in Subunit IC (middle Miocene age).

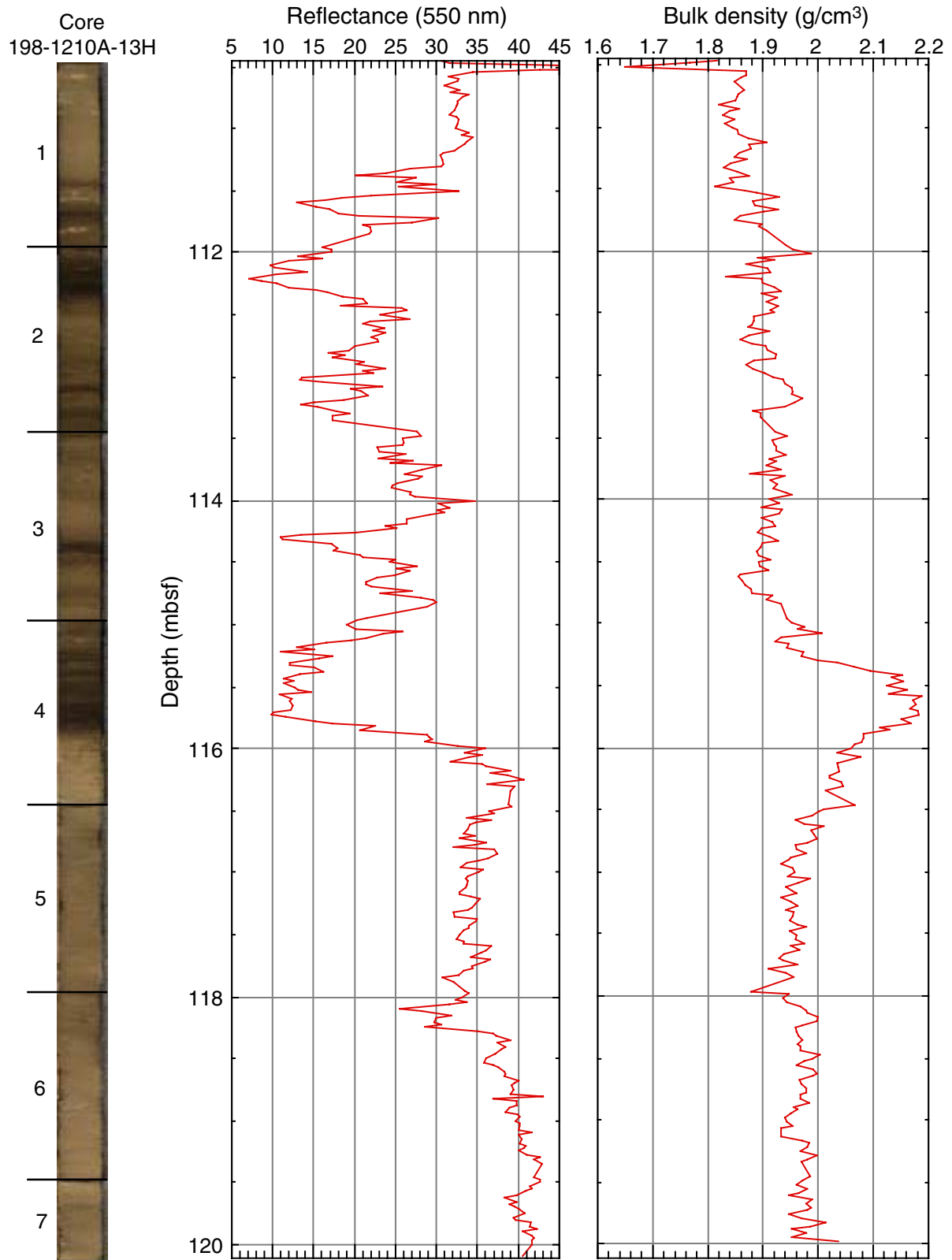


Figure F10. Composite digital photograph, color reflectance, and bulk density for Core 198-1210A-20H. The PETM lies at the base of the negative excursion in reflectance at ~185 mbsf.

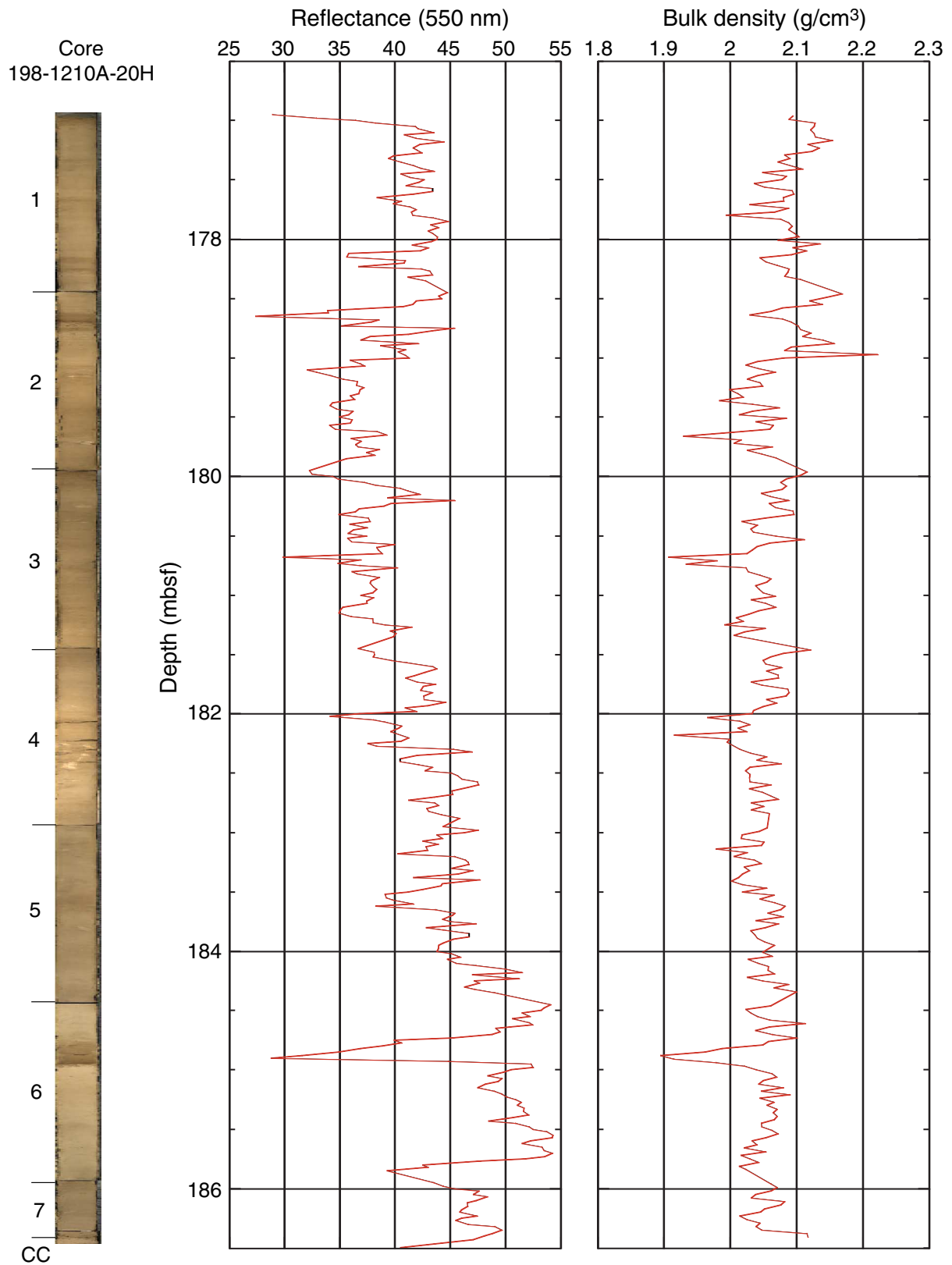


Figure F11. Close-up digital photograph of diffuse green and purple banding (interval 198-1210B-3H-2, 128–145 cm).

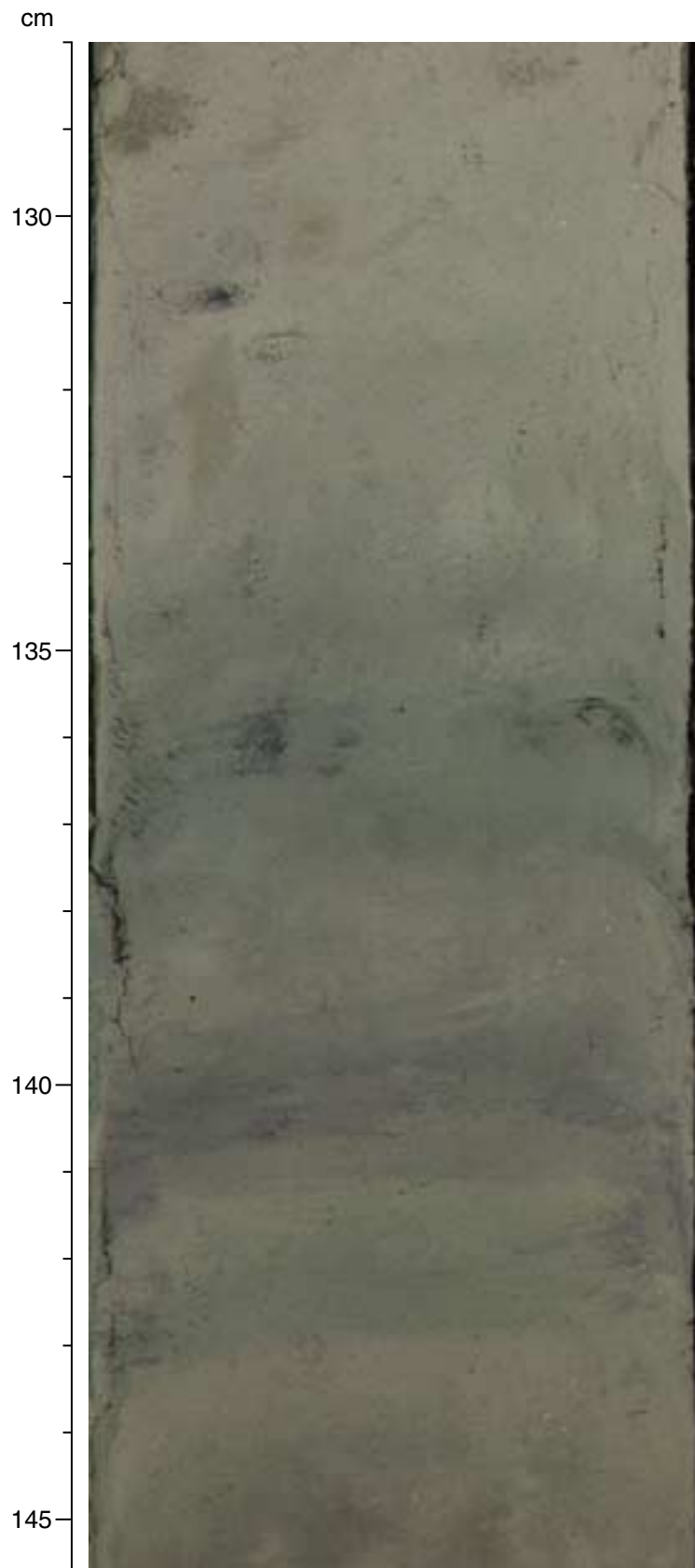


Figure F12. Site 1210 archive-half magnetization intensities after AF demagnetization at peak fields of 20 mT as measured with the shipboard pass-through magnetometer. Solid blue circles = measurements from Hole 1210A, open red circles = measurements from Hole 1210B.

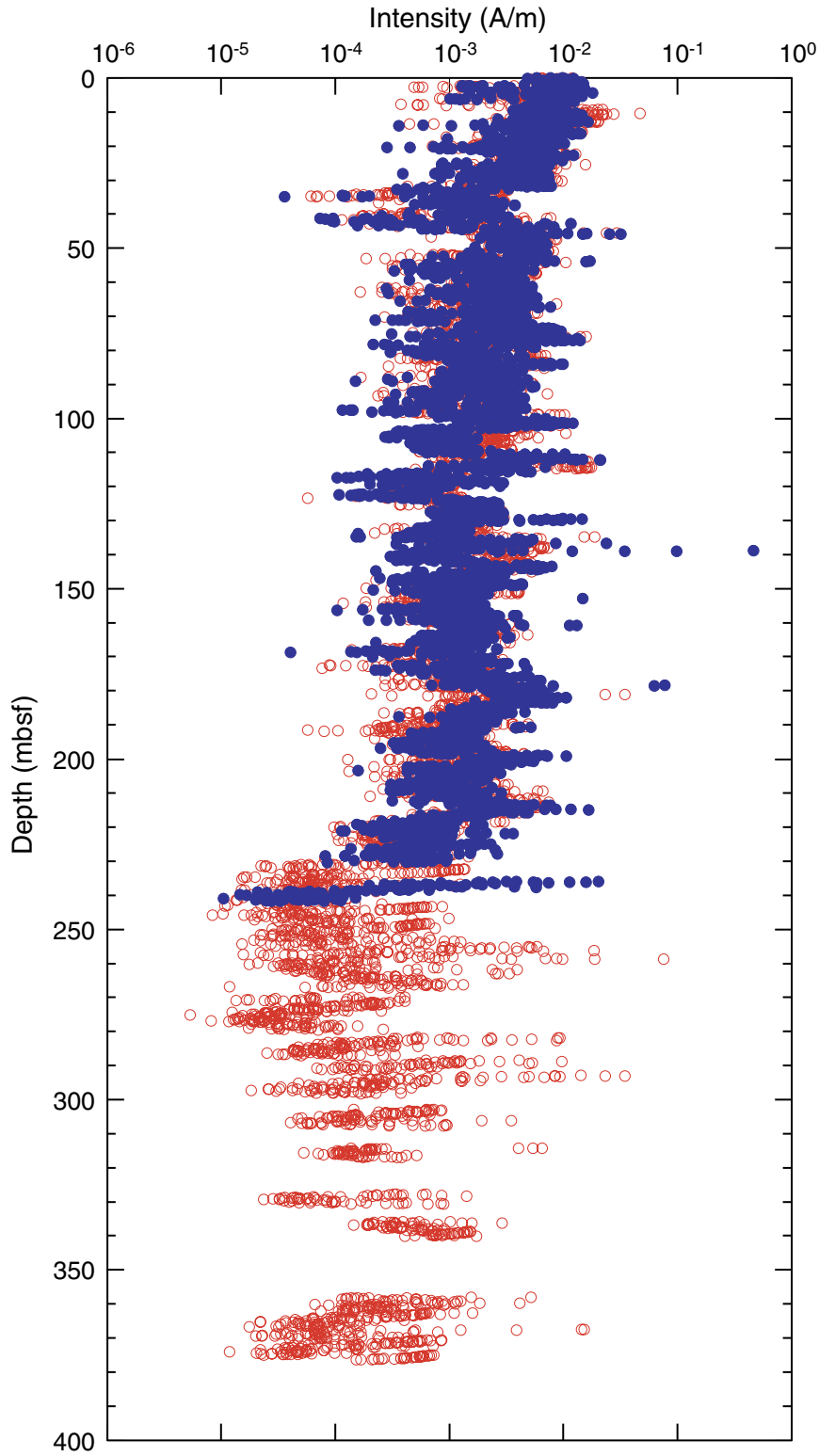


Figure F13. Inclination after AF demagnetization at peak fields of 20 mT as measured with the shipboard pass-through magnetometer for the upper 300 mcd from Holes 1210A (black symbols) and 1210B (purple symbols). The column in the center shows interpreted zones of normal (black) and reversed (white) polarity for the 0–100 mcd interval. Gray intervals indicate zones in which polarity is uncertain.

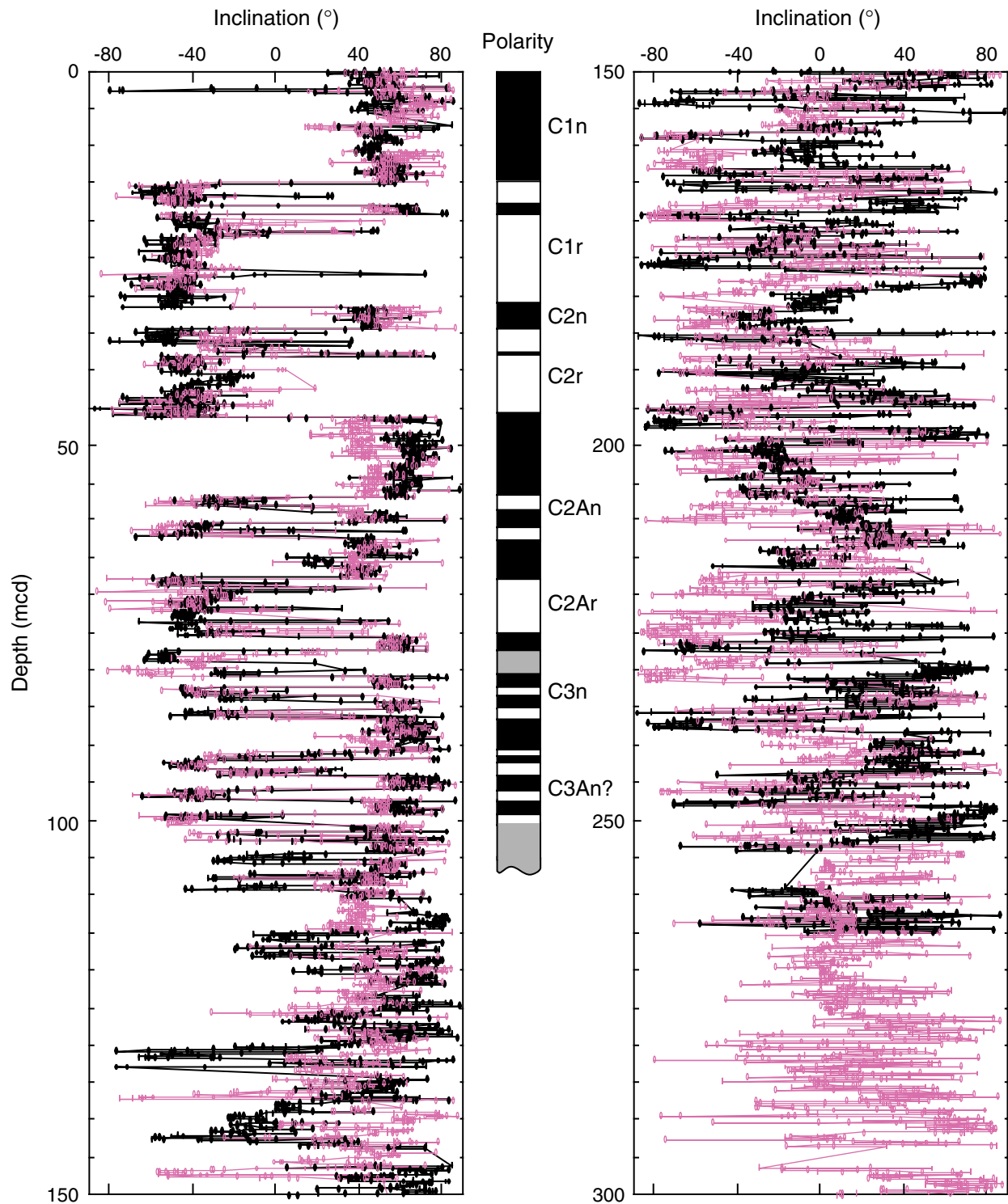


Figure F14. Age-depth curve for Site 1210 derived from the Hole 1210A magnetic stratigraphy shown in Figure F13, p. 46, using the geomagnetic polarity timescale of Cande and Kent (1995). Average sedimentation rates are also plotted.

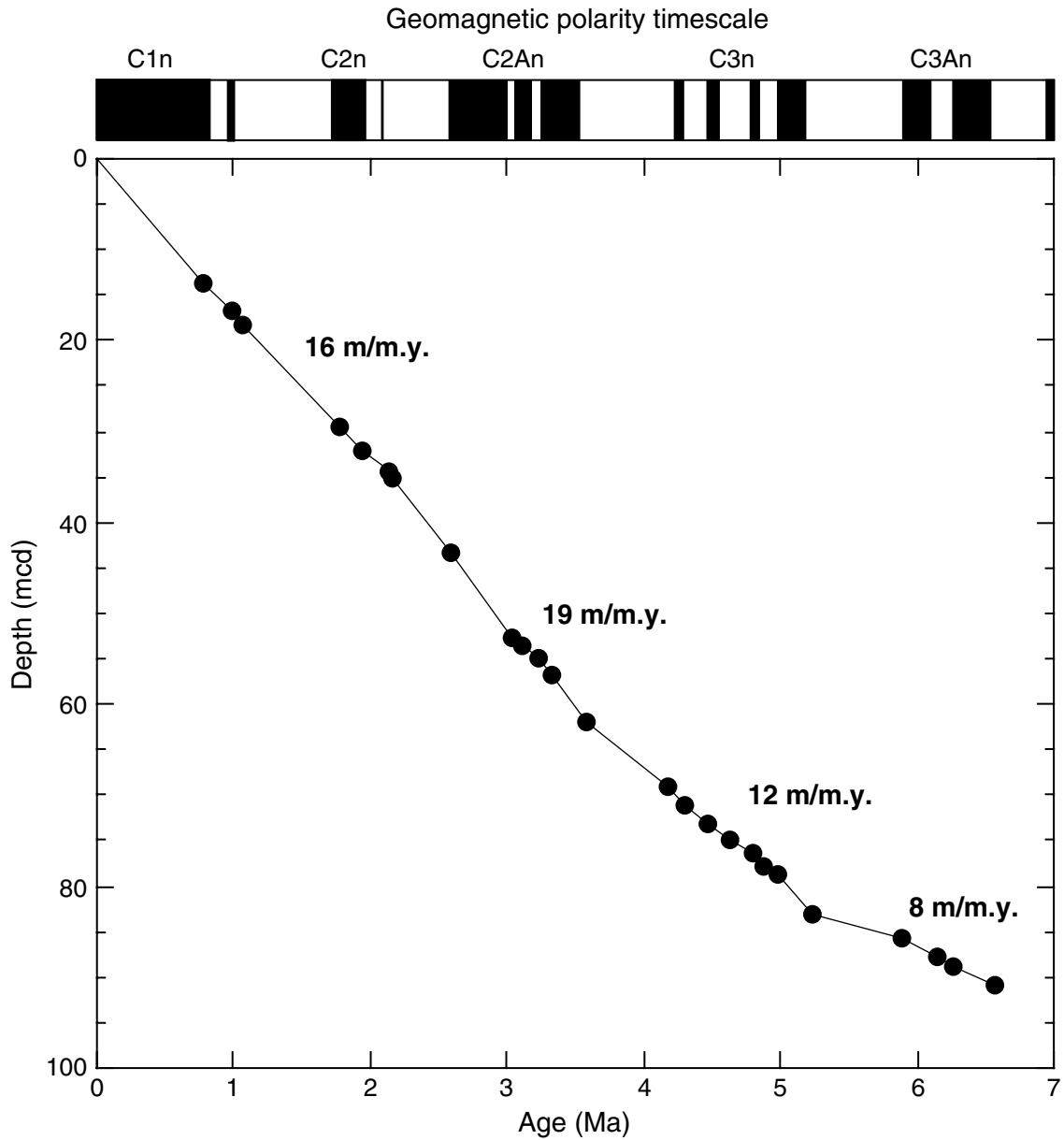


Figure F15. A. Magnetic susceptibility data for 0 to 260 mcd for Site 1210. The accurate correction factor for these raw instrument values is 0.68×10^{-6} . Hole 1210B data are offset from Hole 1210A data by a constant (40×10^{-6}). B. Gamma ray attenuation (GRA) bulk density data for 0 to 260 mcd for Site 1210. Hole 1210B data are offset from Hole 1210A data by a constant (0.3 g/cm^3).

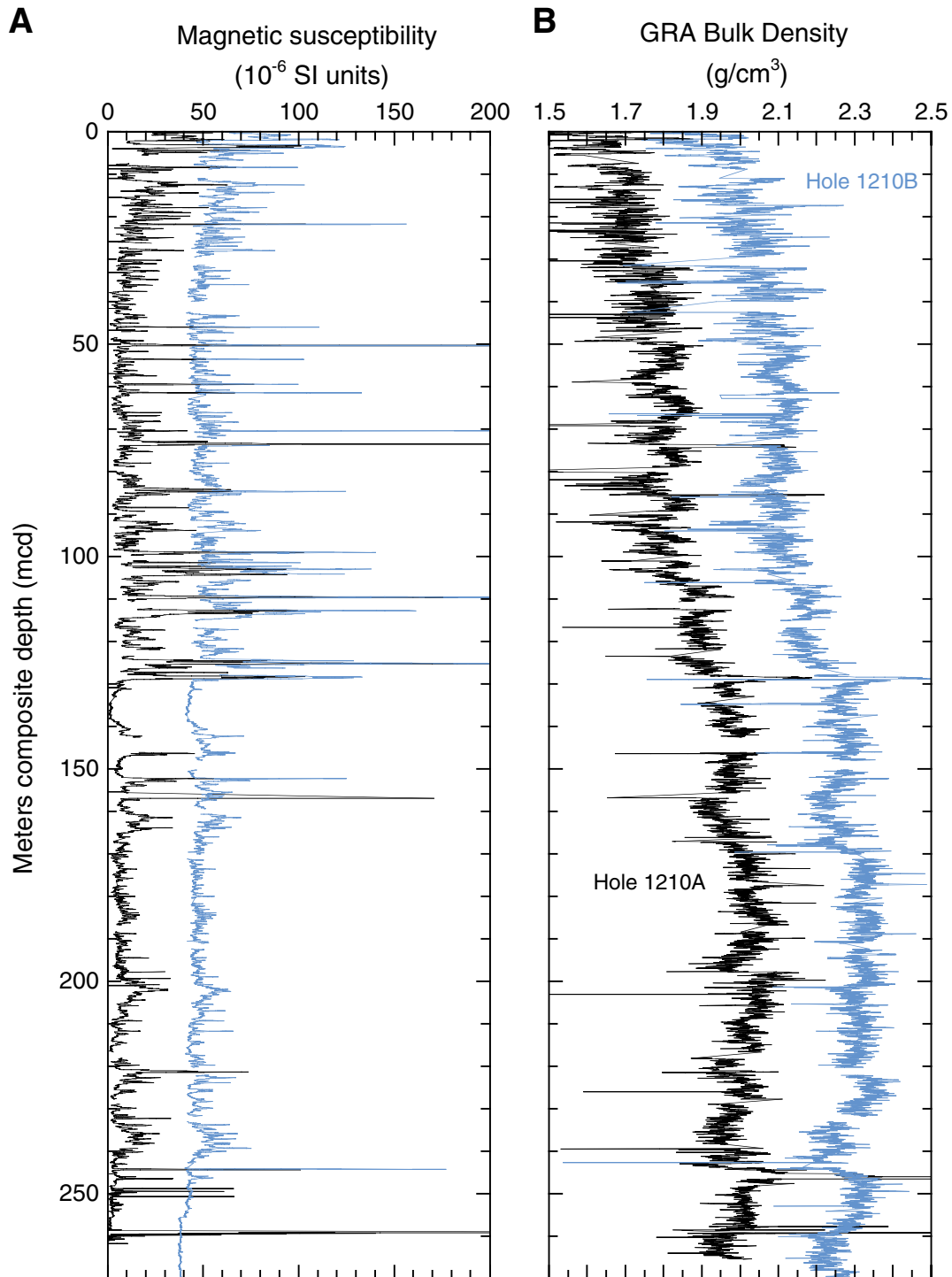


Figure F16. Magnetic susceptibility data for 115 to 135 mcd for Holes 1210A (black line) and 1210B (blue line). The accurate correction factor for these raw instrument values is 0.68×10^{-6} . This interval includes the middle Miocene/lower Oligocene unconformity. Hole 1210B data are offset from Hole 1210A data by a constant (40×10^{-6}).

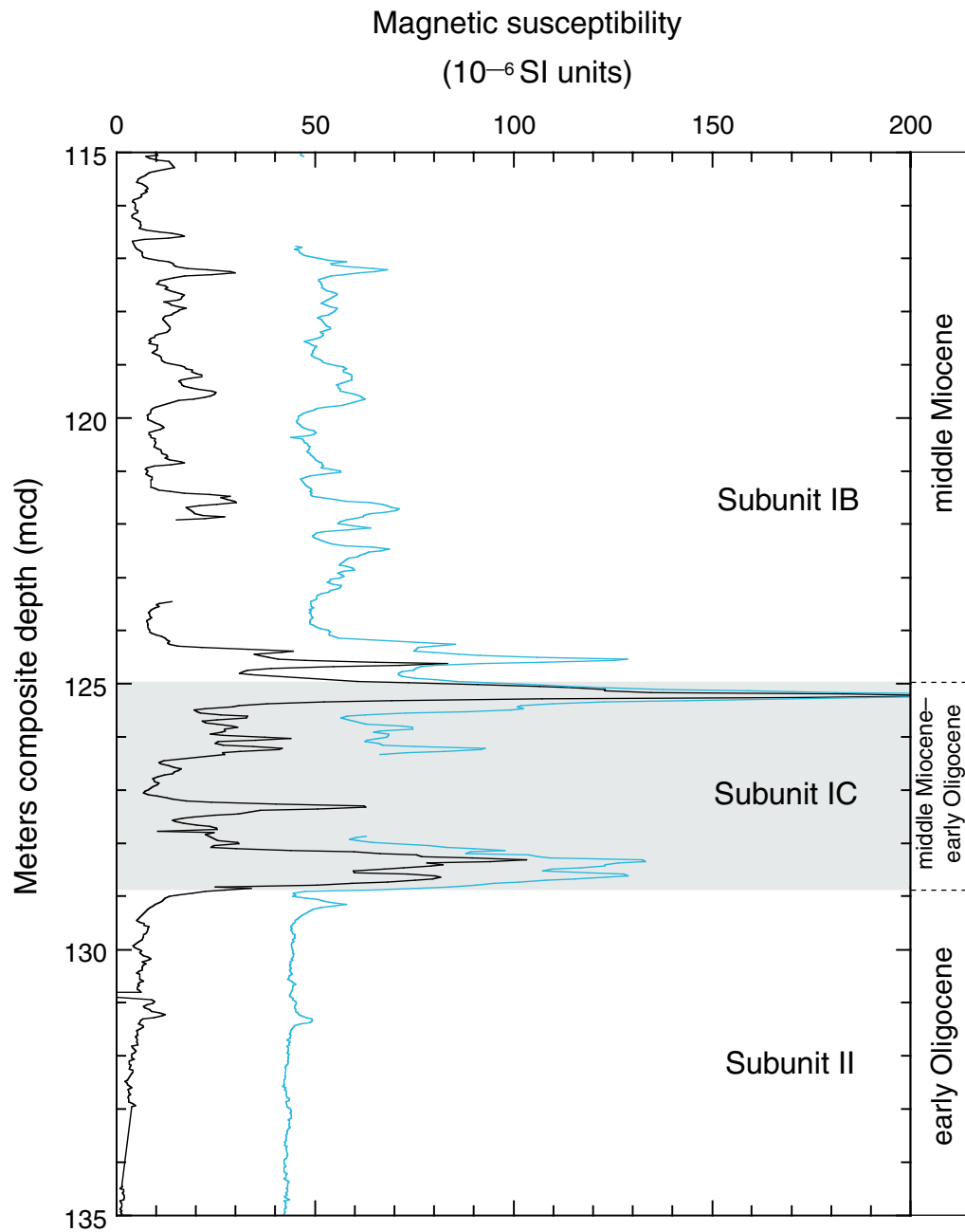


Figure F17. Age-depth plot of calcareous nannofossil (diamonds) and planktonic foraminiferal (crosses) datums at Site 1210. Datum ages and depths are presented in Tables T3, p. 72, and T4, p. 73.

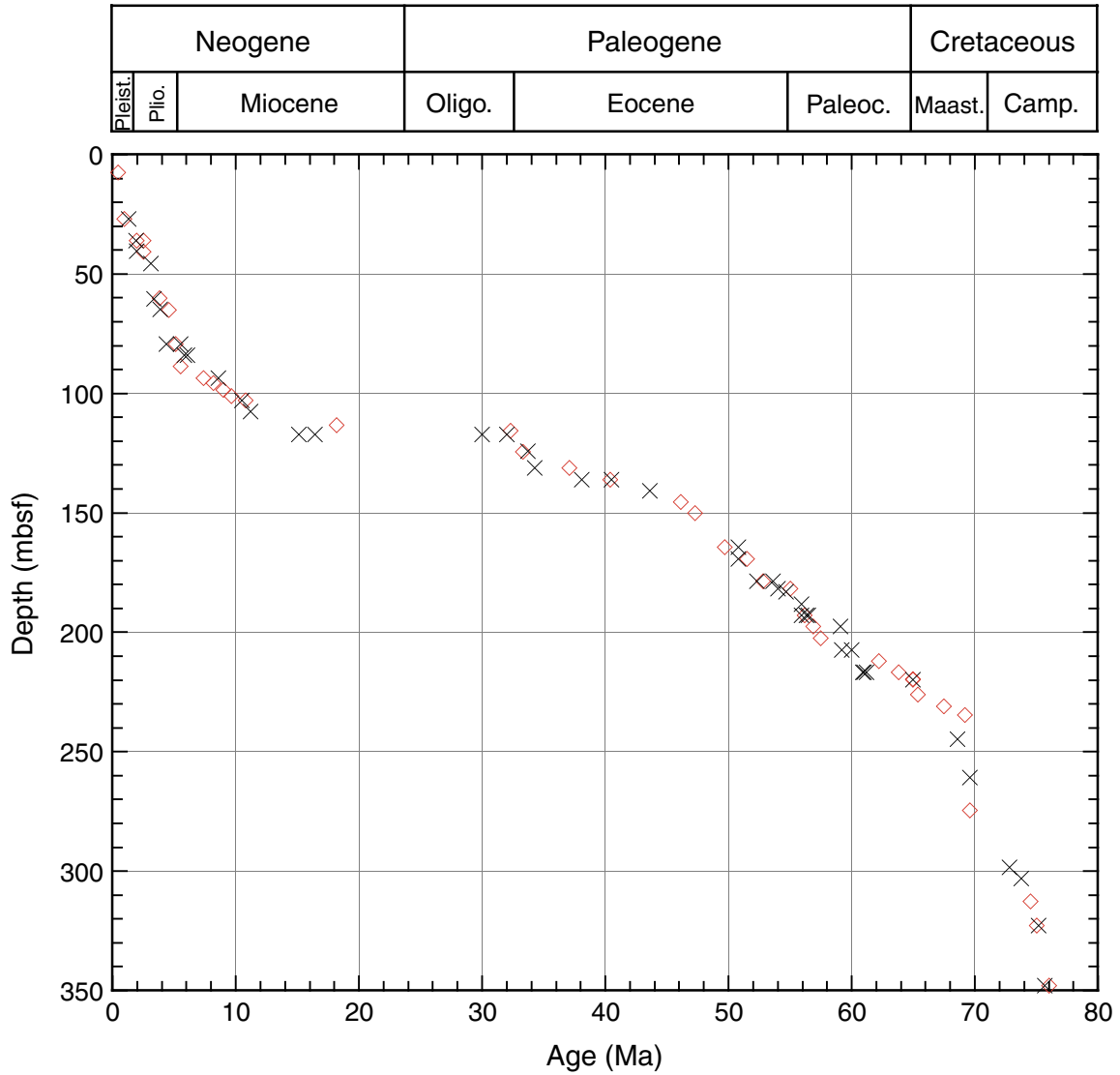


Figure F18. Age-depth plot of Neogene calcareous nannofossil (diamonds) and planktonic foraminiferal (crosses) datums at Site 1210. The pair of lines through the upper Miocene and uppermost Miocene–Pleistocene show alternate interpretations of sedimentation rate changes. Foraminiferal data based on core catcher samples suggest the presence of an unconformity separating the middle Miocene and lower Oligocene, whereas calcareous nannofossil data indicate the presence of one or more condensed intervals. Datum ages and depths are presented in Tables T3, p. 72, and T4, p. 73. FO = first occurrence, LO = last occurrence.

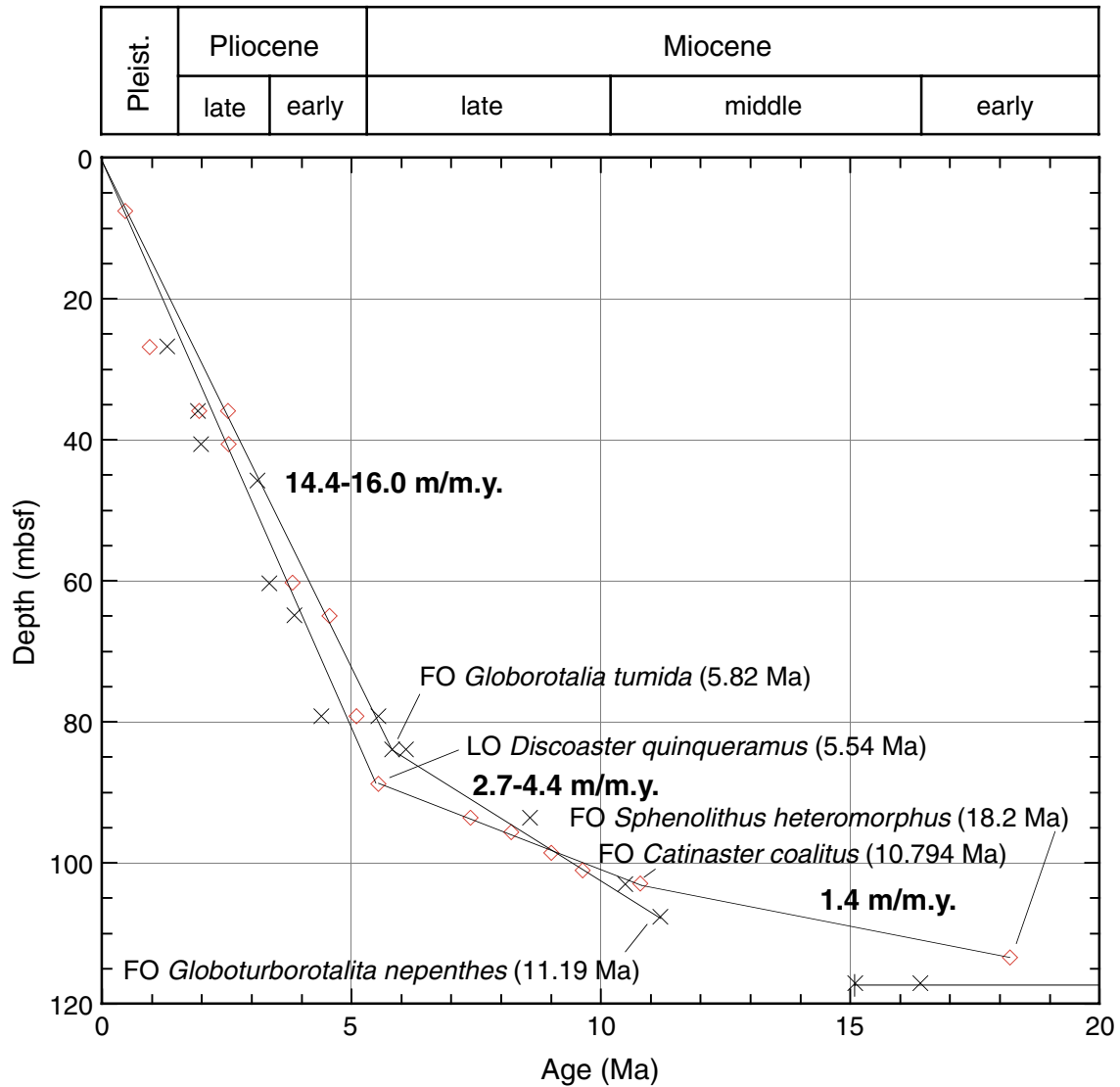


Figure F19. Age-depth plot of early Miocene–late Eocene calcareous nannofossil (diamonds) and planktonic foraminiferal (crosses) datums at Site 1210. Foraminiferal data based on core catcher samples suggest the presence of an unconformity separating the middle Miocene and lower Oligocene, whereas calcareous nannofossil data indicate the presence of one or more condensed intervals. Datum ages and depths are presented in Tables T3, p. 72, and T4, p. 73. FO = first occurrence, LO = last occurrence, TA = top acme.

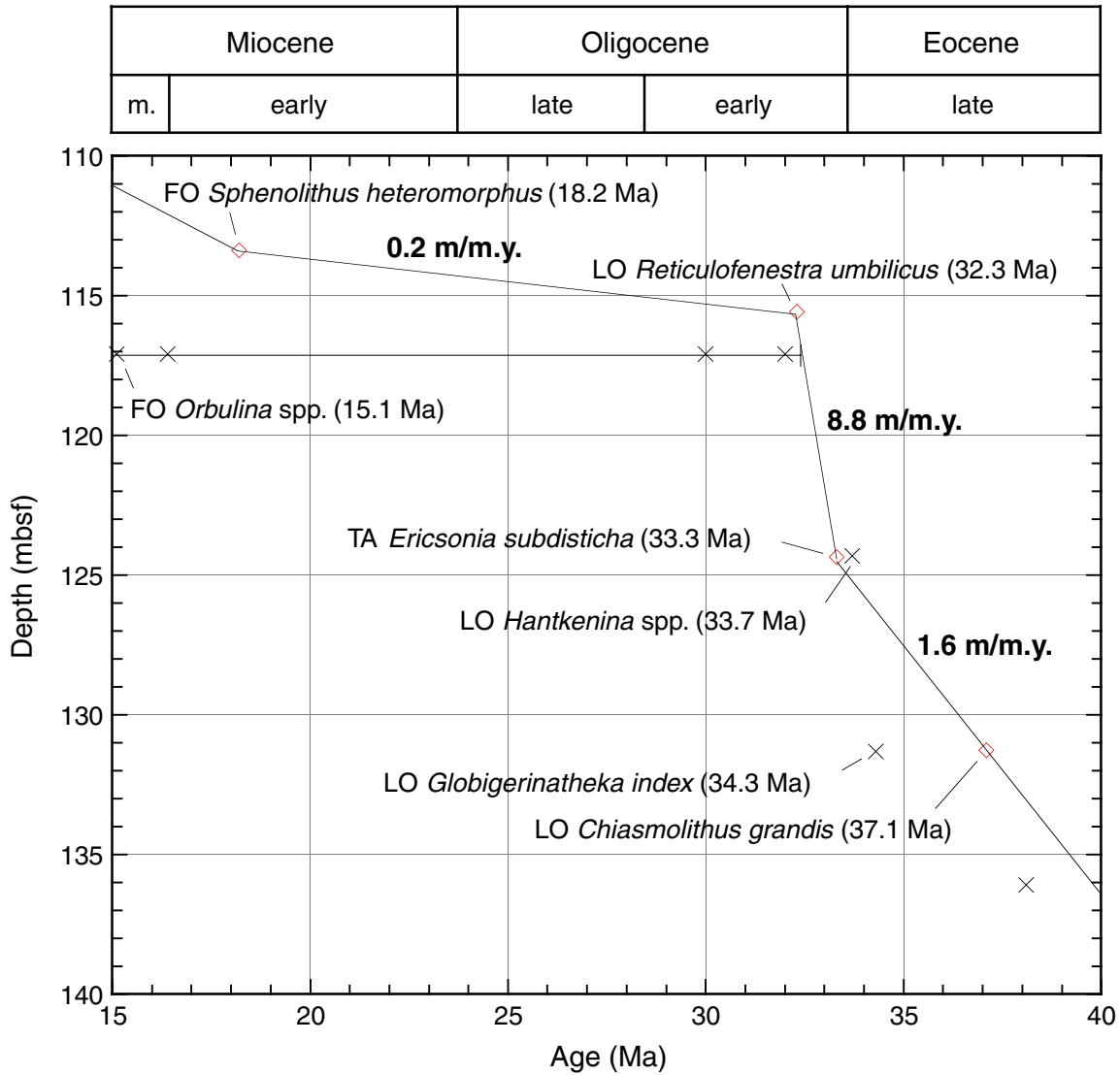


Figure F20. Age-depth plot of early Oligocene–late Paleocene calcareous nannofossil (diamonds) and planktonic foraminiferal (crosses) datums at Site 1210. Datum ages and depths are presented in Tables T3, p. 72, and T4, p. 73. FO = first occurrence, LO = last occurrence, TA = top acme.

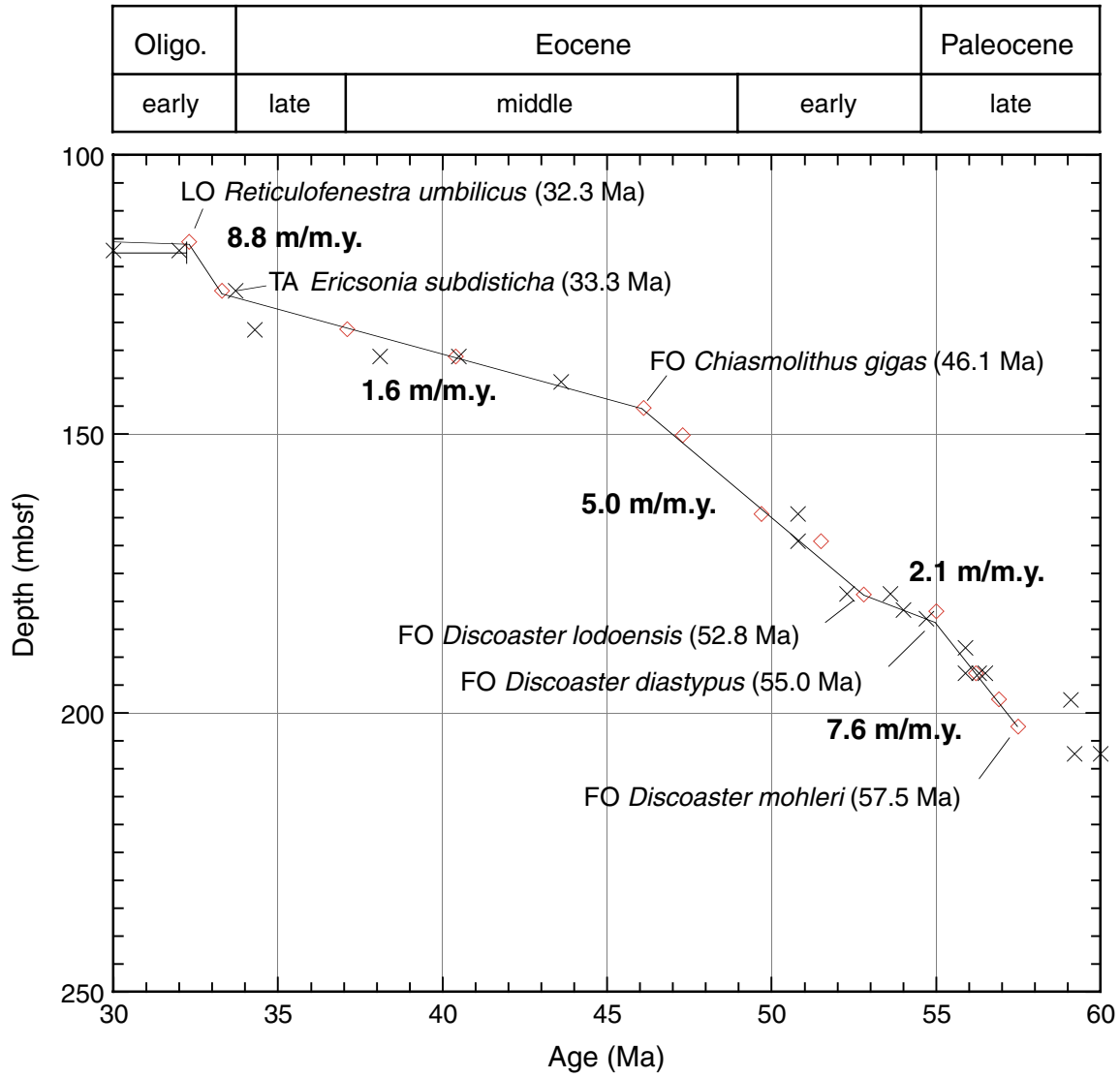


Figure F21. Age-depth plot of early Eocene–Campanian calcareous nannofossil (diamonds) and planktonic foraminiferal (crosses) datums at Site 1210. Datum ages and depths are presented in Tables T3, p. 72, and T4, p. 73. FO = first occurrence, LO = last occurrence.

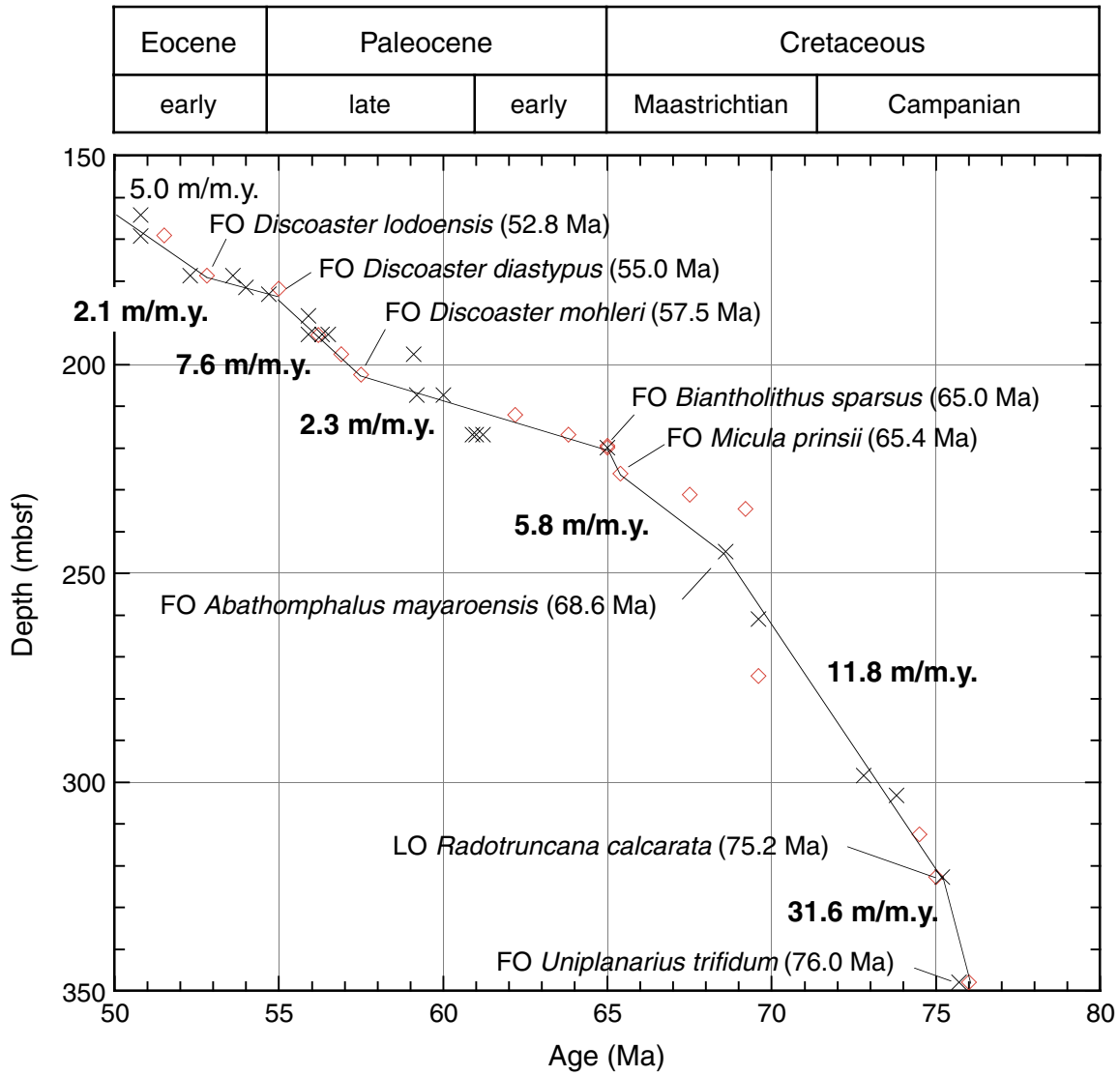


Figure F22. Mass accumulation rates for bulk sediment, carbonate fraction, and noncarbonate fraction vs. (A) depth and (B) age for the Campanian–Pleistocene of Site 1210.

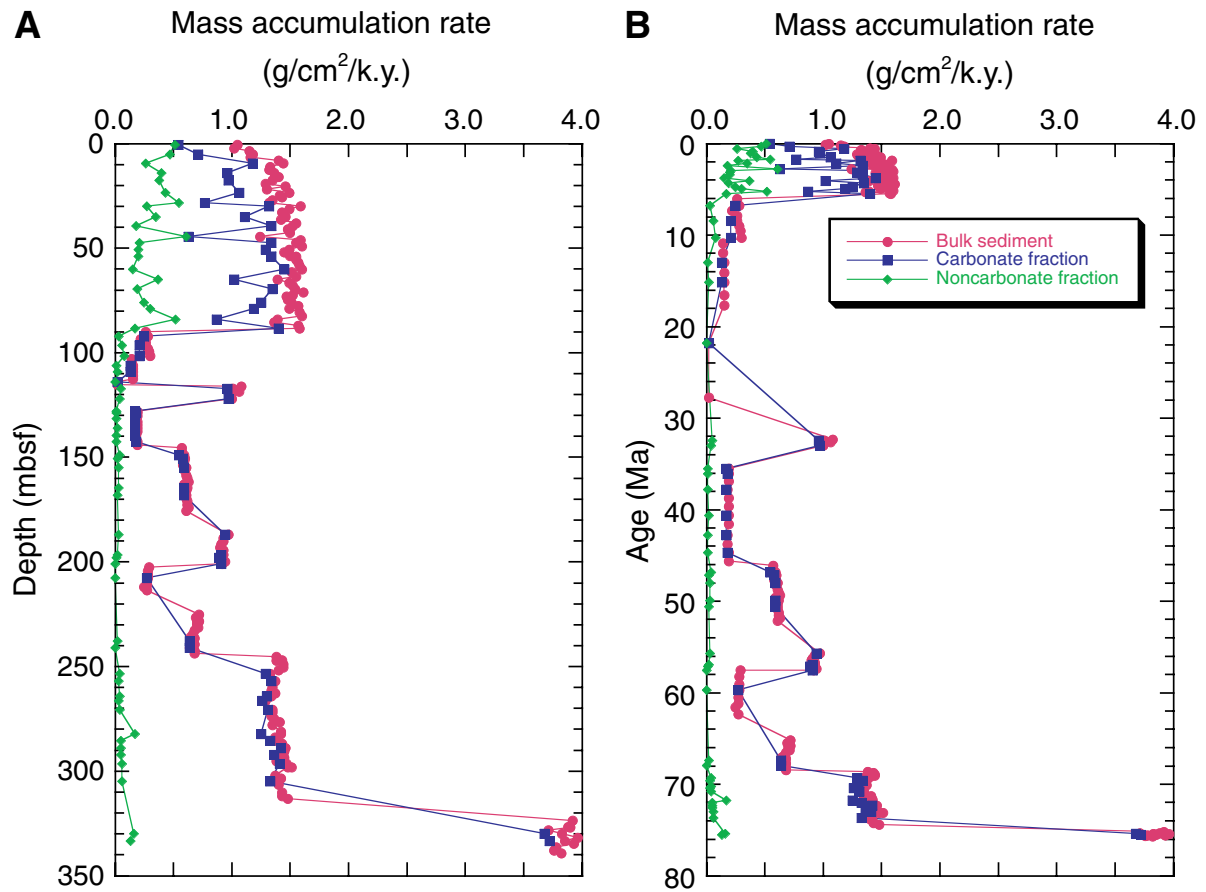


Figure F23. Downhole profiles of carbonate content at Site 1210.

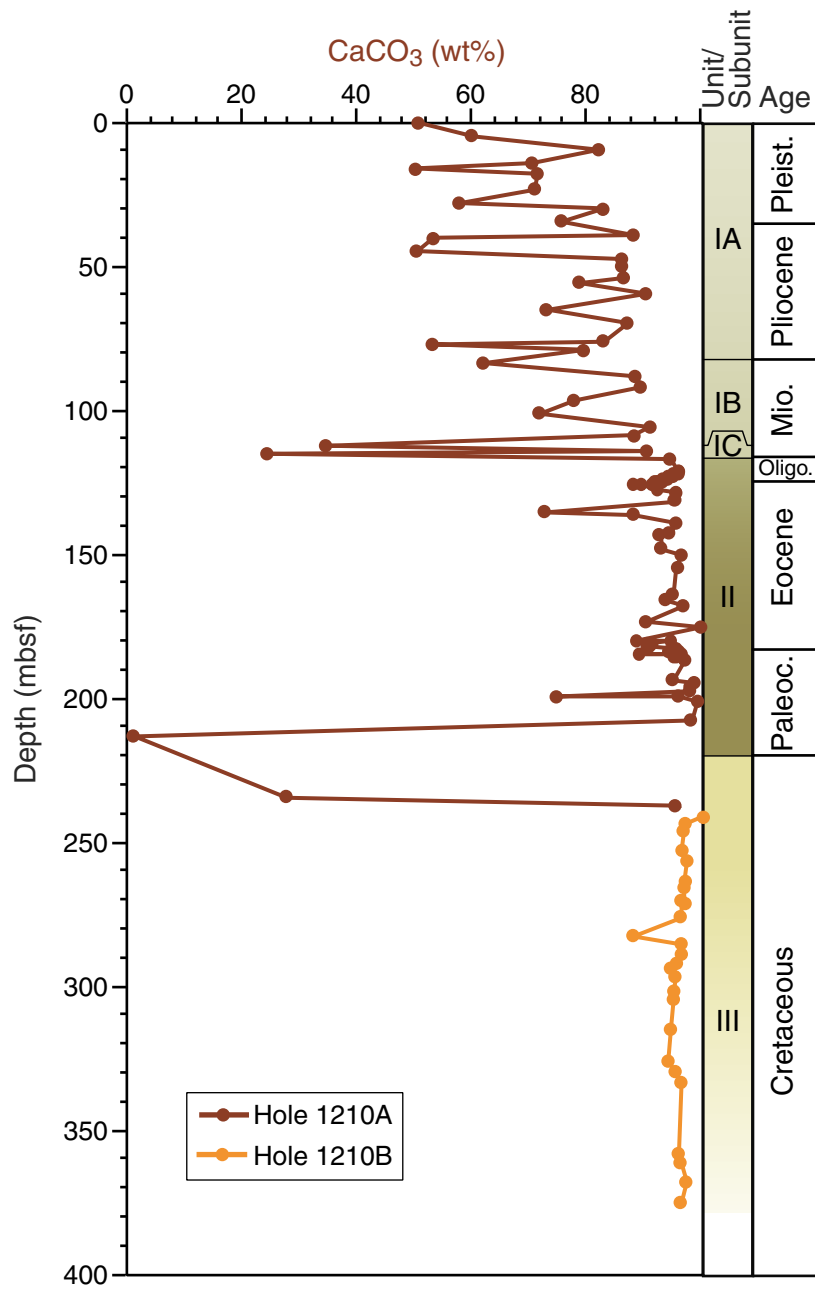


Figure F24. Chloride ion concentrations at Site 1210. Variability in the downcore chloride profile is shown at Site 1210 (left) and at a higher resolution in the 0–100 mbsf interval (right).

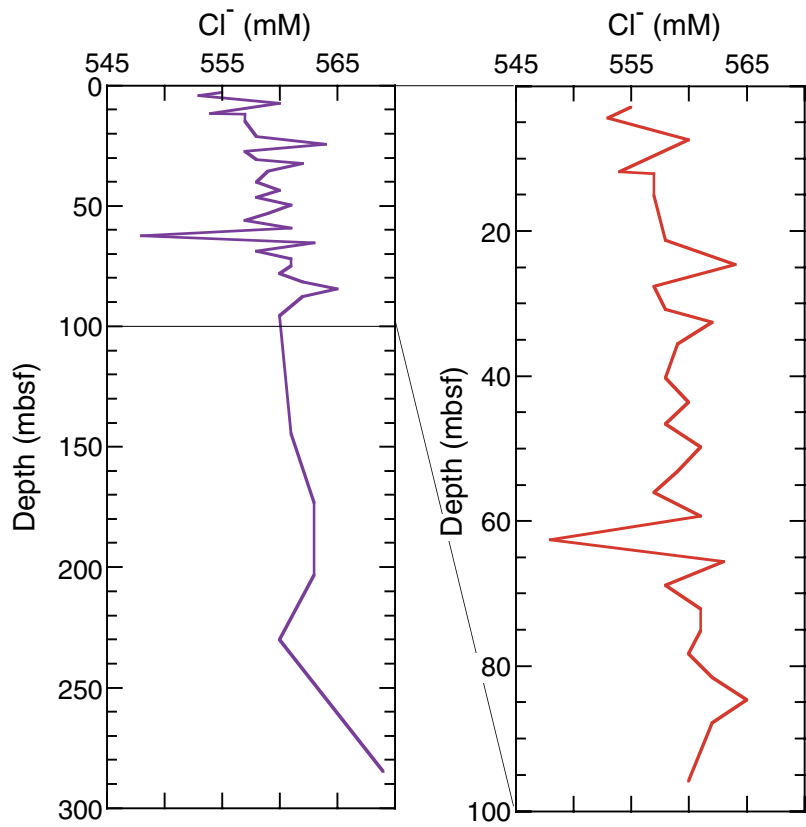


Figure F25. Site 1210 interstitial water profiles. **A.** Alkalinity. **B.** Sulfate. **C.** Ammonium. **D.** Phosphate. **E.** Iron. **F.** Manganese. These figures represent organic remineralization reactions. Deviations in the iron profile are likely related to the occurrence of pyrite blebs and oxidized sediments.

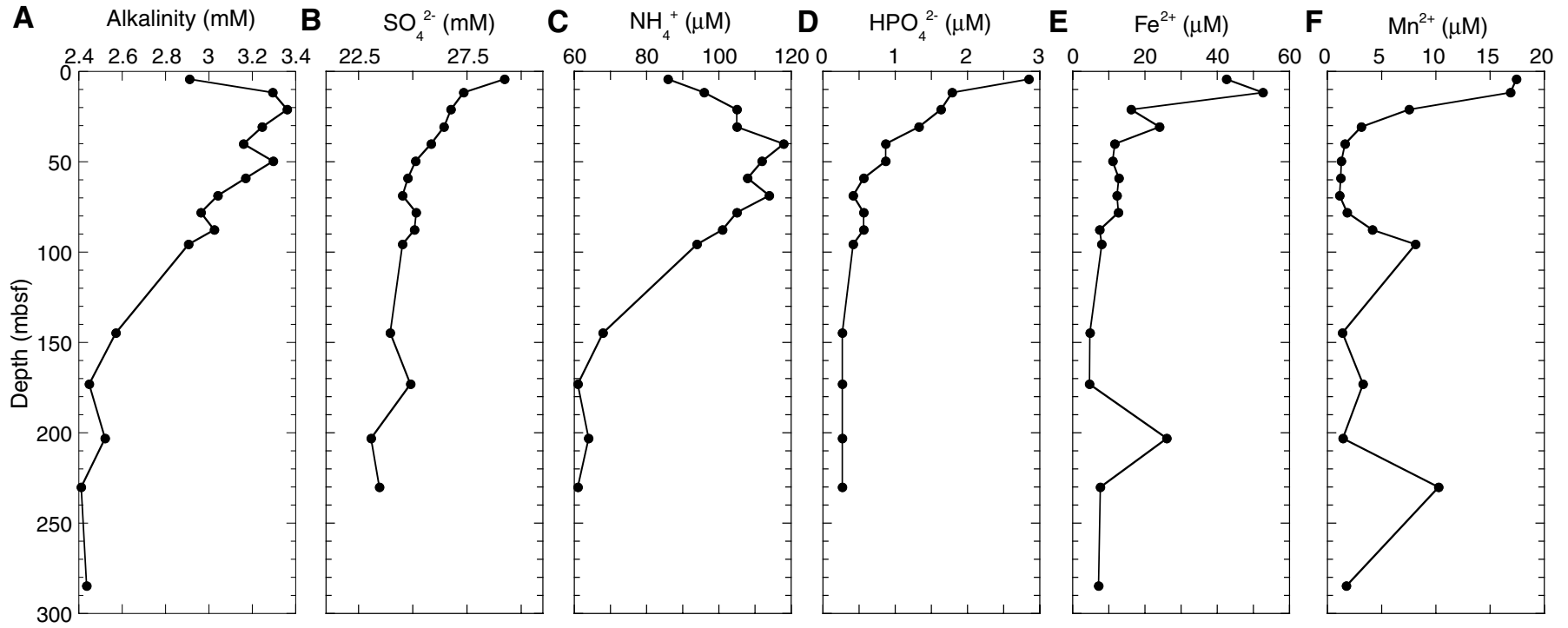


Figure F26. Interstitial water profiles for Site 1210. A. Potassium. B. Calcium. C. Magnesium. D. Sr and Sr/Ca. E. Lithium. These profiles do not differ significantly from Sites 1208 and 1209.

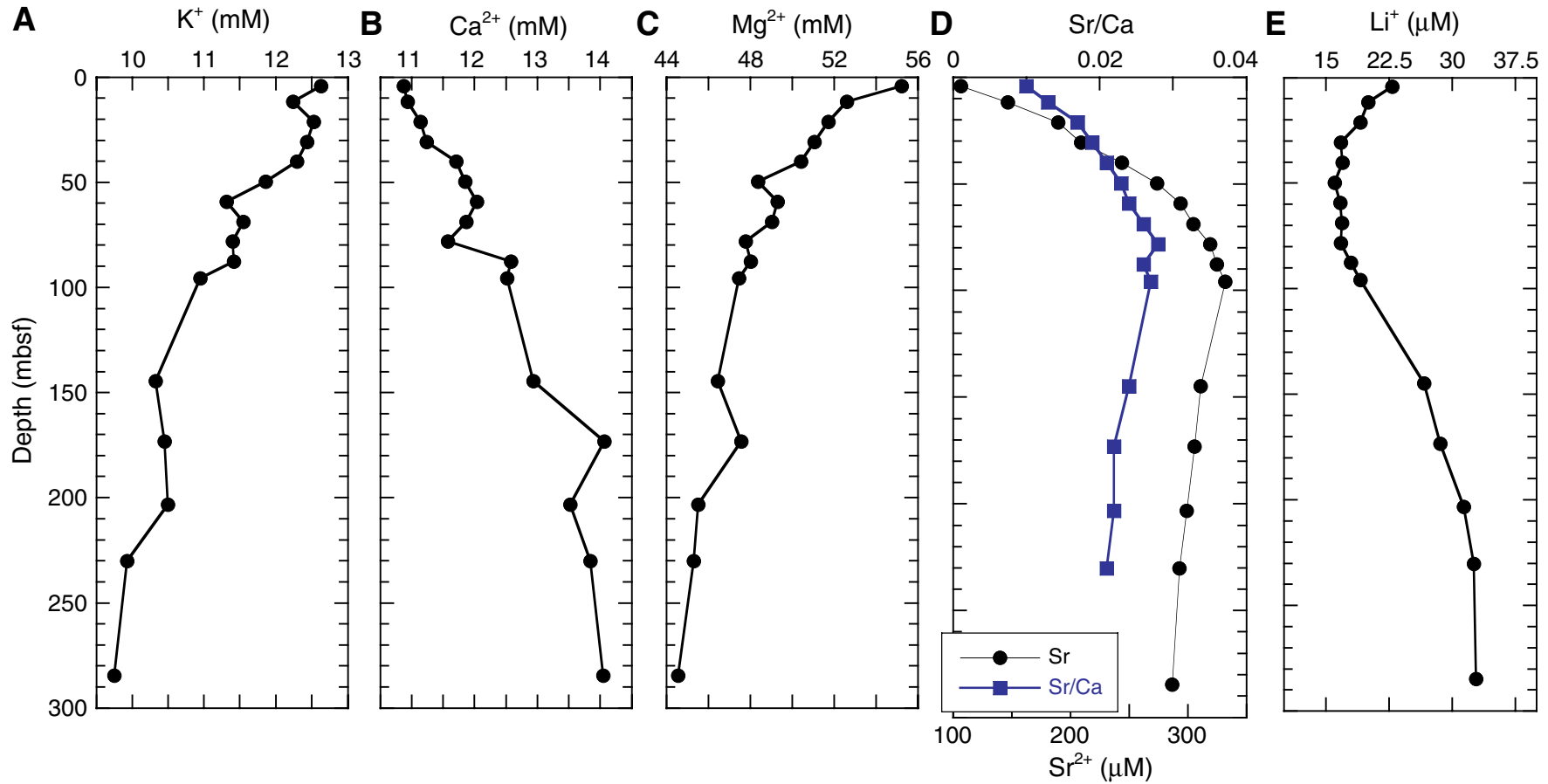


Figure F27. Silica profile for Site 1210.

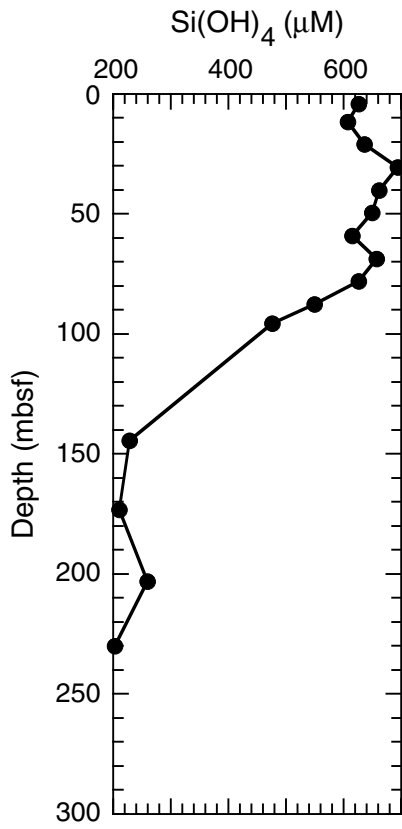


Figure F28. MST magnetic susceptibility measured in whole cores from Holes 1210A and 1210B plotted vs. depth. The accurate correction factor for these raw instrument values is 0.68×10^{-5} .

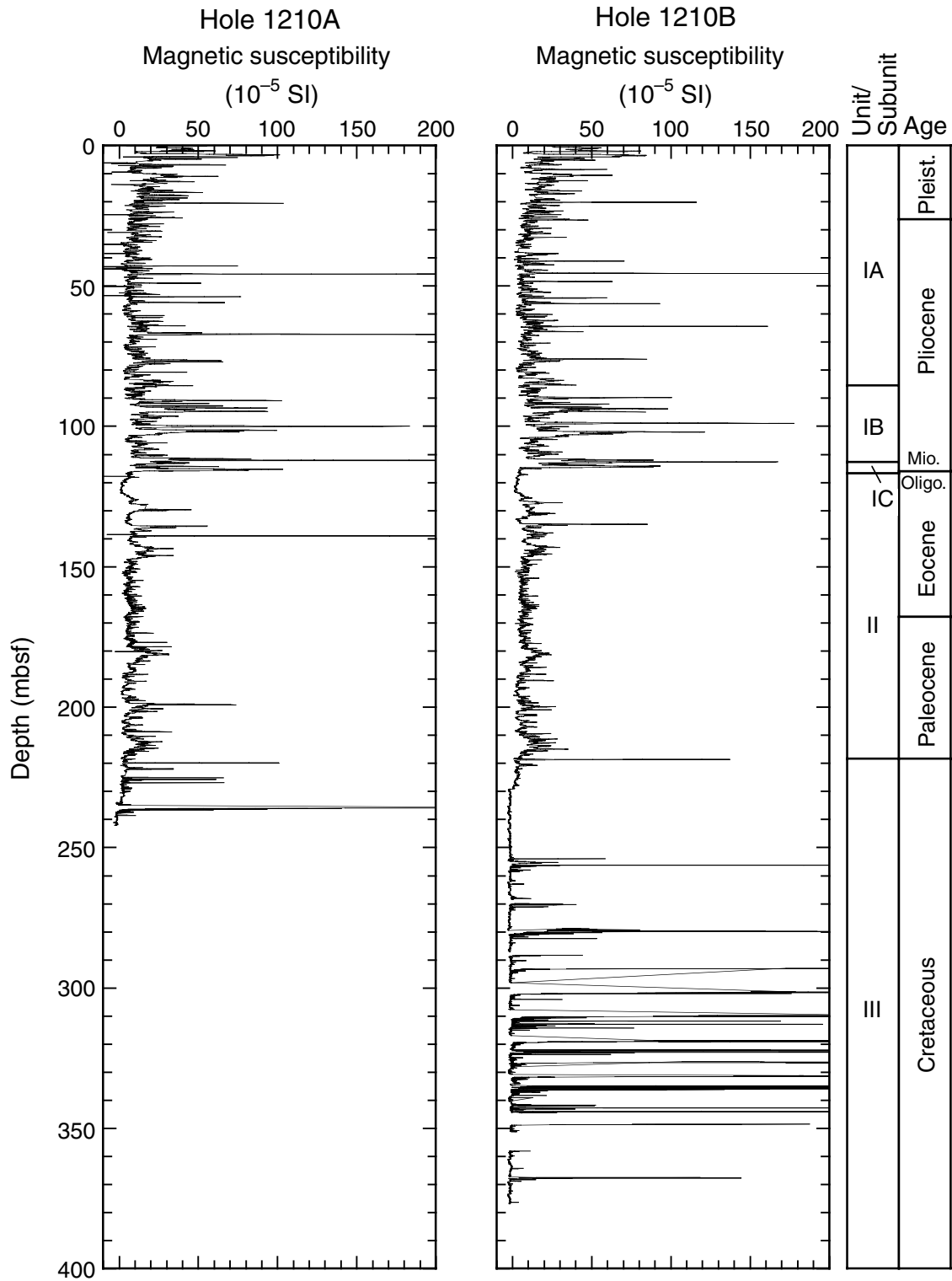


Figure F29. MST GRA bulk density (lines) measured in whole cores from Holes 1210A and 1210B plotted vs. depth. Discrete measurements of wet bulk density (see Table T14, p. 84) (solid circles) are plotted for comparison.

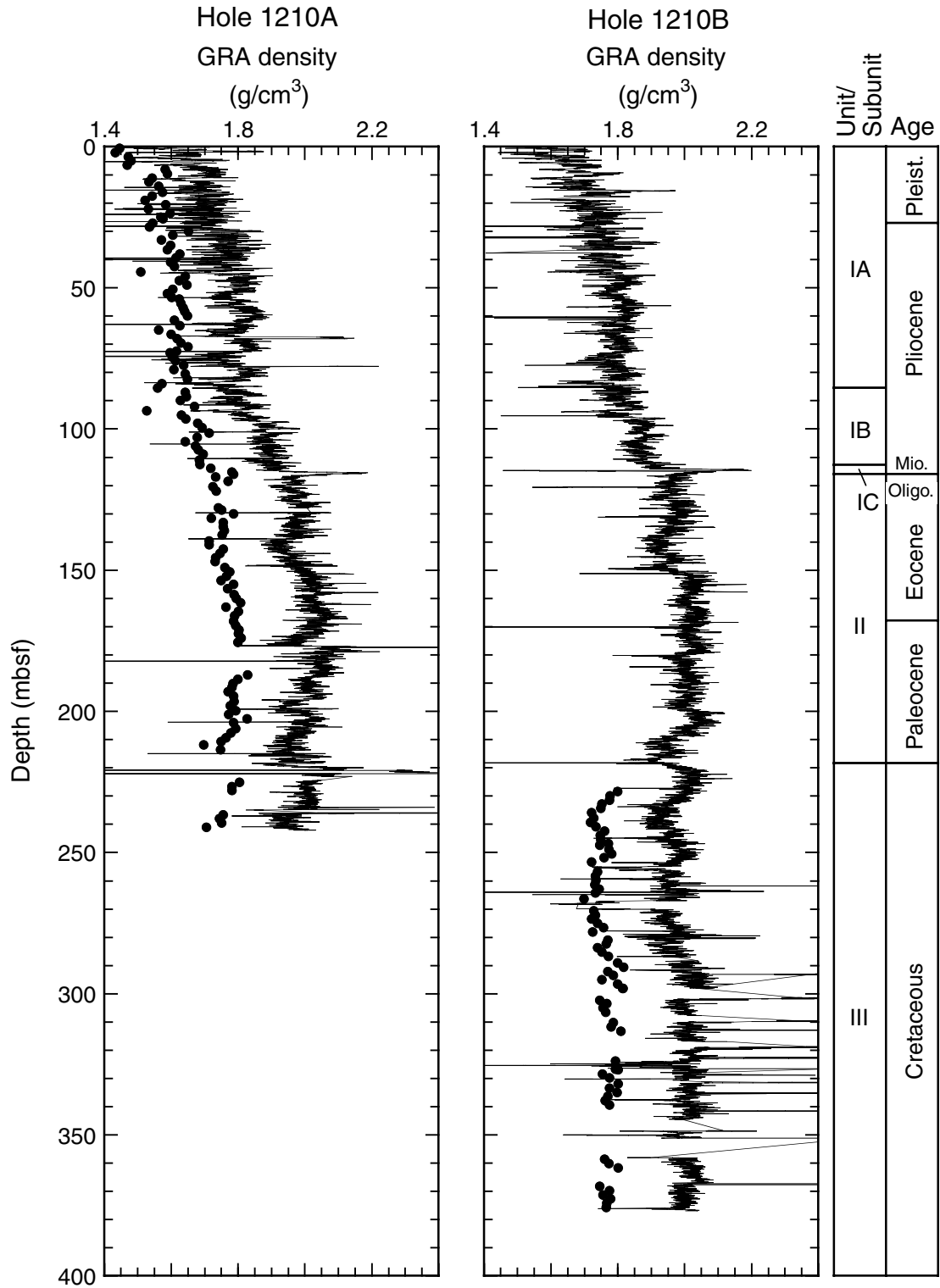


Figure F30. MST *P*-wave velocity (lines) measured in Holes 1210A and 1210B whole cores plotted vs. depth. For comparison, discrete *P*-wave velocity data (solid circles) are also shown.

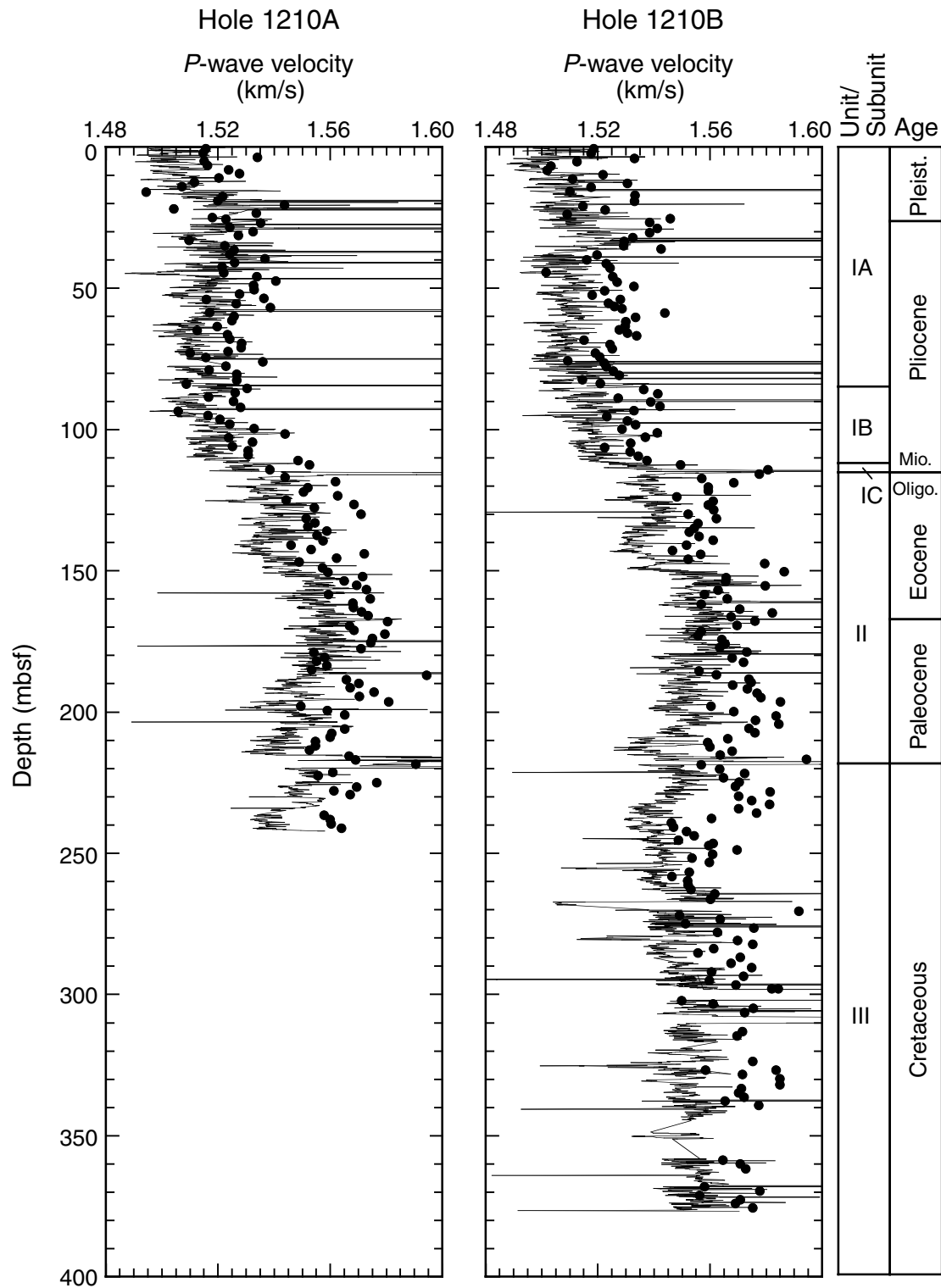


Figure F31. MST natural gamma radiation data for Holes 1210A and 1210B plotted vs. depth.

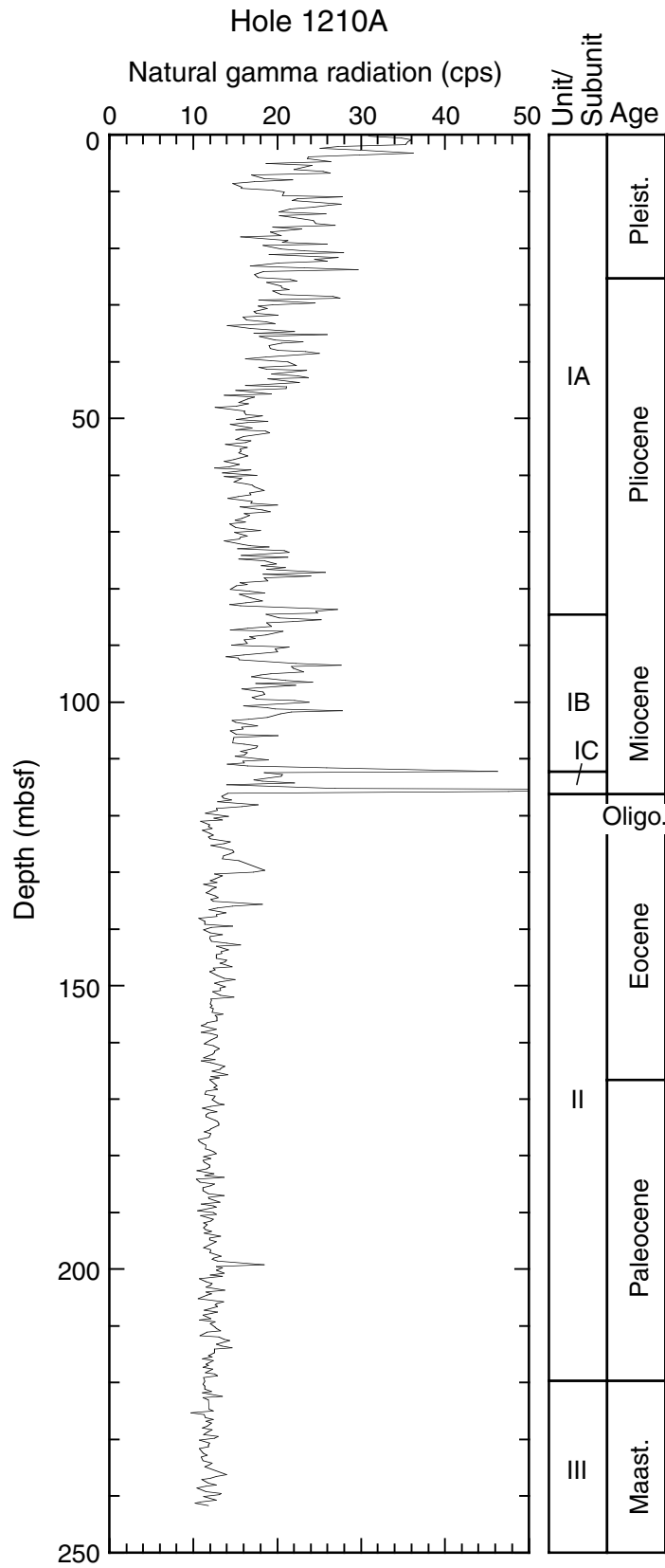


Figure F32. *P*-wave velocities for discrete samples from Holes 1210A and 1210B (see Table T15, p. 86, for data).

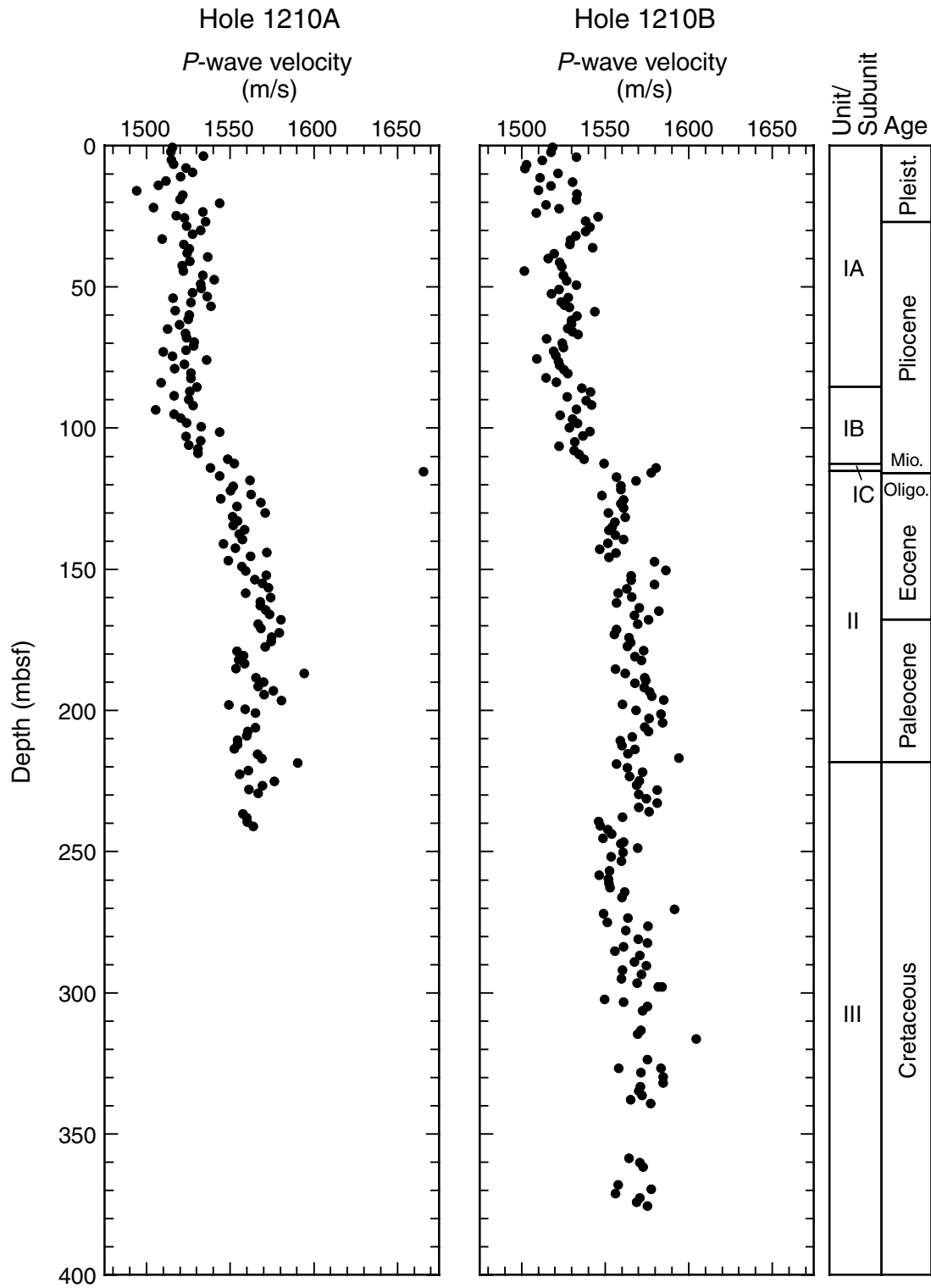


Figure F33. Discrete measurements of Hole 1210A *P*-wave velocities plotted vs. discrete wet bulk density measurements at comparable stratigraphic horizons.

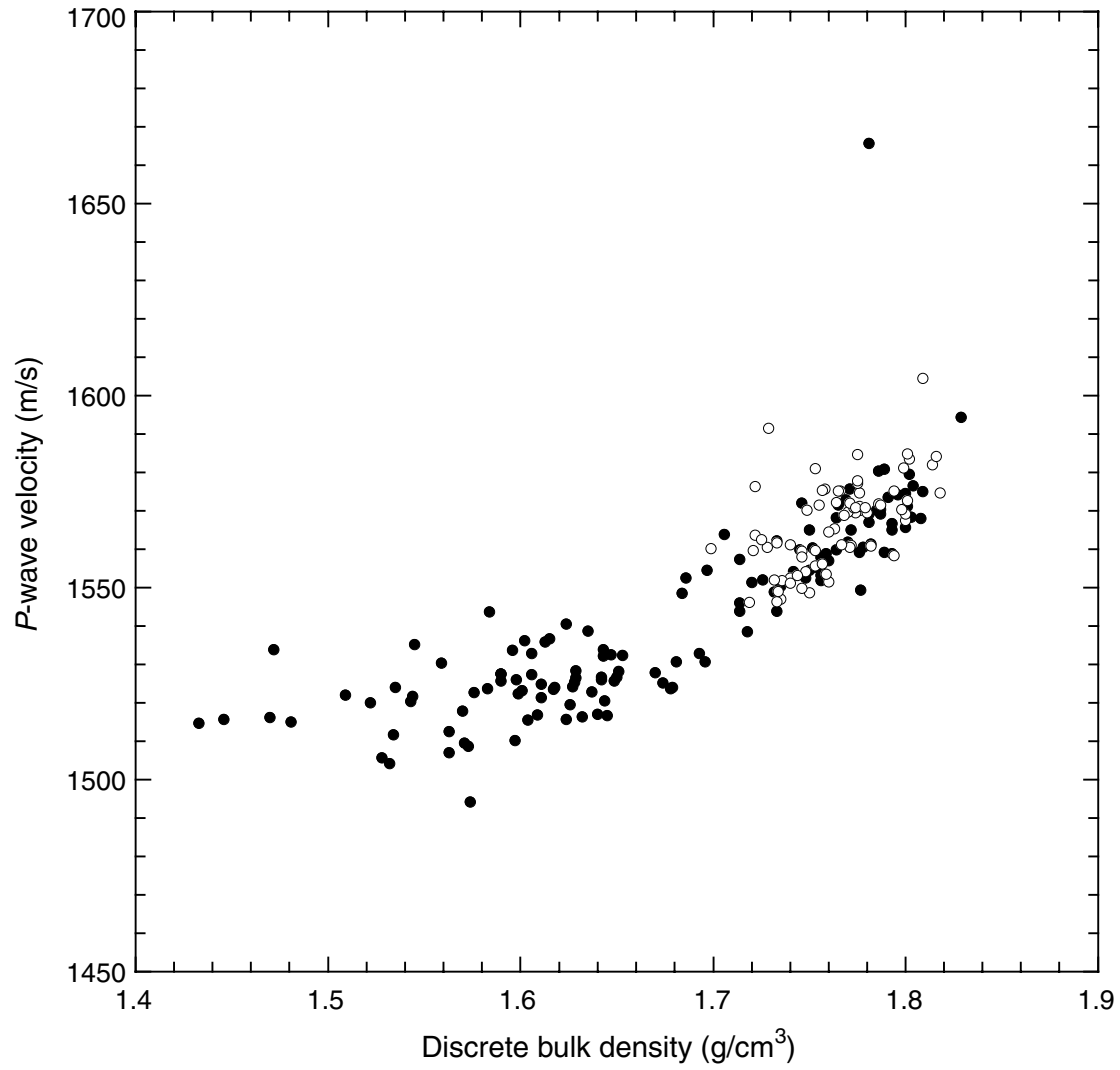


Figure F34. (A) Wet bulk density, (B) dry density, and (C) grain density determined for discrete samples from Hole 1210A (solid circles) and Hole 1210B (open circles) plotted vs. depth.

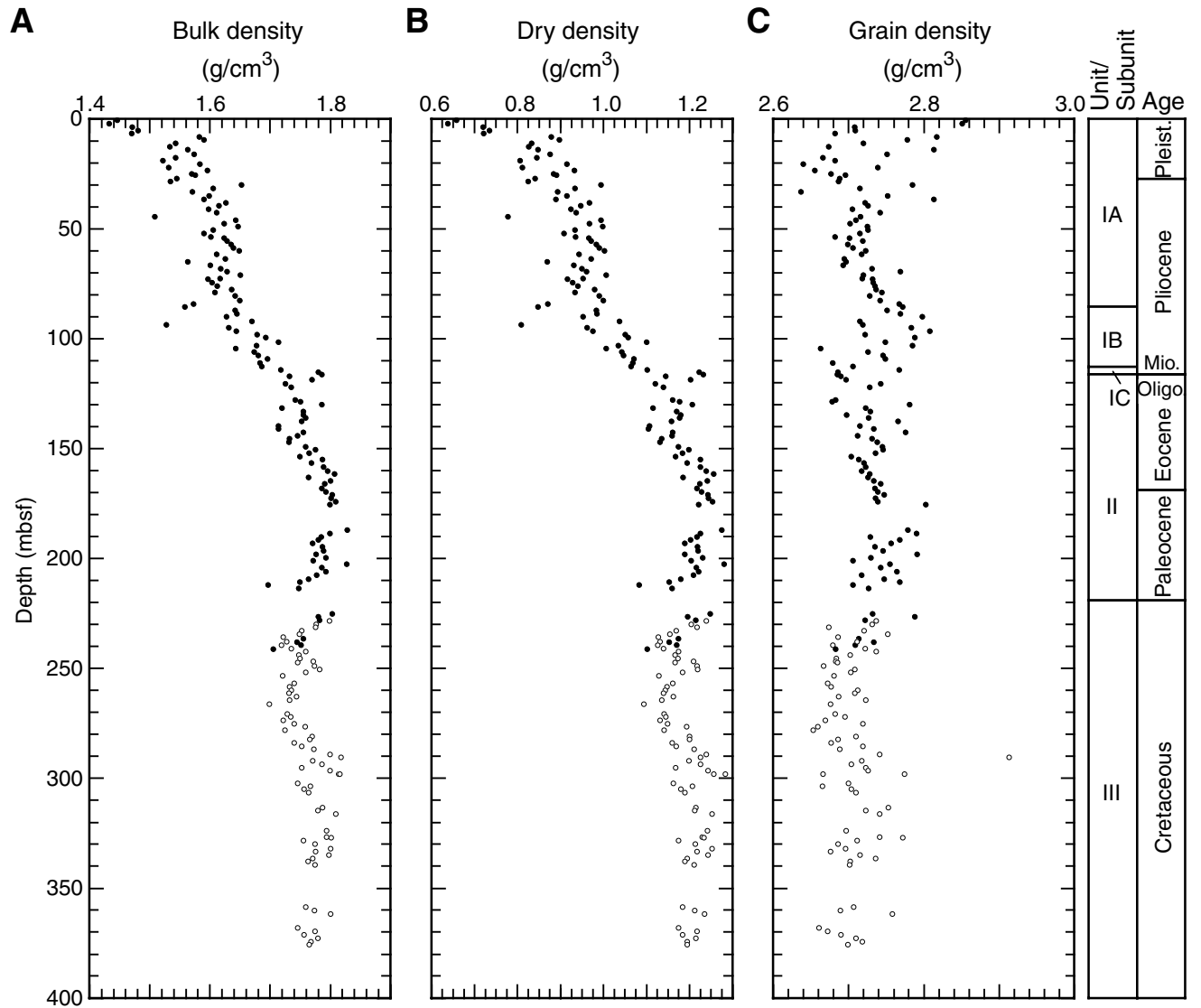


Figure F35. Water content (A) calculated relative to bulk sediment (circles) and solid phase (triangles), (B) porosity, and (C) void ratio determined for discrete samples from Hole 1210A (solid circles and triangles) and Hole 1210B (open circles and triangles) plotted vs. depth.

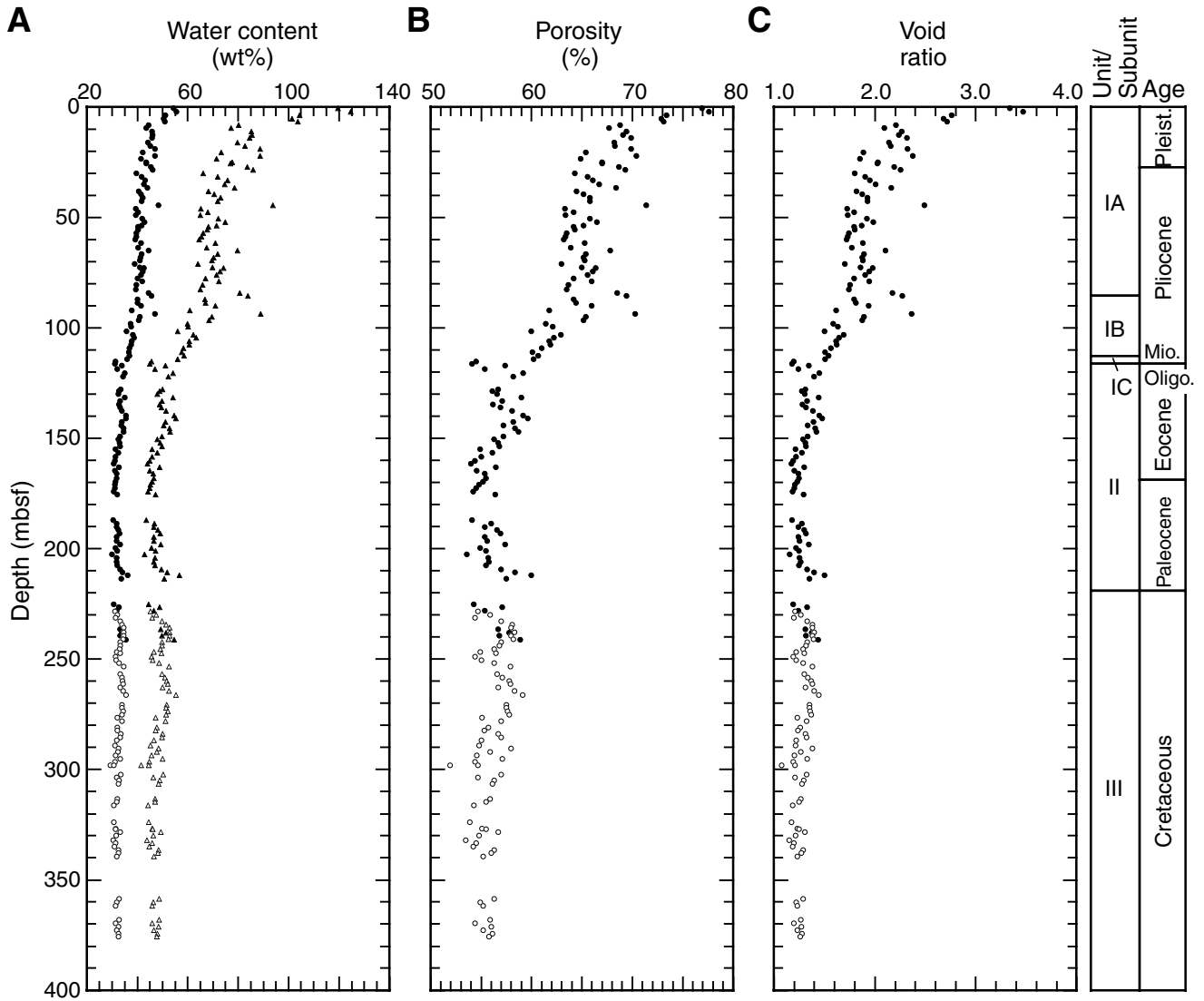


Table T1. Coring summary, Site 1210. (Continued on next page.)

Hole 1210A

Latitude: 32°13.4123'N
 Longitude: 158°15.5618'E
 Time on site (hr): 88.25 (0745 hr, 23 Sep–0000 hr, 27 Sep 2001)
 Time on hole (hr): 30.5 (0745 hr 23 Sep–1415 hr 24 Sep 2001)
 Seafloor (drill pipe measurement from rig floor, mbrf): 2584.6
 Distance between rig floor and sea level (m): 11.0
 Water depth (drill pipe measurement from sea level, m): 2573.6
 Total depth (drill pipe measurement from rig floor, mbrf): 2827.0
 Total penetration (mbsf): 242.4
 Total length of cored section (m): 241.4
 Total core recovered (m): 249.3
 Core recovery (%): 103.3
 Total number of cores: 27
 Total number of drilled intervals: 1

Hole 1210B

Latitude: 32°13.4203'N
 Longitude: 158°15.5623'E
 Time on hole (hr): 57.75 (1415 hr 24 Sep–0000 hr 27 Sep 2001)
 Seafloor (drill pipe measurement from rig floor, mbrf): 2584.3
 Distance between rig floor and sea level (m): 11.1
 Water depth (drill pipe measurement from sea level, m): 2573.2
 Total depth (drill pipe measurement from rig floor, mbrf): 2961.3
 Total penetration (mbsf): 377.0
 Total length of cored section (m): 365.5
 Total core recovered (m): 376.4
 Core recovery (%): 103.0
 Total number of cores: 42
 Total number of drilled intervals: 10

Core	Date (Sep 2001)	Local time (hr)	Depth (mbsf)		Length (m)		Recovery (%)	
			Top	Bottom	Cored	Recovered		
198-1210A-								
1H	23	1420	0.0	5.9	5.9	5.90	100.0	
2H	23	1515	5.9	15.4	9.5	9.79	103.1	
3H	23	1558	15.4	24.9	9.5	10.06	105.9	
4H	23	1647	24.9	34.4	9.5	9.92	104.4	
5H	23	1733	34.4	43.9	9.5	9.89	104.1	
6H	23	1815	43.9	53.4	9.5	10.09	106.2	
7H	23	1900	53.4	62.9	9.5	10.00	105.3	
8H	23	1952	62.9	72.4	9.5	10.08	106.1	
9H	23	2037	72.4	81.9	9.5	9.76	102.7	
10H	23	2122	81.9	91.4	9.5	9.95	104.7	
11H	23	2208	91.4	100.9	9.5	9.96	104.8	
12H	23	2250	100.9	110.4	9.5	9.95	104.7	
13H	23	2335	110.4	119.9	9.5	9.79	103.1	
14H	24	0030	119.9	129.4	9.5	9.59	100.9	
15H	24	0120	129.4	138.9	9.5	9.82	103.4	
16H	24	0210	138.9	148.4	9.5	9.72	102.3	
17H	24	0300	148.4	157.9	9.5	9.78	102.9	
18H	24	0350	157.9	167.4	9.5	9.59	100.9	
19H	24	0440	167.4	176.9	9.5	9.82	103.4	
20H	24	0530	176.9	186.4	9.5	9.74	102.5	
21H	24	0625	186.4	195.9	9.5	9.53	100.3	
22H	24	0710	195.9	205.4	9.5	9.83	103.5	
23H	24	0800	205.4	214.9	9.5	9.82	103.4	
24H	24	0855	214.9	224.4	9.5	9.28	97.7	
25H	24	0947	224.4	233.9	9.5	9.82	103.4	
26H	24	1035	233.9	234.9	1.0	1.24	124.0	
			*****Drilled from 234.9 to 235.9 mbsf*****					
27H	24	1230	235.9	242.4	6.5	6.58	101.2	
				Cored totals:	241.4	249.30	103.3	
				Drilled total:	1.0			
				Total:	242.4			
198-1210B-								
1H	24	1700	0.0	9.2	9.2	9.24	100.4	
2H	24	1735	9.2	18.7	9.5	8.99	94.6	
3H	24	1815	18.7	28.2	9.5	9.66	101.7	
4H	24	1900	28.2	37.7	9.5	8.88	93.5	

Table T1 (continued).

Core	Date (Sep 2001)	Local time (hr)	Depth (mbsf)		Length (m)		Recovery (%)
			Top	Bottom	Cored	Recovered	
5H	24	1950	37.7	47.2	9.5	9.76	102.7
6H	24	2035	47.2	56.7	9.5	10.08	106.1
7H	24	2125	56.7	66.2	9.5	9.86	103.8
8H	24	2205	66.2	75.7	9.5	10.13	106.6
9H	24	2247	75.7	85.2	9.5	10.05	105.8
10H	24	2345	85.2	94.7	9.5	10.16	106.9
11H	25	0030	94.7	104.2	9.5	9.94	104.6
12H	25	0125	104.2	113.7	9.5	9.98	105.1
13H	25	0210	113.7	123.2	9.5	9.84	103.6
14H	25	0300	123.2	132.7	9.5	9.95	104.7
15H	25	0350	132.7	142.2	9.5	9.53	100.3
16H	25	0440	142.2	151.7	9.5	9.75	102.6
17H	25	0530	151.7	161.2	9.5	9.50	100.0
18H	25	0620	161.2	170.7	9.5	9.76	102.7
19H	25	0710	170.7	180.2	9.5	9.66	101.7
20H	25	0800	180.2	189.7	9.5	9.85	103.7
21H	25	0850	189.7	199.2	9.5	9.61	101.2
22H	25	0935	199.2	208.7	9.5	9.91	104.3
23H	25	1020	208.7	218.2	9.5	9.96	104.8
24H	25	1110	218.2	227.7	9.5	9.97	104.9
25H	25	1205	227.7	237.2	9.5	9.82	103.4
26H	25	1250	237.2	246.7	9.5	9.99	105.2
27H	25	1335	246.7	256.2	9.5	9.79	103.1
28H	25	1505	256.2	265.7	9.5	9.25	97.4
29H	25	1550	265.7	267.9	2.2	3.73	169.5
30H	25	*****Drilled from 267.9 to 269.9 mbsf***** 1745	269.9	277.4	7.5	9.80	130.7
		*****Drilled from 277.4 to 278.4 mbsf*****					
		*****Drilled from 278.4 to 278.9 mbsf*****					
31H	25	2220	278.9	288.4	9.5	8.63	90.8
32H	25	2300	288.4	291.9	3.5	10.01	286.0
		*****Drilled from 291.9 to 292.9 mbsf*****					
33H	26	0055	292.9	299.3	6.4	5.59	87.3
		*****Drilled from 299.3 to 301.3 mbsf*****					
34H	26	0355	301.3	308.6	7.3	6.76	92.6
		*****Drilled from 308.6 to 309.6 mbsf*****					
35H	26	0545	309.6	317.6	8.0	7.62	95.2
		*****Drilled from 317.6 to 318.6 mbsf*****					
36H	26	0755	318.6	325.2	6.6	9.73	147.4
		*****Drilled from 325.2 to 326.2 mbsf*****					
37H	26	0930	326.2	330.2	4.0	4.77	119.2
		*****Drilled from 330.2 to 331.2 mbsf*****					
38H	26	1055	331.2	338.0	6.8	9.17	134.9
		*****Drilled from 338.0 to 339.0 mbsf*****					
39H	26	1245	339.0	348.5	9.5	5.75	60.5
40H	26	1410	348.5	358.0	9.5	2.85	30.0
41H	26	1500	358.0	367.5	9.5	9.48	99.8
42H	26	1605	367.5	377.0	9.5	9.60	101.1
			Cored totals:		365.5	376.40	103.0
			Drilled total:		11.5		
			Total:		377.0		

Table T2. Mineralogy of the clay fraction determined from shipboard XRD analyses, Site 1210A.

Core, section, interval (cm)	Clay mineralogy
198-1209A-	
5H-2, 117-118	Illite, saponite, smectite-kaolinite
5H-2, 118-119*	Saponite, illite
5H-2, 119-120	Illite, saponite, smectite-kaolinite
198-1210A-	
6H-1, 55-56*	Saponite, illite
6H-1, 59-60	Illite, saponite, smectite-kaolinite

Note: * = samples taken from pale green diagenetic laminae. All other samples are taken from the surrounding nannofossil ooze.

Table T3. Calcareous nannofossil datums, ages, and depths, Site 1210.

Datum	Zone/Subzone (base)	Core, section, interval (cm)	Depth (mbsf)	Core, section, interval (cm)	Depth (mbsf)	Age (Ma)
LO <i>Pseudoemiliana lacunosa</i>	CN14b	198-1210A-1H-CC	5.85	198-1210B-		0.46
LO <i>Gephyrocapsa caribbeanica</i>	CN13b	4H-CC	34.77			0.95
LO <i>Discoaster brouweri</i>	CN13a			3H-CC	28.26	1.95
LO <i>Discoaster pentaradiatus</i>	CN12d			4H-CC	37.03	2.52
LO <i>Discoaster surculus</i>	CN12b	5H-CC	44.24	5H-CC	47.36	2.53
LO <i>Reticulofenestra pseudoumbilicus</i>	CN12	6H-CC	53.94	6H-CC	57.18	3.82
LO <i>Amaurolithus</i> spp.	CN11	7H-CC	63.35			4.56
FO <i>Ceratolithus rugosus</i>	CN10c	8H-CC	72.93	8H-CC	76.28	5.10
LO <i>Discoaster quinqueramus</i>	CN10a	9H-CC	82.11	9H-CC	85.70	5.54
FO <i>Amaurolithus amplificus</i>	CN9b					7.39
FO <i>Discoaster berggrenii</i>	CN9	10H-CC	91.80	10H-CC	95.31	8.20
LO <i>Discoaster hamatus</i>	CN8	11H-6, 45	99.35			9.00
FO <i>Discoaster hamatus</i>	CN7	11H-7, 45	100.85			9.63
FO <i>Catinaster coalitus</i>	CN6	11H-CC	101.31			10.79
FO <i>Sphenolithus heteromorphus</i>	CN3	12H-CC	110.80	12H-CC	114.13	18.20
LO <i>Reticulofenestra umbilicus</i>	CP 17	13H-CC	120.14			32.30
TA <i>Ericsonia subdisticha</i>	CP16b					33.30
LO <i>Discoaster saipanensis</i>	CP16a	14-4H, 10	124.50	14H-1, 10	123.27	34.20
LO <i>Chiasmolithus grandis</i>	CP15	14H-CC	129.44	14H-2, 3	124.73	37.10
LO <i>Chiasmolithus solitus</i>	CP14b			14H-CC	133.10	40.40
FO <i>Chiasmolithus gigas</i>	CP13b	15H-CC	139.17	15H-CC	142.13	46.10
FO <i>Nannotetrina fulgens</i>	CP13a	16H-CC	148.57			47.30
FO <i>Discoaster sublodoensis</i>	CP12	17H-CC	158.13	17H-CC	161.15	49.70
FO <i>Coccolithus crassus</i>	CP11					51.50
FO <i>Discoaster lodoensis</i>	CP10	19H-CC	177.17	18H-CC	170.91	52.80
FO <i>Discoaster diastypus</i>	CP9a	20H-3, 100	180.90	20H-1, 50	180.70	55.00
FO <i>Discoaster multiradiatus</i>	CP8	20H-CC	186.59	20H-CC	190.00	56.20
FO <i>Discoaster nobilis</i>	CP7	21H-CC	195.88			56.90
FO <i>Discoaster mohleri</i>	CP6			21H-CC	199.26	57.50
FO <i>Ellipsolithus macellus</i>	CP3	22H-CC	205.68	22H-CC	209.06	62.20
FO <i>Chiasmolithus danicus</i>	CP2					63.80
FO <i>Cruciplacolithus tenuis</i>	CP1b			23H-CC	218.61	64.50
FO <i>Biantholithus sparsus</i>	CP1a	24H-4, 42	219.82	24H-1, 45	218.65	65.00
LO Cretaceous taxa	CP1a	24H-4, 42	219.82	24H-1, 45	218.65	65.00
FO <i>Micula prinsii</i>	CC26	24H-CC	224.13	24H-1, 53	218.73	65.40
LO <i>Lithraphidites quadratus</i>	CC25b/UC20	25H-CC	234.17	26H-CC	247.14	67.50
LO <i>Reinhardtites levis</i>	CC25a/UC19					69.20
LO <i>Tranolithus orionatus</i>	CC24/UC18			29H-2, 135	268.55	69.60
LO <i>Uniplanarius trifidum</i>	CC23c			30H-CC	279.65	71.30
FO <i>Uniplanarius trifidum</i>	CC22			39H-CC	344.70	76.00

Note: FO = first occurrence, LO = last occurrence, TA = top acme.

Table T4. Planktonic foraminiferal datums, ages, and depths, Site 1210.

Datum	Zone/ Subzone (base)	Core, section, interval (cm)	Depth (mbsf)	Core, section, interval (cm)	Depth (mbsf)	Age (Ma)
		198-1210A-		198-1210B-		
LO <i>Globigerinoides obliquus</i>		3H-CC	25.41	3H-CC	28.26	1.3
FO <i>Truncorotalia truncatulinoides</i>	N22	4H-CC	34.77	3H-CC	28.26	1.92
LO <i>Globigerinoides extremus</i>		5H-CC	44.24	5H-CC	47.36	1.98
FO <i>Truncorotalia tosaensis</i>	N21	6H-CC	53.94	6H-CC	57.18	3.35
LO <i>Dentoglobigerina altispira</i>		6H-CC	53.94	5H-CC	47.36	3.11
LO <i>Sphaeroidinellopsis seminulina</i>		6H-CC	53.94	5H-CC	47.36	3.11
LO <i>Globorotalia margaritae</i>		8H-CC	72.93	7H-CC	66.51	3.85
FO <i>Truncorotalia tosaensis</i>		6H-CC	53.94	5H-CC	47.36	4.31
LO <i>Globoturborotalita nepenthes</i>		9H-CC	82.11	10H-CC	95.31	4.39
FO <i>Globorotalia tumida</i>	N18	9H-CC	82.11	7H-CC	66.51	5.82
FO <i>Globorotalia margaritae</i>		9H-CC	82.11	8H-CC	76.28	6.09
LO <i>Paragloborotalia mayeri</i>	N15			11H-CC	104.59	10.49
FO <i>Globoturborotalita nepenthes</i>	N14	11H-CC	101.31	11H-CC	104.59	11.19
FO <i>Orbulina universa</i>	N9	12H-CC	110.80	12H-CC	114.13	15.1
FO <i>Praeorbulina sicana</i>	N8					16.4
FO <i>Globoquadrina dehiscescens</i>	M1b	12H-CC	110.80	12H-CC	114.13	23.2
LO <i>Subbotina angiporoides</i>						30
LO <i>Pseudohastigerina</i> spp.	P19	13H-CC	120.14	13H-CC	123.00	32
LO <i>Hantkenina</i> spp.		15H-CC	139.17	14H-1, 7-8	123.27	33.7
LO <i>Globigerinatheka index</i>				14H-CC	133.10	34.3
LO <i>Acarinina primitiva</i>		16H-CC	148.57	15H-CC	142.13	39.0
LO "Orbulinoides" <i>beckmanni</i>	P14					40.1
FO "Orbulinoides" <i>beckmanni</i>	P13					40.5
LO <i>Acarinina bullbrookii</i>		15H-CC	139.17	15H-CC	142.13	40.5
FO <i>Turborotalia pomeroli</i>						
LO <i>Morozovella aragonensis</i>	P12	16H-CC	148.57	15H-CC	142.13	43.6
FO <i>Globigerinatheka kugleri</i>	P11					45.8
FO <i>Hantkenina</i> spp.	P10	15H-CC	139.17	15H-CC	142.13	49.0
LO <i>Morozovella formosa</i>	P8	18H-CC	167.44	18H-CC	170.91	50.8
FO <i>Acarinina pentacamerata</i>		18H-CC	167.44	17H-CC	161.15	50.8
FO <i>Morozovella aragonensis</i>	P7	19H-CC	177.17	18H-CC	170.91	52.3
LO <i>Morozovella aequa</i>		21H-CC	195.88	19H-CC	180.31	53.6
FO <i>Morozovella formosa</i>	P6b	19H-CC	177.17	19H-CC	180.31	54.0
LO <i>Morozovella velascoensis</i>	P6a	20H-CC	186.59	20H-CC	190.00	54.7
FO <i>Morozovella gracilis</i>		19H-CC	177.17	19H-CC	180.31	54.7
FO <i>Morozovella subbotinae</i>		20H-CC	186.59	20H-CC	190.00	55.9
LO <i>Globanomalina pseudomenardii</i>	P5	21H-CC	195.88	20H-CC	190.00	55.9
LO <i>Acarinina mckannai</i>		21H-CC	195.88			56.3
FO <i>Acarinina mckannai</i>		21H-CC	195.88			59.1
FO <i>Globanomalina pseudomenardii</i>	P4a	22H-CC	205.68	21H-CC	199.26	59.2
FO <i>Morozovella velascoensis</i>		22H-CC	205.68	21H-CC	199.26	60.0
FO <i>Morozovella conicotruncata</i>		23H-CC	215.17	22H-CC	209.06	60.9
FO <i>Morozovella angulata</i>		23H-CC	215.17	22H-CC	209.06	61.0
FO <i>Igorina pusilla</i>		23H-CC	215.17	22H-CC	209.06	61.0
FO <i>Praemurica uncinata</i>	P2					61.2
FO <i>Praemurica inconstans</i>						63
LO <i>Parvularugoglobigerina eugubina</i>	P1a	24H-4, 24-25	219.64	24H-1, 5-6	218.25	64.7
FO <i>Parvularugoglobigerina eugubina</i>	P1a	24H-4, 49-50	219.89	24H-1, 48-49	218.68	64.97
LO <i>Abathomphalus mayaroensis</i>		24H-CC	224.13	24H-1, 57-58	218.77	65.0
FO <i>Abathomphalus mayaroensis</i>	KS31	27H-CC	242.38	25H-CC	237.47	68.6
FO <i>Racemiguembelina fructicosa</i>		27H-CC	242.38	27H-CC	256.44	69.6
FO <i>Contusotruncana contusa</i>		27H-CC	242.38	27H-CC	256.44	69.6

Table T7. Composite depth section, Site 1210.

Core	Depth (mbsf)	Offset (m)	Depth (mcd)	Core	Depth (mbsf)	Offset (m)	Depth (mcd)
198-1210A-				8H	66.2	7.58	73.78
1H	0.0	0.00	0.00	9H	75.7	8.61	84.31
2H	5.9	1.51	7.41	10H	85.2	9.25	94.45
3H	15.4	1.19	16.59	11H	94.7	10.70	105.40
4H	24.9	2.28	27.18	12H	104.2	12.51	116.71
5H	34.4	3.10	37.50	13H	113.7	14.11	127.81
6H	43.9	4.52	48.42	14H	123.2	15.14	138.34
7H	53.4	5.55	58.95	15H	132.7	17.49	150.19
8H	62.9	6.29	69.19	16H	142.2	18.37	160.57
9H	72.4	7.65	80.05	17H	151.7	19.49	171.19
10H	81.9	8.26	90.16	18H	161.2	20.34	181.54
11H	91.4	9.56	100.96	19H	170.7	21.64	192.34
12H	100.9	11.34	112.24	20H	180.2	21.08	201.28
13H	110.4	13.00	123.40	21H	189.7	21.24	210.94
14H	119.9	14.48	134.38	22H	199.2	22.87	222.07
15H	129.4	16.71	146.11	23H	208.7	24.38	233.08
16H	138.9	17.86	156.76	24H	218.2	25.56	243.76
17H	148.4	18.65	167.05	25H	227.7	26.44	254.14
18H	157.9	19.53	177.43	26H	237.2	26.44	263.64
19H	167.4	20.89	188.29	27H	246.7	26.44	273.14
20H	176.9	20.84	197.74	28H	256.2	26.44	282.64
21H	186.4	20.94	207.34	29H	265.7	26.44	292.14
22H	195.9	22.18	218.08	30H	269.9	26.44	296.34
23H	205.4	23.48	228.88	31H	278.9	26.44	305.34
24H	214.9	24.45	239.35	32H	288.4	26.44	314.84
25H	224.4	23.71	248.11	33H	292.9	26.44	319.34
26H	233.9	23.71	257.61	34H	301.3	26.44	327.74
27H	235.9	23.22	259.12	35H	309.6	26.44	336.04
198-1210B-				36H	318.6	26.44	345.04
1H	0.0	-0.18	-0.18	37H	326.2	26.44	352.64
2H	9.2	1.75	10.95	38H	331.2	26.44	357.64
3H	18.7	1.49	20.19	39H	339.0	26.44	365.44
4H	28.2	3.24	31.44	40H	348.5	26.44	374.94
5H	37.7	4.78	42.48	41H	358.0	26.44	384.44
6H	47.2	5.12	52.32	42H	367.5	26.44	393.94
7H	56.7	6.03	62.73				

Table T8. Splice tie points, Site 1210.

Core, section, interval (cm)	Depth			Core, section, interval (cm)	Depth	
	(mbsf)	(mcd)			(mbsf)	(mcd)
198-				198-		
1210A-1-H-2, 60	2.10	2.10	Tie to	1210B-1-H-2, 78	2.28	2.10
1210B-1-H-6, 108	8.58	8.40	Tie to	1210A-2-H-1, 99	6.89	8.40
1210A-2-H-4, 60	11.00	12.51	Tie to	1210B-2-H-2, 6	10.76	12.51
1210B-2-H-5, 96	16.16	17.91	Tie to	1210A-3-H-1, 132	16.72	17.91
1210A-3-H-5, 33	21.73	22.92	Tie to	1210B-3-H-2, 123	21.43	22.92
1210B-3-H-6, 27	26.47	27.96	Tie to	1210A-4-H-1, 78	25.68	27.96
1210A-4-H-4, 108	30.48	32.76	Tie to	1210B-4-H-1, 132	29.52	32.76
1210B-4-H-5, 108	35.28	38.52	Tie to	1210A-5-H-1, 102	35.42	38.52
1210A-5-H-6, 96	42.86	45.96	Tie to	1210B-5-H-3, 48	41.18	45.96
1210B-5-H-7, 30	47.00	51.78	Tie to	1210A-6-H-3, 36	47.26	51.78
1210A-6-H-7, 12	53.02	57.54	Tie to	1210B-6-H-4, 72	52.42	57.54
1210B-6-H-7, 21	56.41	61.53	Tie to	1210A-7-H-2, 108	55.98	61.53
1210A-7-H-5, 120	60.60	66.15	Tie to	1210B-7-H-3, 46.5	60.12	66.15
1210B-7-H-6, 36	64.51	70.54	Tie to	1210A-8-H-1, 135	64.25	70.54
1210A-8-H-5, 6	68.96	75.25	Tie to	1210B-8-H-1, 147	67.67	75.25
1210B-8-H-5, 117	73.37	80.95	Tie to	1210A-9-H-1, 90	73.30	80.95
1210A-9-H-4, 21	77.11	84.76	Tie to	1210B-9-H-1, 45	76.15	84.76
1210B-9-H-7, 51	85.21	93.82	Tie to	1210A-10-H-3, 66	85.56	93.82
1210A-10-H-6, 141	90.81	99.07	Tie to	1210B-10-H-4, 12	89.82	99.07
1210B-10-H-6, 96	93.66	102.91	Tie to	1210A-11-H-2, 45	93.35	102.91
1210A-11-H-6, 102	99.92	109.48	Tie to	1210B-11-H-3, 108	98.78	109.48
1210B-11-H-6, 48	102.68	113.38	Tie to	1210A-12-H-1, 114	102.04	113.38
1210A-12-H-7, 42	110.32	121.66	Tie to	1210B-12-H-4, 45	109.15	121.66
1210B-12-H-6, 81	112.51	125.02	Tie to	1210A-13-H-2, 12	112.02	125.02
1210A-13-H-4, 87	115.77	128.77	Tie to	1210B-13-H-1, 96	114.66	128.77
1210B-13-H-7, 51	123.21	137.32	Tie to	1210A-14-H-2, 144	122.84	137.32
1210A-14-H-6, 57	127.97	142.45	Tie to	1210B-14-H-3, 111	127.31	142.45
1210B-14-H-6, 84	131.54	146.68	Tie to	1210A-15-H-1, 57	129.97	146.68
1210A-15-H-5, 18	135.58	152.29	Tie to	1210B-15-H-2, 60	134.80	152.29
1210B-15-H-5, 114	139.84	157.33	Tie to	1210A-16-H-1, 57	139.47	157.33
1210A-16-H-4, 24	143.64	161.50	Tie to	1210B-16-H-1, 93	143.13	161.50
1210B-16-H-6, 144	151.14	169.51	Tie to	1210A-17-H-2, 96	150.86	169.51
1210A-17-H-5, 48	154.88	173.53	Tie to	1210B-17-H-2, 84	154.04	173.53
1210B-17-H-6, 135	160.55	180.04	Tie to	1210A-18-H-2, 109.5	160.51	180.04
1210A-18-H-5, 93	164.83	184.36	Tie to	1210B-18-H-2, 132	164.02	184.36
1210B-18-H-6, 138	170.08	190.42	Tie to	1210A-19-H-2, 63	169.53	190.42
1210A-19-H-5, 21	173.61	194.50	Tie to	1210B-19-H-2, 66	172.86	194.50
1210B-19-H-6, 96	179.16	200.80	Tie to	1210A-20-H-3, 6	179.96	200.80
1210A-20-H-3, 108	180.98	201.82	Tie to	1210B-20-H-1, 54	180.74	201.82
1210B-20-H-6, 60	188.30	209.38	Tie to	1210A-21-H-2, 54	188.44	209.38
1210A-21-H-3, 138	190.78	211.72	Tie to	1210B-21-H-1, 78	190.48	211.72
1210B-21-H-6, 129	198.49	219.73	Tie to	1210A-22-H-2, 15	197.55	219.73
1210A-22-H-6, 12	203.52	225.70	Tie to	1210B-22-H-3, 63	202.83	225.70
1210B-22-H-6, 36	207.06	229.93	Tie to	1210A-23-H-1, 105	206.45	229.93
1210A-23-H-7, 18	214.58	238.06	Tie to	1210B-23-H-4, 46.5	213.68	238.06
1210B-23-H-6, 54	216.74	241.12	Tie to	1210A-24-H-2, 27	216.67	241.12
1210A-24-H-5, 114	222.04	246.49	Tie to	1210B-24-H-2, 123	220.93	246.49
1210B-24-H-5, 114	225.34	250.90	Tie to	1210A-25-H-2, 129	227.19	250.90
1210A-25-H-7, 57	233.97	257.68				

Table T9. Linear sedimentation rate segments used to calculate mass accumulation rates and average accumulation rates.

Segment	Depth (mbsf)		Age (Ma)		Age	Average accumulation rate (g/cm ² /k.y.)		
	Top	Bottom	Top	Bottom		Bulk sediment	Carbonate	Noncarbonate
1*	0.00	88.75	0.00	5.54	latest Miocene–Pleistocene	1.4	1.1	0.3
2*	88.75	102.95	5.54	10.79	middle Miocene–late Miocene	0.3	0.2	0.1
3	102.95	113.38	10.79	18.20	early Miocene–middle Miocene	0.1	0.1	0.0
4	113.38	115.58	18.20	32.30	early Oligocene–early Miocene	0.0	0.0	0.0
5	115.58	124.37	32.30	33.30	early Oligocene	1.0	1.0	0.0
6	124.37	145.35	33.30	46.10	middle Eocene–earliest Oligocene	0.2	0.2	0.0
7	145.35	178.74	46.10	52.80	early Eocene–middle Eocene	0.6	0.6	0.0
8	178.74	181.80	52.80	55.00	latest Paleocene–early Eocene	NA	NA	NA
9	181.80	202.47	55.00	57.50	late Paleocene	0.9	0.9	0.0
10	202.47	219.53	57.50	65.00	early Paleocene–late Paleocene	0.3	0.3	0.0
11	226.13	244.80	65.40	68.60	late Maastrichtian	0.7	0.6	0.0
12	244.80	322.70	68.60	75.20	late Campanian–late Maastrichtian	1.4	1.3	0.1
13	322.70	348.00	75.20	76.00	late Campanian	3.8	3.7	0.1

Notes: * = MARs based on nannofossil datums. NA = no dry bulk density or carbonate concentration data available.

Table T10. Concentrations of CH₄ in headspace gas, Hole 1210A.

Core, section, interval (cm)	Depth (mbsf)	CH ₄ (ppmv)
198-1210A-		
1H-4, 0-5	4.5	1.9
2H-5, 0-5	11.9	2.0
3H-5, 0-5	21.4	2.2
4H-5, 0-5	30.9	1.9
5H-5, 0-5	40.4	2.1
6H-5, 0-5	49.9	2.0
7H-5, 0-5	59.4	1.9
8H-5, 0-5	68.9	2.2
9H-5, 0-5	78.4	2.0
10H-5, 0-5	87.9	2.0
11H-4, 0-5	95.9	1.8
12H-5, 0-5	106.9	2.0
13H-5, 0-5	116.4	2.0
16H-5, 0-5	144.9	1.9
19H-5, 0-5	173.4	1.8
22H-6, 0-5	203.4	1.7
25H-5, 0-5	230.4	1.7

Table T11. Carbonate content, Hole 1210A.

Core, section, interval (cm)	Depth (mbsf)	Total inorganic carbon (wt%)	CaCO ₃ (wt%)	Core, section, interval (cm)	Depth (mbsf)	Total inorganic carbon (wt%)	CaCO ₃ (wt%)
198-1210A-				17H-5, 73-74	155.13	11.5	95.7
1H-1, 70-71	0.70	6.2	51.4	18H-5, 72-73	164.62	11.4	95.2
1H-4, 70-71	5.20	7.3	60.5	18H-6, 39-40	165.79	11.3	93.9
2H-3, 70-71	9.60	9.9	82.2	19H-1, 66-67	168.06	11.7	97.2
2H-6, 70-71	14.10	8.5	70.7	19H-5, 21-22	173.61	10.9	90.7
3H-1, 66-67	16.06	6.1	50.5	19H-6, 60-61	175.50	12.0	100.0
3H-2, 72-73	17.62	8.6	71.8	21H-1, 73-74	187.13	11.7	97.1
3H-6, 72-73	23.62	8.5	71.0	21H-5, 119-120	193.59	11.5	95.4
4H-3, 67-68	28.57	7.0	58.1	21H-6, 133-134	195.23	11.9	99.0
4H-4, 67-68	30.07	10.0	83.1	22H-1, 71-72	196.61	11.8	98.0
5H-1, 73-74	35.13	9.1	76.0	22H-2, 70-71	198.10	11.8	98.5
5H-4, 63-64	39.53	10.6	88.3	22H-3, 30-31	199.20	9.1	75.6
5H-5, 31-32	40.71	6.4	53.6	22H-3, 68-69	199.58	11.6	96.4
6H-1, 73-74	44.63	6.1	50.9	22H-4, 70-71	201.10	11.9	99.8
6H-3, 73-74	47.63	10.4	86.4	23H-2, 70-71	207.60	11.8	98.5
6H-5, 72-73	50.62	10.4	86.4	23H-6, 71-72	213.61	0.2	1.3
7H-1, 73-74	54.13	10.4	86.9	26H-CC, 0-1	235.04	3.3	27.7
7H-3, 5-6	56.45	9.5	79.1	27H-4, 72-73	241.12	12.1	100.7
7H-5, 73-74	60.13	10.9	90.7	198-1210B-			
8H-2, 72-73	65.12	8.2	73.5	27H-5, 72-73	253.42	11.6	96.7
8H-5, 72-73	69.62	10.3	87.7	26H-1, 70-71	237.90	11.7	97.0
9H-3, 73-74	76.13	10.0	83.1	26H-5, 92-93	244.12	11.7	97.1
9H-4, 84-85	77.74	6.4	53.4	26H-7, 68-69	246.88	11.7	97.0
9H-5, 73-74	79.23	9.6	79.8	28H-1, 71-72	256.91	11.8	97.9
10H-2, 71-72	84.11	7.5	62.3	28H-6, 72-73	264.42	11.7	97.3
10H-5, 71-72	88.61	10.7	88.9	29H-1, 71-72	266.41	11.7	97.4
11H-1, 72-73	92.12	10.8	89.9	30H-1, 69-70	270.59	11.7	97.0
11H-4, 72-73	96.62	9.4	78.1	30H-1, 71-72	270.61	11.7	97.0
12H-1, 71-72	101.61	8.7	72.2	30H-5, 39-40	276.29	11.6	96.7
12H-4, 70-71	106.10	11.0	91.2	31H-3, 72-73	282.39	10.6	88.3
12H-6, 71-72	109.11	10.6	88.6	31H-5, 72-73	285.39	11.6	96.7
13H-2, 35-36	112.25	4.2	35.1	32H-1, 73-74	289.13	11.6	96.8
13H-3, 71-72	114.11	10.9	90.6	32H-3, 73-74	292.13	11.6	96.3
13H-4, 76-77	115.66	2.9	24.0	33H-1, 96-97	293.86	11.4	95.0
13H-5, 71-72	117.11	11.4	95.1	33H-3, 72-73	296.62	11.5	96.0
14H-2, 71-72	122.11	11.6	96.4	34H-1, 124-125	302.54	11.4	95.2
14H-6, 60-61	128.00	11.1	92.5	34H-3, 73-74	305.03	11.5	95.6
14H-7, 70-71	128.80	11.5	95.7	35H-4, 73-74	314.83	11.4	95.1
15H-2, 67-68	131.57	11.5	96.1	36H-6, 71-72	326.81	11.4	94.6
15H-5, 18-19	135.58	8.8	72.8	37H-3, 70-71	329.90	11.5	95.9
15H-5, 76-77	136.16	10.6	88.6	38H-2, 70-71	333.40	11.6	96.7
16H-1, 72-73	139.62	11.5	96.0	41H-1, 74-75	358.74	11.6	96.5
16H-3, 75-76	142.65	11.4	95.0	41H-3, 73-74	361.73	11.6	96.6
16H-3, 102-103	142.92	11.2	93.1	42H-1, 71-72	368.21	11.7	97.8
17H-1, 73-74	149.13	11.2	93.5	42H-6, 65-66	375.65	11.6	97.0
17H-2, 63-64	150.53	11.6	96.7				

Table T12. Results from CNSH analysis of samples, Hole 1210A.

Core, section, interval (cm)	Depth (mbsf)	Organic carbon (wt%)	Nitrogen (wt%)	Sulfur (wt%)	Hydrogen (wt%)	C/N ratio (atomic)
198-1210A-						
1H-1, 70-71	0.70	0.41	0.07	0.04	0.38	5.0
3H-1, 66-67	16.06	0.23	0.02	0.00	0.38	9.9
6H-1, 73-74	44.63	0.15	0.03	0.05	0.41	4.3
9H-4, 84-85	77.74	0.00	0.02	0.00	0.41	NA
13H-4, 76-77	115.66	0.00	0.02	0.15	0.87	NA
19H-5, 21-22	173.61	0.00	0.02	0.03	0.11	NA
22H-3, 30-31	199.20	0.00	0.02	0.12	0.22	NA
26H-CC, 0-1	235.04	0.00	0.02	0.00	0.41	NA

Note: NA = not applicable.

Table T13. Results of geochemical analyses, Hole 1210A.

Core, section, interval (cm)	Depth (mbsf)	pH	Alkalinity (mM)	Salinity	Cl ⁻ (mM)	SO ₄ ²⁻ (mM)	Na ⁺ (mM)	Mg ²⁺ (mM)	Ca ²⁺ (mM)	K ⁺ (mM)	H ₄ SiO ₄ (μM)	NH ₄ ⁺ (μM)	HPO ₄ ²⁻ (μM)	Sr ²⁺ (μM)	Fe ²⁺ (μM)	Mn ²⁺ (μM)	Li ⁺ (μM)	Ba ²⁺ (μM)	H ₃ BO ₃ (μM)
198-1210A-																			
1H-3, 145-150	4.45	7.26	2.91	35.0	553	29	469	55.2	10.9	12.6	627	86	2.9	107	43	17	22.9	0.3	432
2H-4, 145-150	11.85	7.39	3.30	35.0	554	27	473	52.6	10.9	12.2	608	96	1.8	147	53	17	20.0	1.0	454
3H-4, 145-150	21.35	7.40	3.36	35.0	558	27	477	51.7	11.1	12.5	637	105	1.6	190	16	8	19.1	0.3	471
4H-4, 145-150	30.85	7.38	3.25	35.0	558	26	477	51.1	11.2	12.4	695	105	1.3	209	24	3	16.8	0.2	282
5H-4, 145-150	40.35	7.43	3.16	35.0	558	26	476	50.4	11.7	12.3	662	118	0.9	244	12	2	17.0	0.2	449
6H-4, 145-150	49.85	7.36	3.30	35.0	561	25	482	48.4	11.9	11.9	650	112	0.9	274	11	1	16.1	0.3	451
7H-4, 145-150	59.35	7.24	3.17	35.0	561	25	479	49.3	12.0	11.3	616	108	0.6	294	13	1	16.7	0.6	468
8H-4, 145-150	68.85	7.35	3.04	35.0	558	25	476	49.1	11.9	11.6	658	114	0.4	305	12	1	16.9	0.3	458
9H-4, 145-150	78.35	7.33	2.97	35.0	560	25	483	47.8	11.6	11.4	627	105	0.6	319	13	2	16.8	0.7	457
10H-4, 145-150	87.85	7.28	3.03	35.0	562	25	482	48.0	12.6	11.4	550	101	0.6	325	8	4	18.0	0.2	466
11H-3, 145-150	95.85	7.36	2.91	35.0	560	25	481	47.5	12.5	11.0	477	94	0.4	332	8	8	19.1	0.3	489
16H-4, 140-150	144.80	7.43	2.57	35.0	561	24	482	46.4	12.9	10.3	229	68	0.3	311	5	1	26.7	0.3	522
19H-4, 145-150	173.35	7.49	2.45	35.0	563	25	481	47.6	14.1	10.5	212	61	0.3	306	5	3	28.6	0.3	503
22H-5, 145-150	203.35	7.41	2.52	35.0	563	23	483	45.5	13.5	10.5	260	64	0.3	299	26	1	31.4	0.4	522
25H-4, 140-150	230.30	7.39	2.41	35.0	560	23	481	45.3	13.9	9.9	204	61	0.3	293	8	10	32.6	0.3	488
198-1210B-																			
31H-4, 145-150	284.80	7.40	2.44	35.0	569			44.6	14.1	9.8			0.0	287	7	2	32.9	0.3	482

Table T14. Discrete measurements of *P*-wave velocity, Site 1210. (Continued on next page.)

Core, section, interval (cm)	Depth (mbsf)	Velocity (m/s)	Core, section, interval (cm)	Depth (mbsf)	Velocity (m/s)	Core, section, interval (cm)	Depth (mbsf)	Velocity (m/s)
198-1210A-			12H-1, 66	101.56	1543.9	23H-5, 67	212.07	1554.7
1H-1, 76	0.76	1515.7	12H-2, 65	103.05	1523.8	23H-6, 71	213.61	1552.5
1H-2, 74	2.24	1514.8	12H-3, 65	104.55	1532.3	24H-1, 72	215.62	1566.6
1H-3, 75	3.75	1534.0	12H-4, 65	106.05	1525.2	24H-2, 60	217.00	1569.0
1H-4, 68	5.18	1515.1	12H-5, 64	107.54	1530.8	24H-3, 71	218.61	1590.6
2H-1, 67	6.57	1516.2	12H-6, 68	109.08	1530.8	24H-5, 48	221.38	1560.9
2H-2, 67	8.07	1523.7	13H-1, 69	111.09	1548.5	24H-6, 53	222.63	1555.7
2H-3, 66	9.56	1527.6	13H-2, 75	112.64	1552.5	25H-1, 79	225.19	1576.6
2H-4, 67	11.07	1520.3	13H-3, 82	114.22	1538.5	25H-2, 71	226.61	1569.3
2H-5, 67	12.57	1511.7	13H-4, 60	115.50	1665.8	25H-3, 63	228.03	1561.4
2H-6, 65	14.05	1507.2	13H-5, 62	117.02	1543.9	25H-4, 49	229.39	1567.0
3H-1, 66	16.06	1494.3	13H-6, 65	118.55	1561.9	27H-1, 77	236.67	1557.9
3H-2, 66	17.56	1521.7	14H-1, 75	120.65	1552.0	27H-2, 76	238.16	1559.9
3H-3, 67	19.07	1520.0	14H-2, 74	122.14	1550.5	27H-3, 76	239.66	1560.4
3H-4, 64	20.54	1543.7	14H-3, 63	123.53	1562.7	27H-4, 76	241.16	1564.0
3H-5, 64	22.04	1504.2	14H-4, 73	125.13	1544.4			
3H-6, 64	23.54	1533.7	14H-5, 65	126.55	1568.5	198-1210B-		
3H-7, 56	24.96	1517.9	14H-6, 38	127.78	1554.3	1H-1, 72	0.72	1518.6
4H-1, 65	25.55	1522.7	15H-1, 64	130.04	1571.0	1H-2, 81	2.31	1517.7
4H-2, 65	27.05	1535.2	15H-2, 65	131.55	1551.5	1H-3, 106	4.06	1533.1
4H-3, 58	28.48	1524.1	15H-3, 65	133.05	1554.4	1H-4, 76	5.26	1512.6
4H-4, 66	30.06	1532.4	15H-4, 66	134.55	1551.9	1H-5, 81	6.81	1503.2
4H-5, 52	31.42	1527.4	15H-5, 65	136.05	1558.9	1H-6, 72	8.22	1501.9
4H-6, 64	33.04	1509.6	15H-6, 63	137.53	1555.4	2H-1, 70	9.90	1521.9
5H-1, 65	35.05	1522.4	16H-1, 62	139.52	1557.4	2H-2, 69	11.39	1511.0
5H-2, 66	36.56	1525.7	16H-2, 64	141.04	1546.1	2H-3, 71	12.91	1530.5
5H-3, 65	38.05	1524.2	16H-3, 63	142.53	1553.2	2H-4, 62	14.32	1517.6
5H-4, 60	39.50	1536.8	16H-4, 66	144.05	1572.1	2H-5, 68	15.88	1510.2
5H-5, 64	41.04	1526.0	16H-5, 63	145.53	1562.3	2H-6, 58	17.27	1533.2
5H-6, 66	42.56	1521.5	16H-6, 64	146.98	1549.0	3H-1, 68	19.38	1533.0
6H-1, 65	44.55	1522.0	17H-1, 67	149.07	1557.2	3H-2, 76	20.96	1514.7
6H-2, 64	46.04	1533.9	17H-2, 76	150.66	1559.2	3H-3, 64	22.34	1522.6
6H-3, 63	47.53	1540.6	17H-3, 76	152.16	1571.6	3H-4, 62	23.82	1509.0
6H-4, 63	49.03	1532.6	17H-4, 76	153.65	1565.0	3H-5, 64	25.34	1545.9
6H-5, 64	50.54	1532.8	17H-5, 76	155.16	1569.3	3H-6, 67	26.87	1538.5
6H-6, 64	52.04	1527.6	17H-6, 77	156.67	1572.9	4H-1, 74	28.94	1541.2
6H-7, 63	53.53	1536.3	18H-1, 63	158.53	1559.3	4H-2, 71	30.41	1538.5
7H-1, 62	54.02	1515.8	18H-2, 65	160.05	1574.2	4H-3, 87	32.07	1532.5
7H-2, 63	55.53	1526.6	18H-3, 64	161.54	1568.1	4H-4, 75	33.45	1529.4
7H-3, 56	56.96	1538.7	18H-4, 64	163.04	1568.2	4H-5, 81	35.01	1529.2
7H-4, 64	58.54	1517.1	18H-5, 64	164.54	1571.2	4H-6, 53	36.23	1542.6
7H-5, 66	60.06	1525.7	18H-6, 65	166.05	1573.5	5H-1, 69	38.39	1519.7
7H-6, 64	61.54	1524.9	19H-1, 66	168.05	1580.4	5H-2, 72	39.92	1516.0
8H-1, 66	63.56	1519.7	19H-2, 65	169.55	1566.8	5H-3, 74	41.44	1522.9
8H-2, 66	65.06	1512.6	19H-3, 65	171.05	1568.4	5H-4, 70	42.90	1524.3
8H-3, 66	66.56	1523.3	19H-4, 64	172.54	1579.5	5H-5, 72	44.42	1501.6
8H-4, 65	68.05	1524.1	19H-5, 66	174.05	1575.0	5H-6, 75	45.95	1525.3
8H-5, 65	69.55	1528.4	19H-6, 66	175.55	1574.5	6H-1, 65	47.85	1527.0
8H-6, 65	71.05	1528.2	20H-1, 70	177.60	1571.0	6H-2, 73	49.43	1532.9
8H-7, 63	72.53	1523.6	20H-2, 67	179.07	1554.1	6H-3, 73	50.93	1522.4
9H-1, 64	73.04	1510.2	20H-3, 70	180.60	1558.0	6H-4, 71	52.41	1518.0
9H-2, 65	74.55	1515.6	20H-4, 70	182.10	1555.1	6H-5, 76	53.96	1528.1
9H-3, 64	76.04	1535.9	20H-5, 67	183.57	1558.9	6H-6, 73	55.43	1523.7
9H-4, 63	77.53	1522.8	20H-6, 80	185.20	1553.4	6H-7, 37	56.57	1525.9
9H-5, 66	79.06	1516.9	21H-1, 64	187.04	1594.4	7H-1, 66	57.36	1528.7
9H-6, 64	80.54	1526.8	21H-2, 63	188.53	1565.7	7H-2, 66	58.86	1543.9
10H-1, 66	82.56	1526.7	21H-3, 64	190.04	1570.2	7H-3, 78	60.43	1533.4
10H-2, 66	84.06	1508.7	21H-4, 63	191.53	1567.0	7H-4, 78	61.93	1530.0
10H-3, 66	85.56	1530.4	21H-5, 66	193.06	1575.7	7H-5, 66	63.31	1529.9
10H-4, 66	87.06	1526.1	21H-6, 64	194.54	1570.5	7H-6, 64	64.79	1527.7
10H-5, 66	88.56	1516.7	22H-1, 68	196.58	1580.9	7H-7, 32	65.97	1530.6
10H-6, 64	90.04	1525.5	22H-2, 60	198.00	1549.4	8H-1, 68	66.88	1533.9
11H-1, 76	92.16	1528.0	22H-3, 67	199.57	1559.0	8H-2, 70	68.40	1515.1
11H-2, 75	93.65	1505.7	22H-4, 64	201.04	1565.1	8H-3, 72	69.92	1524.4
11H-3, 76	95.16	1516.4	23H-1, 71	206.11	1565.1	8H-4, 81	71.51	1525.2
11H-4, 67	96.57	1520.6	23H-2, 65	207.55	1560.6	8H-5, 77	72.96	1519.2
11H-5, 75	98.14	1524.1	23H-3, 61	209.01	1559.9	8H-6, 64	74.34	1520.6
11H-6, 76	99.66	1532.9	23H-4, 62	210.52	1554.7	8H-7, 45	75.65	1509.2

Table T14 (continued).

Core, section, interval (cm)	Depth (mbsf)	Velocity (m/s)	Core, section, interval (cm)	Depth (mbsf)	Velocity (m/s)	Core, section, interval (cm)	Depth (mbsf)	Velocity (m/s)
9H-1, 70	76.40	1522.2	18H-4, 70	166.40	1567.5	27H-5, 64	253.34	1559.8
9H-2, 69	77.89	1522.9	18H-5, 79	167.99	1576.0	28H-1, 63	256.83	1552.6
9H-3, 68	79.38	1525.5	18H-6, 72	169.41	1569.6	28H-2, 63	258.33	1546.5
9H-4, 60	80.80	1527.6	19H-1, 72	171.42	1556.8	28H-3, 63	259.83	1551.9
9H-5, 69	82.39	1514.6	19H-2, 82	173.02	1555.7	28H-4, 63	261.33	1552.2
9H-6, 67	83.87	1520.9	19H-3, 68	174.38	1564.2	28H-5, 65	262.85	1553.2
10H-1, 77	85.97	1536.3	19H-4, 74	175.94	1565.3	28H-6, 75	264.45	1561.7
10H-2, 70	87.39	1541.5	19H-5, 67	177.37	1563.4	29H-1, 64	266.34	1560.2
10H-3, 81	89.01	1527.3	19H-6, 67	178.87	1573.2	30H-1, 61	270.51	1591.6
10H-4, 69	90.39	1538.8	20H-1, 77	180.97	1567.9	30H-2, 63	272.03	1549.1
10H-5, 69	91.89	1542.1	20H-2, 75	182.45	1571.9	30H-3, 65	273.55	1563.7
10H-6, 67	93.37	1532.8	20H-4, 78	185.48	1556.2	30H-4, 64	275.04	1551.2
11H-1, 80	95.50	1523.2	20H-5, 70	186.90	1562.3	30H-5, 64	276.54	1575.7
11H-2, 70	96.90	1530.5	20H-6, 72	188.42	1573.8	30H-6, 64	278.04	1562.6
11H-3, 70	98.40	1533.5	20H-7, 37	189.57	1574.6	31H-2, 84	281.01	1569.8
11H-4, 72	99.92	1528.7	21H-1, 73	190.43	1568.0	31H-3, 65	282.32	1575.2
11H-5, 66	101.36	1541.2	21H-2, 73	191.93	1573.4	31H-4, 65	283.82	1561.3
11H-6, 68	102.88	1536.9	21H-3, 74	193.44	1576.7	31H-5, 65	285.32	1555.8
12H-1, 74	104.94	1531.8	21H-4, 73	194.93	1578.1	31H-6, 66	286.83	1570.9
12H-2, 74	106.44	1522.4	21H-5, 71	196.41	1585.2	32H-1, 63	289.03	1567.5
12H-3, 77	107.97	1531.5	21H-6, 72	197.92	1560.4	32H-2, 64	290.54	1574.8
12H-4, 72	109.42	1534.4	22H-1, 72	199.92	1568.5	32H-3, 66	292.06	1560.6
12H-5, 80	111.00	1537.4	22H-2, 75	201.45	1583.5	32H-7, 65	298.05	1582.0
12H-6, 80	112.50	1549.5	22H-3, 74	202.94	1576.2	33H-1, 66	293.56	1571.9
13H-1, 51	114.21	1580.6	22H-4, 75	204.45	1584.4	33H-2, 74	295.14	1559.8
13H-2, 70	115.89	1577.6	22H-5, 73	205.93	1573.9	33H-3, 75	296.65	1569.2
13H-3, 67	117.37	1557.0	22H-6, 75	207.45	1576.0	33H-4, 65	298.05	1584.2
13H-4, 66	118.86	1568.5	23H-1, 75	209.45	1566.3	34H-1, 105	302.35	1549.9
13H-5, 70	120.40	1559.3	23H-2, 67	210.87	1559.2	34H-2, 64	303.44	1561.2
13H-6, 69	121.89	1559.3	23H-3, 70	212.40	1560.0	34H-3, 66	304.96	1575.5
14H-1, 71	123.90	1548.2	23H-4, 71	213.91	1567.8	34H-4, 66	306.45	1572.3
14H-2, 73	125.43	1561.1	23H-5, 65	215.35	1563.6	35H-3, 66	313.26	1571.6
14H-3, 69	126.89	1559.4	23H-6, 61	216.81	1594.3	35H-4, 66	314.76	1569.5
14H-4, 72	128.42	1561.3	24H-1, 70	218.90	1556.8	35H-5, 75	316.35	1604.6
14H-5, 81	130.01	1552.1	24H-2, 63	220.33	1563.4	36H-4, 67	323.77	1575.2
14H-6, 94	131.63	1562.3	24H-3, 67	221.87	1572.4	36H-6, 75	326.85	1558.4
15H-1, 66	133.36	1555.8	24H-4, 73	223.43	1564.8	37H-1, 66	326.86	1583.5
15H-2, 80	135.00	1554.3	24H-5, 73	224.93	1570.5	37H-2, 64	328.34	1571.6
15H-3, 69	136.39	1552.5	24H-6, 70	226.40	1569.0	37H-3, 64	329.84	1584.8
15H-4, 75	137.95	1556.2	25H-1, 66	228.36	1581.3	38H-1, 75	331.95	1584.9
15H-5, 70	139.40	1561.1	25H-2, 66	229.86	1570.2	38H-2, 63	333.33	1571.2
15H-6, 77	140.97	1551.6	25H-3, 67	231.37	1574.8	38H-3, 65	334.85	1570.3
16H-1, 71	142.91	1546.7	25H-4, 66	232.86	1581.1	38H-4, 64	336.34	1572.1
16H-2, 67	144.37	1556.7	25H-5, 67	234.37	1570.2	38H-5, 64	337.84	1565.3
16H-3, 76	145.96	1552.2	25H-6, 65	235.85	1576.5	38H-6, 66	339.36	1577.3
16H-4, 76	147.46	1579.5	26H-1, 65	237.85	1560.6	41H-1, 65	358.65	1564.5
16H-6, 73	150.43	1586.4	26H-2, 65	239.35	1546.2	41H-2, 66	360.16	1570.9
17H-1, 76	152.46	1565.8	26H-3, 65	240.85	1547.0	41H-3, 77	361.77	1572.7
17H-2, 70	153.90	1565.6	26H-4, 65	242.35	1551.6	42H-1, 64	368.14	1558.1
17H-3, 79	155.49	1579.6	26H-5, 64	243.84	1554.2	42H-2, 67	369.67	1577.8
17H-4, 79	156.99	1562.9	26H-6, 65	245.35	1548.8	42H-3, 63	371.13	1556.3
17H-5, 84	158.54	1558.1	26H-7, 42	246.62	1561.1	42H-4, 66	372.65	1570.9
17H-6, 72	159.92	1566.1	27H-1, 66	247.36	1559.5	42H-5, 65	374.15	1569.0
18H-1, 76	161.96	1556.9	27H-2, 63	248.83	1569.6	42H-6, 64	375.64	1575.2
18H-2, 94	163.64	1570.6	27H-3, 64	250.34	1560.9			
18H-3, 73	164.93	1582.2	27H-4, 64	251.84	1553.6			

Table T15. Discrete index properties measurements for Site 1210. (Continued on next three pages.)

Core, section, interval (cm)	Depth (mbsf)	Water content (wt%)		Density (g/cm ³)			Porosity (%)	Void ratio
		Bulk mass	Dry mass	Bulk	Dry	Grain		
198-1210A-								
1H-1, 70-72	0.70	54.5	119.7	1.45	0.66	2.86	76.9	3.34
1H-2, 70-72	2.20	55.5	124.6	1.43	0.64	2.85	77.6	3.47
1H-3, 70-72	3.70	51.1	104.4	1.47	0.72	2.71	73.4	2.76
1H-4, 70-72	5.20	50.4	101.5	1.48	0.74	2.71	72.9	2.68
2H-1, 70-72	6.60	50.9	103.7	1.47	0.72	2.68	73.1	2.72
2H-2, 70-72	8.10	44.5	80.2	1.58	0.88	2.82	68.8	2.21
2H-3, 70-72	9.60	43.6	77.3	1.59	0.90	2.78	67.7	2.10
2H-4, 70-72	11.10	46.0	85.3	1.54	0.83	2.72	69.4	2.27
2H-5, 70-72	12.60	46.1	85.6	1.53	0.83	2.67	69.1	2.24
2H-6, 70-72	14.10	45.8	84.5	1.56	0.85	2.81	69.9	2.32
3H-1, 70-72	16.10	44.3	79.7	1.57	0.88	2.75	68.2	2.14
3H-2, 70-72	17.60	45.3	82.8	1.54	0.85	2.67	68.3	2.16
3H-3, 70-72	19.10	47.0	88.8	1.52	0.81	2.68	69.9	2.33
3H-4, 70-72	20.60	42.3	73.2	1.58	0.92	2.64	65.4	1.89
3H-5, 70-72	22.10	47.0	88.8	1.53	0.81	2.74	70.4	2.38
3H-6, 70-72	23.60	41.6	71.4	1.60	0.93	2.66	64.9	1.85
3H-7, 61-63	25.01	43.7	77.6	1.57	0.88	2.68	67.0	2.03
4H-1, 70-72	25.60	43.5	77.0	1.58	0.89	2.70	67.0	2.03
4H-2, 70-72	27.10	45.5	83.6	1.55	0.84	2.69	68.7	2.20
4H-3, 64-66	28.54	46.2	86.0	1.54	0.83	2.69	69.3	2.26
4H-4, 70-72	30.10	39.8	66.1	1.65	1.00	2.79	64.3	1.80
4H-5, 59-61	31.49	41.8	71.9	1.61	0.93	2.72	65.6	1.91
4H-6, 70-72	33.10	43.1	75.7	1.57	0.89	2.64	66.1	1.95
5H-1, 69-71	35.09	42.7	74.7	1.60	0.92	2.75	66.7	2.01
5H-2, 70-72	36.60	44.0	78.7	1.59	0.89	2.81	68.4	2.16
5H-3, 70-72	38.10	40.6	68.3	1.63	0.97	2.72	64.5	1.82
5H-4, 65-67	39.55	41.4	70.5	1.62	0.95	2.73	65.2	1.88
5H-5, 70-72	41.10	42.2	73.0	1.60	0.92	2.71	65.8	1.93
5H-6, 70-72	42.60	41.8	72.0	1.61	0.94	2.74	65.8	1.93
6H-1, 70-72	44.60	48.4	93.9	1.51	0.78	2.72	71.4	2.49
6H-2, 70-72	46.10	39.5	65.2	1.64	1.00	2.71	63.3	1.72
6H-3, 70-72	47.60	40.5	68.0	1.62	0.97	2.70	64.2	1.80
6H-4, 70-72	49.10	39.4	65.0	1.65	1.00	2.73	63.4	1.73
6H-5, 70-72	50.60	41.9	72.2	1.61	0.93	2.73	65.8	1.92
6H-6, 70-72	52.10	42.8	75.0	1.59	0.91	2.72	66.5	1.99
6H-7, 70-72	53.60	41.7	71.4	1.60	0.94	2.68	65.2	1.87
7H-1, 70-72	54.10	40.5	68.1	1.62	0.97	2.70	64.2	1.80
7H-2, 70-72	55.60	40.4	67.8	1.63	0.97	2.72	64.3	1.80
7H-3, 70-72	57.10	39.8	66.1	1.64	0.98	2.70	63.5	1.74
7H-4, 70-72	58.60	39.6	65.5	1.64	0.99	2.71	63.4	1.73
7H-5, 70-72	60.10	39.2	64.6	1.65	1.00	2.72	63.2	1.72
7H-6, 70-72	61.60	41.5	70.9	1.61	0.94	2.72	65.3	1.88
8H-1, 70-72	63.60	40.3	67.4	1.63	0.97	2.69	63.9	1.77
8H-2, 70-72	65.10	44.4	79.8	1.56	0.87	2.70	67.8	2.10
8H-3, 70-72	66.60	41.8	72.0	1.60	0.93	2.69	65.4	1.89
8H-4, 70-72	68.10	41.3	70.3	1.62	0.95	2.73	65.2	1.88
8H-5, 70-72	69.60	41.1	69.6	1.63	0.96	2.77	65.3	1.88
8H-6, 70-72	71.10	39.1	64.1	1.65	1.01	2.72	63.0	1.70
8H-7, 70-72	72.60	41.1	69.9	1.62	0.95	2.72	65.0	1.86
9H-1, 70-72	73.10	42.6	74.2	1.60	0.92	2.73	66.4	1.98
9H-2, 70-72	74.60	42.2	72.9	1.60	0.93	2.73	66.1	1.95
9H-3, 70-72	76.10	41.6	71.4	1.61	0.94	2.74	65.6	1.91
9H-4, 70-72	77.60	40.2	67.2	1.64	0.98	2.74	64.2	1.80
9H-5, 70-72	79.10	42.0	72.5	1.61	0.93	2.74	66.0	1.94
9H-6, 70-72	80.60	39.7	65.9	1.64	0.99	2.73	63.7	1.76
10H-1, 70-72	82.60	39.4	65.1	1.65	1.00	2.74	63.5	1.74
10H-2, 70-72	84.10	44.6	80.6	1.57	0.87	2.77	68.5	2.18
10H-3, 70-72	85.60	45.6	83.9	1.56	0.85	2.77	69.4	2.27
10H-4, 70-72	87.10	40.1	66.8	1.64	0.98	2.75	64.2	1.80
10H-5, 70-72	88.60	40.1	67.0	1.65	0.99	2.77	64.4	1.81
10H-6, 70-72	90.10	41.5	70.9	1.63	0.95	2.80	66.0	1.94
11H-1, 70-72	92.10	37.9	61.0	1.67	1.04	2.72	61.8	1.62
11H-2, 70-72	93.60	47.1	88.9	1.53	0.81	2.72	70.3	2.36
11H-3, 71-73	95.11	41.0	69.6	1.63	0.96	2.78	65.4	1.89
11H-4, 70-72	96.60	40.6	68.5	1.64	0.98	2.81	65.2	1.88
11H-5, 70-72	98.10	37.4	59.8	1.68	1.05	2.72	61.4	1.59

Table T15 (continued).

Core, section, interval (cm)	Depth (mbsf)	Water content (wt%)		Density (g/cm ³)			Porosity (%)	Void ratio
		Bulk mass	Dry mass	Bulk	Dry	Grain		
11H-6, 70-72	99.60	37.5	60.1	1.69	1.06	2.79	62.1	1.64
12H-1, 70-72	101.60	35.8	55.9	1.71	1.10	2.75	60.0	1.50
12H-2, 70-72	103.10	38.4	62.2	1.68	1.03	2.79	62.9	1.69
12H-3, 70-72	104.60	38.8	63.4	1.64	1.01	2.66	62.2	1.65
12H-4, 70-72	106.10	37.8	60.7	1.67	1.04	2.73	61.8	1.62
12H-5, 70-72	107.60	37.7	60.5	1.68	1.05	2.75	61.9	1.62
12H-6, 70-72	109.10	36.8	58.3	1.70	1.07	2.75	61.0	1.57
13H-1, 70-72	111.10	36.6	57.7	1.68	1.07	2.68	60.1	1.51
13H-2, 70-72	112.60	36.9	58.4	1.69	1.06	2.71	60.7	1.54
13H-3, 70-72	114.10	35.9	55.9	1.72	1.10	2.77	60.2	1.51
13H-4, 40-42	115.30	31.3	45.6	1.78	1.22	2.69	54.5	1.20
13H-4, 130-132	116.20	31.0	45.0	1.79	1.23	2.69	54.1	1.18
13H-5, 70-72	117.10	33.9	51.3	1.73	1.15	2.69	57.4	1.35
13H-6, 70-72	118.60	32.0	47.1	1.77	1.20	2.70	55.4	1.24
14H-1, 70-72	120.60	35.1	54.1	1.73	1.12	2.74	59.2	1.45
14H-2, 70-72	122.10	34.4	52.4	1.74	1.14	2.73	58.2	1.40
14H-6, 60-62	128.00	33.4	50.1	1.74	1.16	2.68	56.7	1.31
14H-7, 70-72	128.80	32.8	48.8	1.75	1.18	2.68	56.1	1.28
15H-1, 70-72	130.10	32.5	48.1	1.79	1.21	2.78	56.6	1.31
15H-2, 70-72	131.60	35.1	54.2	1.72	1.12	2.72	59.0	1.44
15H-3, 70-72	133.10	33.3	49.9	1.76	1.17	2.73	57.1	1.33
15H-4, 70-72	134.60	32.8	48.8	1.76	1.18	2.70	56.2	1.29
15H-5, 70-72	136.10	33.1	49.5	1.76	1.18	2.73	56.9	1.32
15H-6, 70-72	137.60	34.0	51.4	1.75	1.16	2.77	58.1	1.39
16H-1, 70-72	139.60	35.4	54.7	1.71	1.11	2.72	59.2	1.45
16H-2, 70-72	141.10	35.6	55.3	1.71	1.10	2.73	59.6	1.48
16H-3, 70-72	142.60	33.9	51.3	1.76	1.16	2.78	58.2	1.39
16H-4, 70-72	144.10	33.6	50.5	1.75	1.16	2.71	57.2	1.34
16H-5, 70-72	145.60	34.5	52.8	1.73	1.14	2.73	58.4	1.41
16H-6, 70-72	147.04	34.7	53.1	1.73	1.13	2.74	58.7	1.42
17H-1, 70-72	149.10	33.3	49.9	1.76	1.18	2.75	57.2	1.34
17H-2, 70-72	150.60	32.5	48.1	1.78	1.20	2.75	56.3	1.29
17H-3, 70-72	152.10	32.9	49.1	1.77	1.18	2.74	56.7	1.31
17H-4, 70-72	153.60	33.2	49.8	1.75	1.17	2.70	56.8	1.32
17H-5, 70-72	155.10	31.4	45.9	1.79	1.23	2.71	54.9	1.22
17H-6, 70-72	156.60	32.5	48.1	1.77	1.20	2.72	56.1	1.28
18H-1, 70-72	158.60	31.5	46.0	1.79	1.23	2.72	55.0	1.22
18H-2, 70-72	160.10	31.0	45.0	1.80	1.24	2.72	54.4	1.19
18H-3, 70-72	161.60	30.6	44.0	1.81	1.26	2.73	54.0	1.17
18H-4, 70-72	163.10	32.8	48.8	1.76	1.19	2.73	56.5	1.30
18H-5, 70-72	164.60	31.0	45.0	1.80	1.24	2.73	54.6	1.20
18H-6, 70-72	166.10	31.7	46.4	1.79	1.22	2.74	55.4	1.24
19H-1, 70-72	168.10	31.8	46.7	1.79	1.22	2.74	55.5	1.25
19H-2, 70-72	169.60	31.5	46.0	1.79	1.23	2.74	55.2	1.23
19H-3, 70-72	171.10	31.1	45.1	1.80	1.24	2.75	54.8	1.21
19H-4, 70-72	172.60	31.0	44.9	1.80	1.24	2.74	54.5	1.20
19H-5, 70-72	174.10	30.7	44.3	1.81	1.25	2.74	54.2	1.19
19H-6, 70-72	175.60	32.1	47.2	1.80	1.22	2.80	56.4	1.29
21H-1, 70-72	187.10	30.3	43.5	1.83	1.28	2.78	54.1	1.18
21H-2, 70-72	188.60	31.9	46.8	1.80	1.23	2.79	56.0	1.28
21H-3, 70-72	190.10	31.8	46.6	1.79	1.22	2.73	55.4	1.24
21H-4, 70-72	191.60	32.5	48.2	1.78	1.20	2.77	56.6	1.30
21H-5, 70-72	193.10	32.9	49.0	1.77	1.19	2.76	56.9	1.32
21H-6, 70-72	194.60	31.8	46.6	1.79	1.22	2.74	55.4	1.24
22H-1, 70-72	196.60	31.8	46.6	1.79	1.22	2.75	55.6	1.25
22H-2, 70-72	198.10	33.1	49.4	1.78	1.19	2.79	57.4	1.35
22H-3, 90-92	199.80	31.4	45.7	1.79	1.23	2.73	54.9	1.22
22H-4, 70-72	201.10	32.1	47.2	1.77	1.20	2.71	55.5	1.25
22H-5, 70-72	202.60	30.0	42.9	1.83	1.28	2.76	53.6	1.15
22H-6, 70-72	204.10	31.9	46.9	1.79	1.22	2.74	55.7	1.26
23H-1, 70-72	206.10	31.9	46.7	1.79	1.22	2.76	55.8	1.26
23H-2, 70-72	207.60	32.0	47.0	1.78	1.21	2.72	55.5	1.25
23H-3, 100-102	209.40	33.1	49.5	1.76	1.18	2.75	57.0	1.33
23H-4, 100-102	210.90	34.1	51.8	1.75	1.15	2.77	58.4	1.40
23H-5, 58-60	211.98	36.2	56.7	1.70	1.08	2.71	60.0	1.50
23H-6, 70-72	213.60	33.7	50.7	1.75	1.16	2.73	57.5	1.35
25H-1, 70-72	225.10	30.8	44.6	1.80	1.25	2.73	54.3	1.19
25H-2, 70-72	226.60	32.8	48.9	1.78	1.20	2.79	57.1	1.33
25H-3, 70-72	228.10	31.8	46.7	1.78	1.22	2.72	55.4	1.24

Table T15 (continued).

Core, section, interval (cm)	Depth (mbsf)	Water content (wt%)		Density (g/cm ³)			Porosity (%)	Void ratio
		Bulk mass	Dry mass	Bulk	Dry	Grain		
27H-1, 70-72	236.60	33.1	49.4	1.76	1.18	2.71	56.7	1.31
27H-2, 70-72	238.10	33.9	51.4	1.75	1.15	2.73	57.8	1.37
27H-3, 70-72	239.60	33.2	49.7	1.75	1.17	2.71	56.8	1.32
27H-4, 70-72	241.10	35.4	54.7	1.71	1.10	2.68	58.9	1.44
198-1210B-								
25H-1, 70-72	228.40	31.1	45.2	1.80	1.24	2.74	54.7	1.21
25H-2, 70-72	229.90	32.2	47.5	1.78	1.20	2.73	55.9	1.27
25H-3, 70-72	231.40	31.4	45.8	1.78	1.22	2.67	54.4	1.20
25H-4, 70-72	232.90	33.3	49.9	1.75	1.17	2.72	57.0	1.33
25H-5, 70-72	234.40	34.0	51.5	1.75	1.15	2.75	58.1	1.38
25H-6, 70-72	235.90	34.5	52.7	1.72	1.13	2.69	58.0	1.38
26H-1, 70-72	237.90	34.6	52.8	1.73	1.13	2.71	58.3	1.40
26H-2, 70-72	239.40	34.5	52.7	1.72	1.13	2.68	58.0	1.38
26H-3, 70-72	240.90	34.3	52.3	1.74	1.14	2.72	58.2	1.39
26H-4, 70-72	242.40	33.2	49.7	1.76	1.18	2.74	57.0	1.33
26H-5, 70-72	243.90	33.3	49.9	1.75	1.17	2.70	56.8	1.32
26H-6, 70-72	245.40	32.9	49.1	1.75	1.17	2.68	56.3	1.29
26H-7, 70-72	246.90	31.7	46.5	1.77	1.21	2.68	54.9	1.22
27H-1, 70-72	247.40	33.2	49.6	1.75	1.17	2.69	56.5	1.30
27H-2, 70-72	248.90	31.4	45.7	1.77	1.22	2.67	54.4	1.19
27H-3, 70-72	250.40	31.6	46.2	1.78	1.22	2.71	55.0	1.22
27H-4, 70-72	251.90	32.8	48.7	1.76	1.18	2.70	56.3	1.29
27H-5, 70-72	253.40	34.5	52.6	1.72	1.13	2.68	57.9	1.38
28H-1, 70-72	256.90	33.3	49.9	1.74	1.16	2.67	56.6	1.30
28H-2, 70-72	258.40	33.8	51.0	1.73	1.15	2.68	57.1	1.33
28H-3, 70-72	259.90	34.1	51.7	1.74	1.14	2.71	57.8	1.37
28H-4, 70-72	261.40	34.3	52.1	1.73	1.14	2.71	57.9	1.38
28H-5, 70-72	262.90	33.3	50.0	1.74	1.16	2.69	56.7	1.31
28H-6, 70-72	264.40	34.4	52.5	1.73	1.14	2.72	58.3	1.40
29H-1, 70-72	266.40	35.6	55.4	1.70	1.09	2.68	59.1	1.45
30H-1, 70-72	270.60	34.0	51.6	1.73	1.14	2.68	57.5	1.35
30H-2, 70-72	272.10	34.0	51.4	1.73	1.15	2.70	57.5	1.35
30H-3, 70-72	273.60	34.3	52.1	1.72	1.13	2.67	57.6	1.36
30H-4, 70-72	275.10	34.0	51.5	1.74	1.15	2.72	57.8	1.37
30H-5, 70-72	276.60	32.1	47.3	1.76	1.19	2.66	55.1	1.23
30H-6, 70-72	278.10	33.8	51.1	1.73	1.14	2.65	57.0	1.33
31H-2, 90-92	281.07	32.2	47.6	1.77	1.20	2.71	55.7	1.26
31H-3, 70-72	282.37	32.1	47.2	1.77	1.20	2.69	55.3	1.24
31H-4, 70-72	283.87	33.4	50.1	1.74	1.16	2.68	56.7	1.31
31H-5, 70-72	285.37	33.3	49.9	1.75	1.17	2.72	57.0	1.33
31H-6, 70-72	286.87	31.8	46.5	1.77	1.21	2.69	55.0	1.22
32H-1, 70-72	289.10	31.2	45.3	1.80	1.24	2.74	54.8	1.21
32H-2, 70-72	290.60	32.6	48.4	1.82	1.23	2.91	58.0	1.38
32H-3, 70-72	292.10	32.3	47.8	1.77	1.20	2.72	55.9	1.27
32H-7, 70-72	298.10	29.3	41.4	1.81	1.28	2.67	51.9	1.08
33H-1, 70-72	293.60	31.3	45.6	1.79	1.23	2.70	54.6	1.21
33H-2, 70-72	295.10	33.3	50.0	1.75	1.17	2.72	57.1	1.33
33H-3, 70-72	296.60	31.0	44.8	1.80	1.24	2.73	54.4	1.19
33H-4, 70-72	298.10	30.8	44.6	1.82	1.26	2.77	54.7	1.21
34H-1, 100-102	302.30	33.4	50.2	1.75	1.16	2.70	57.0	1.32
34H-2, 70-72	303.50	31.7	46.4	1.77	1.21	2.67	54.7	1.21
34H-3, 70-72	305.00	32.8	48.9	1.76	1.18	2.70	56.3	1.29
34H-4, 70-72	306.50	32.6	48.3	1.76	1.19	2.71	56.1	1.28
35H-3, 70-72	313.30	32.0	47.1	1.79	1.22	2.75	55.9	1.27
35H-4, 70-72	314.80	31.9	46.9	1.78	1.21	2.72	55.5	1.25
35H-5, 70-72	316.30	30.7	44.3	1.81	1.25	2.74	54.3	1.19
36H-4, 70-72	323.80	30.8	44.5	1.79	1.24	2.70	53.9	1.17
36H-6, 70-72	326.80	31.5	45.9	1.79	1.23	2.74	55.1	1.23
37H-1, 70-72	326.90	31.5	46.1	1.80	1.23	2.77	55.5	1.25
37H-2, 70-72	328.40	33.1	49.4	1.76	1.18	2.71	56.7	1.31
37H-3, 70-72	329.90	31.6	46.3	1.78	1.21	2.69	54.8	1.21
38H-1, 70-72	331.90	30.4	43.8	1.80	1.25	2.70	53.5	1.15
38H-2, 70-72	333.40	31.4	45.8	1.78	1.22	2.68	54.5	1.20
38H-3, 70-72	334.90	30.9	44.7	1.80	1.24	2.72	54.2	1.18
38H-4, 70-72	336.40	32.6	48.3	1.77	1.20	2.74	56.3	1.29
38H-5, 70-72	337.90	32.5	48.2	1.76	1.19	2.70	56.0	1.27
38H-6, 70-72	339.40	31.8	46.7	1.78	1.21	2.70	55.2	1.23
41H-1, 70-72	358.70	32.7	48.7	1.76	1.18	2.71	56.3	1.29

Table T15 (continued).

Core, section, interval (cm)	Depth (mbsf)	Water content (wt%)		Density (g/cm ³)			Porosity (%)	Void ratio
		Bulk mass	Dry mass	Bulk	Dry	Grain		
41H-2, 70-72	360.20	31.7	46.4	1.77	1.21	2.69	54.9	1.22
41H-3, 70-72	361.70	31.4	45.8	1.80	1.24	2.76	55.2	1.23
42H-1, 70-72	368.20	32.8	48.7	1.75	1.17	2.66	55.9	1.27
42H-2, 70-72	369.70	31.4	45.8	1.78	1.22	2.67	54.4	1.20
42H-3, 70-72	371.20	32.6	48.5	1.76	1.18	2.69	56.0	1.27
42H-4, 70-72	372.70	31.8	46.5	1.78	1.21	2.71	55.2	1.23
42H-5, 70-72	374.20	32.5	48.1	1.77	1.19	2.72	56.1	1.28
42H-6, 70-72	375.70	32.4	47.8	1.77	1.19	2.70	55.8	1.26